Delft University of Technology
Faculty of Civil Engineering and Geosciences
Department of Design and Construction
Section of Structural and Building Engineering
Concrete Structures

Report 25.5-22-03
Project CS3B13
Date April 2022
Status Final
Version 1.00

Experiment report on steel-concrete-composite bridge deck without mechanical connectors (Verbundträger)

Anders Jørgensen
Mauro Poliotti
Yuguang Yang

Research assigned by

Ingenieursbureau
Gemeente Amsterdam

PO Box 5048
2600GA Delft
The Netherlands

RELEASE NOTES:

Version	Date	Detail
0.10	25-03-2022	First draft.
0.11	05-04-2022	Second draft.
0.12	12-04-2022	Third draft.
1.00	02-05-2022	First Version

SUMMARY

The purpose of the testing of LB1 and LB3 is to find the load bearing capacity and the failure mechanism of the two specimens. In this report the methods and results following the experiments are shown. The methods and results of the experiments are summarized as follows:

1. The bearing capacity and the structural responses of the specimens during the loading process was investigated using load cells, lasers, LVDTs, optic fibers and DIC.

2. Both specimens were tested using four-point bending test.

3. For LB1 the max load was achieved at 1746 kN. The maximum vertical displacement at mid-span was 43 mm.

4. LB1 reached its maximum bearing capacity when steel beams reached the yielding stress. Afterwards a brittle failure of the interface between one of the beams and the concrete was observed, limiting the ductility of the element.

5. For LB3 the max load was achieved at 1494 kN. The maximum vertical displacement at mid-span was 69 mm.

6. LB3 failed due to bending by yielding of the steel beams and later concrete crushing on the top of the specimen.

Files and folders that accompany this document are listed in the following.

- **Measurement plan drawing**
  Files: 20220127-MeasuringPlan-LB1-v6.pdf
  20220308-MeasuringPlan-LB3-v5.pdf
- **Test Measurement Data**
  Files:
  20220128-Data_LB1.xlsx
  20220309-Data-LB3.xlsx
  20220309-Data-LB3-reloadingTest.xlsx
- **Sensor Details**
  Files: 20220127-SensorDetails-LB1.xlsx
  20220309-SensorDetails-LB3.xlsx
- **2D DIC Data**
  Files: 20220131-2D-DIC-Report-LB1.pdf
  20220309-2D-DIC-Report-LB3.pdf
- **3D DIC Data**
  Files: 20220131-3D-DIC-Report-LB1.pdf
  20220309-3D-DIC-Report-LB3.pdf

CONTENTS

1. DESCRIPTION OF SPECIMENS

The main goal of this report is to describe the experiments of specimens LB1 and LB3 from Amsterdam Bridge 70. For LB1 the test took place on January 26th and for LB3 on March 4th and reloading on March 8th. Testing of the specimens took place in the Stevin Lab at TU Delft. The specimen LB2 is not included in this report as it was tested by TNO. Material tests were also performed by TNO to characterise the material parameters. (Brongers, 2021) (Rasker, 2020)

The specimens were part of a bridge with multiple simple supported spans in Amsterdam. The specimens were cut into pieces of around 2000 mm width. The purpose of testing is to find the load bearing capacity and the failure mechanisms of the elements. Both specimens are concrete-steel composite sections without mechanical connectors between steel and concrete. Therefore, special emphasis was made to track the interface behaviour.

Dimensions of LB1 are shown on Fig. 1.1 and Fig.1.2. LB1 has a length between supports of 5900 mm. Furthermore, the tested cross-section consists of three I-beams, the two outer beams (beams 1 and 3) have a height and flange width at 280 mm and flange thickness at 18 mm. The middle beam, beam 2, has a height and flange width at 260 mm and flange thickness at 17.5 mm. At the end of the specimen its cross section is squared, whereas for the cross section between supports there's a trapezoid shaped gap between the beams with height 130 mm and width 125 mm at the top and 330 mm at the bottom. The gap continues at the outside of the outer beams as shown on Fig.1.2. In the following the steel beams are referred to as beam 1, beam 2 and beam 3, as shown on Fig. 1.1 and Fig.1.3.

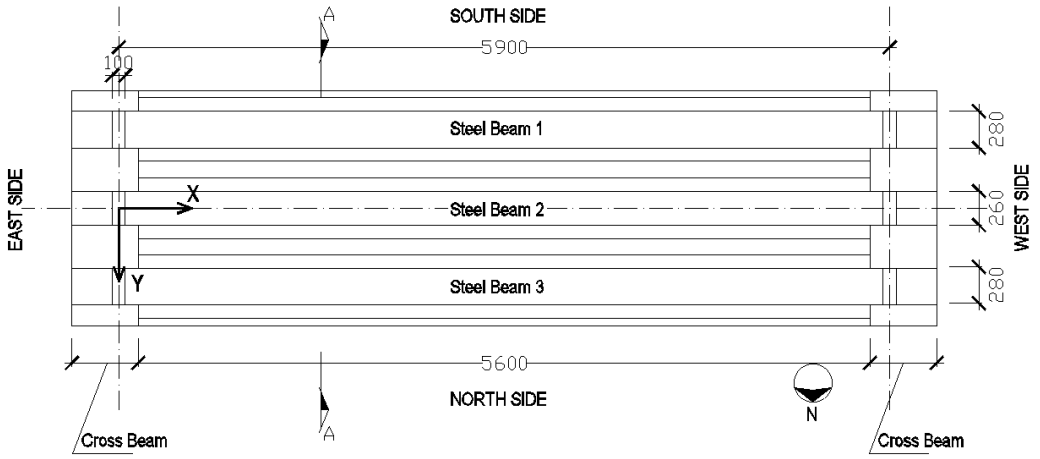

Fig. 1.1. LB1 - Bottom view. Dimensions of LB1 and position of beam 1, beam 2 and beam 3.

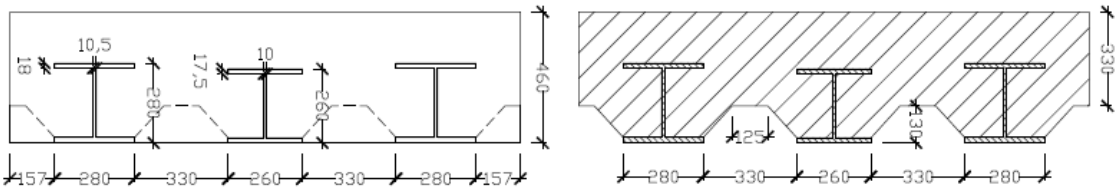

Fig.1.2. LB1 - East view and Section A-A.

The dimensions of LB3 are shown at Fig.1.3 and Fig.1.4. LB3 has a length of 7665 mm between supports. Like LB1, LB3 has three I-beams whereas the outer beams have different dimensions than the middle beam. The outer beams have a height of 340 mm and a flange width of 300 mm. Furthermore, the flange thickness is 21,5 mm and the web thickness is 12 mm. The middle beam has a height and flange of width of 300 mm. In addition, the flange thickness is 19 mm, and the

web thickness is 11 mm. Between the beams there is a trapezoidal shaped gap with height 190 mm and top and bottom width respectively 80 mm and 300 mm, The gap continues the outside of the outer beams, as shown on Fig.1.4.

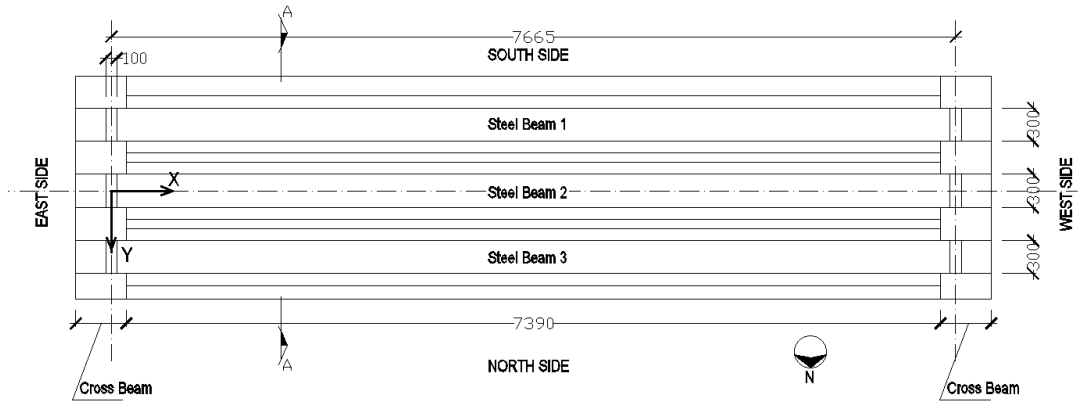

Fig.1.3. LB3 - Bottom view. Dimensions of LB3 and position of beam 1, beam 2 and beam 3.

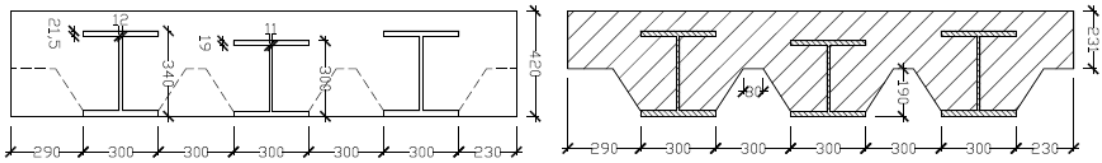

Fig.1.4. LB3 - East view and Section A-A.

In the lab, the specimens were simply supported to reproduce the real conditions of the structure. The supports at both sides were placed underneath the steel beams, as can be seen from Fig.1.5. Both supports were built assuring rotational freedom. A detail of the support for the specimens is shown at Fig.1.5, Fig.1.6 and Fig.1.7.

Fig.1.5. LB1. East side view.

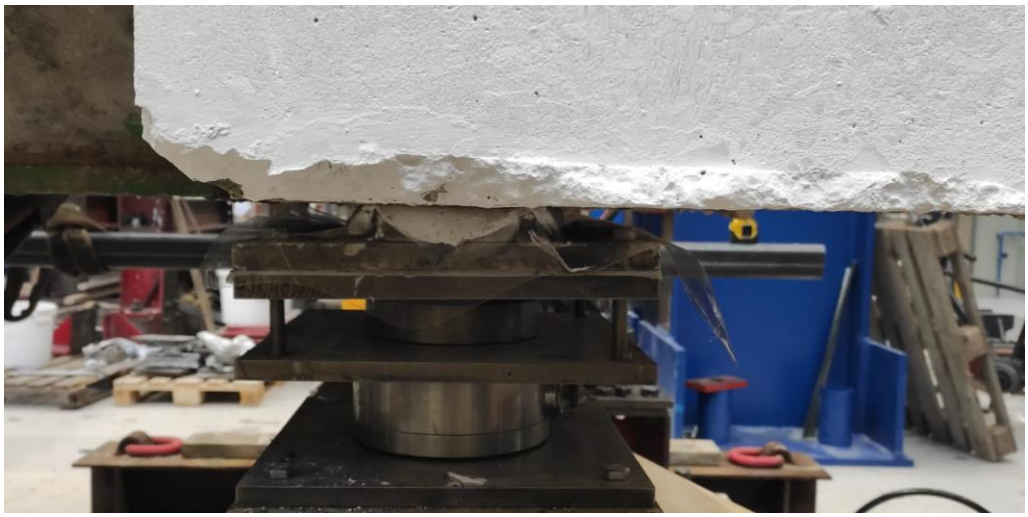

Fig.1.6. LB1. West side support below beam 3.

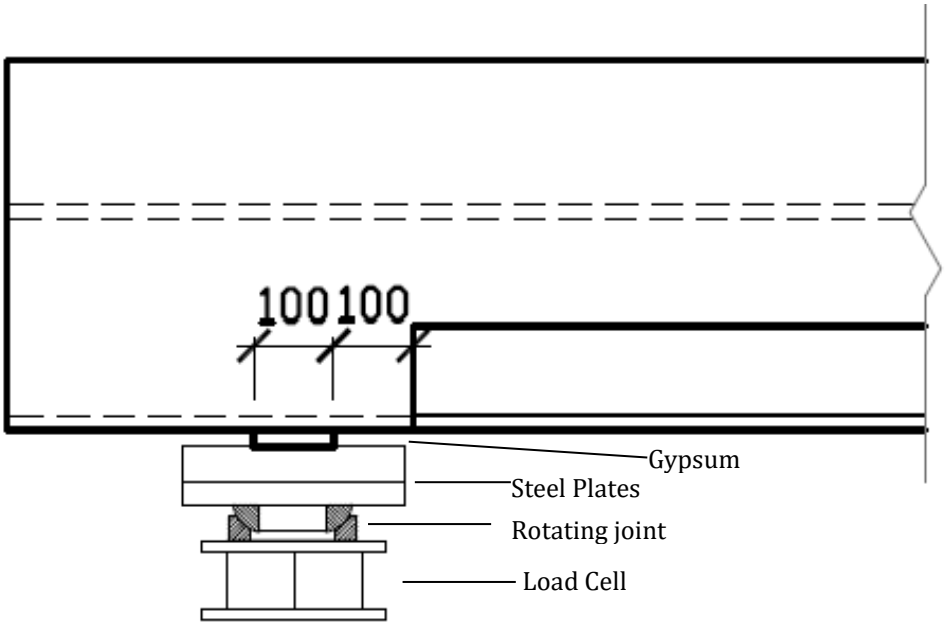

Fig.1.7. LB1. Detail of the supports.

2. METHODS

2.1. TEST SETUP

The test setup for LB1 and LB3 were designed to be as similar as possible. Only the distance between the sensors for LB1 and LB3 varied because the different length of the two specimens.

2.1.1. Loading

The specimens were tested following a four-point bending scheme. Two hydraulic jacks transferred the loads to spreader I-beams which each one was supported by two loading plates. The distance between the hydraulic jacks is 1200 mm in the longitudinal direction and were place symmetrically from the supports. The distance between the loading plates on the transverse direction was 600 mm center to center. Furthermore, the loading plates have a contact dimension of 230x230 mm. The position of the hydraulic jacks and loading plates, is shown for each specimen at Fig.2.1 to Fig.2.4.

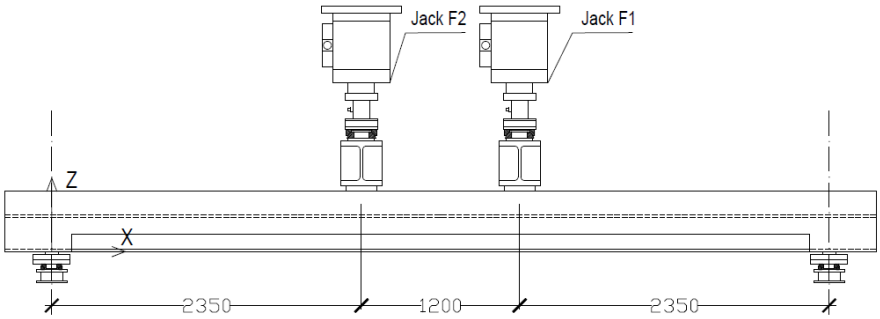

Fig.2.1. LB1 - North side view. Position of jack F1 and F2.

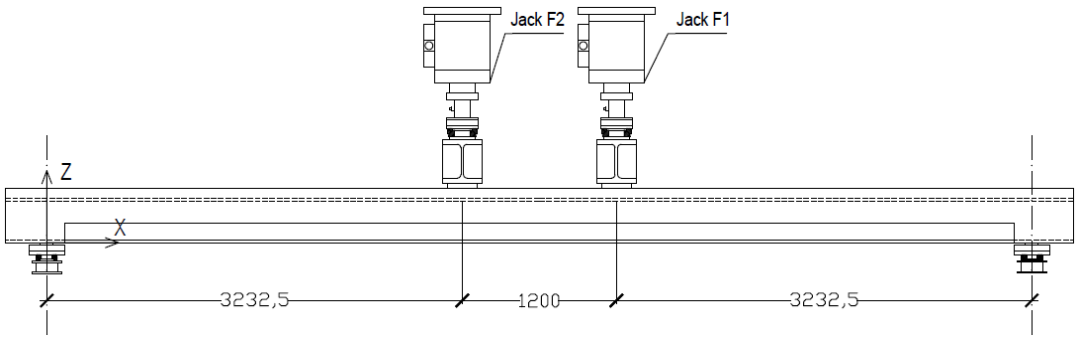

Fig.2.2. LB3 - North side view. Position of jack F1 and F2.

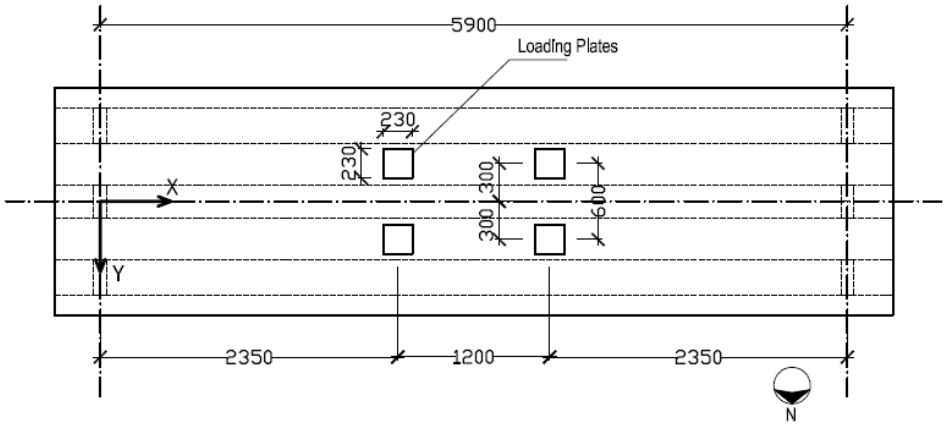

Fig.2.3. LB1 - Top view. Position loading plates.

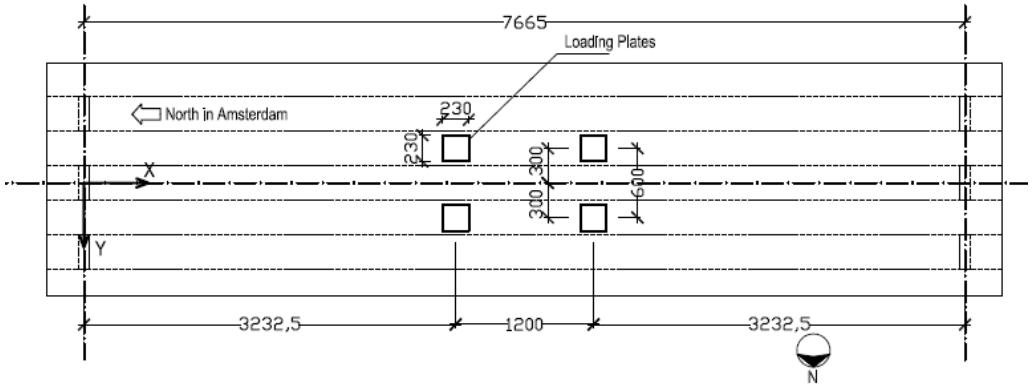

Fig.2.4. LB3 - Top view. Position loading plates.

In the following when referring to the hydraulic jacks the names F1 and F2 are used, as shown in Fig.2.1 and Fig.2.2. The specimens were loaded using displacement control at a rate of 0.01mm/sec. Displacement control was used on jack F2, whereas jack F1 was set to load control following the loading of jack F2. Each hydraulic jack has a range of 1600 kN and a sensitivity of 1 kN. The load history for testing of LB1 are shown in Table 1 and Fig.2.5.

Table 1. LB1 - Load history. Hold steps

Displacement rate 0.01 mm/sec	
1 jack load [KN]	Total load [KN]
25	50
75	150
125	250
175	350
225	450
325	650
425	850
525	1050
625	1250
700	1400
750	1500
790	1580
800	1600
850	1700
25	50
850	1700
872	1744

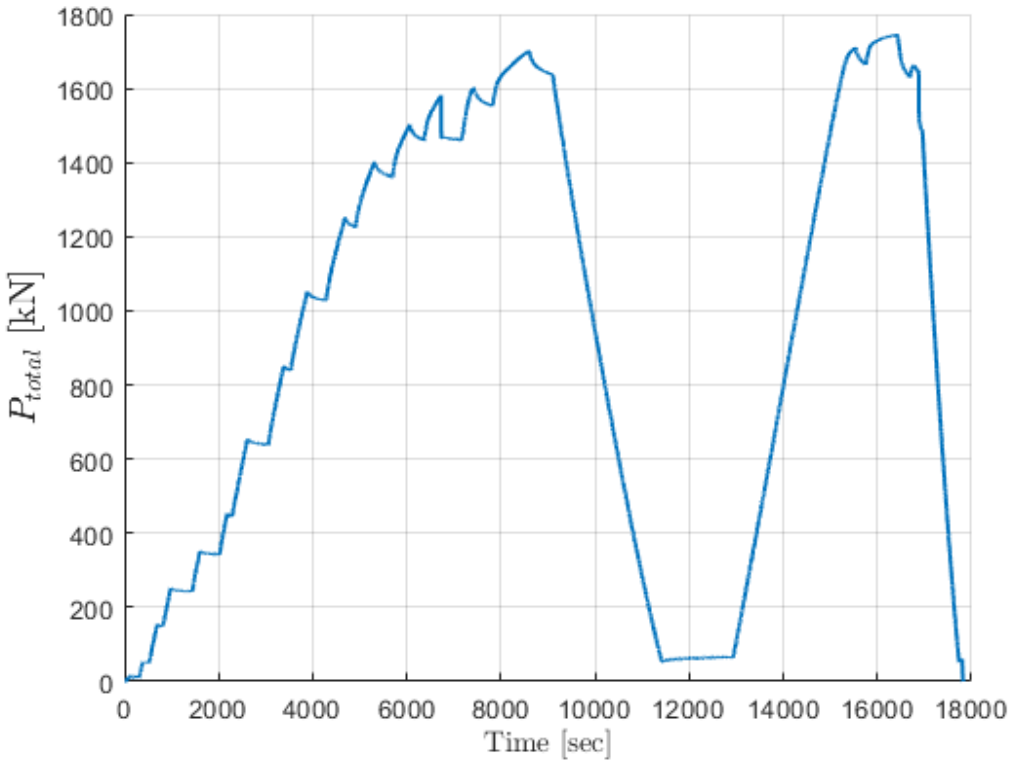

Fig.2.5. LB1. Load history

The load history for specimen LB3 is shown at Table 2 and Fig.2.6. The testing of LB3 was stopped because the maximum displacement range of one of the jacks was achieved. After unloading, plates were added to were added to increase the displacement range. During the reloading phase the displacement rate was 0.03 mm/sec.

Table 2. LB3 - Load history. Hold steps.

Displacement rate 0.01 mm/sec	
1 jack load [kN]	Total load [kN]
25	50
75	150
125	250
175	350
225	450
325	650
425	850
475	950
525	1050
575	1150
600	1200
625	1250
650	1300
675	1350
700	1400
725	1450

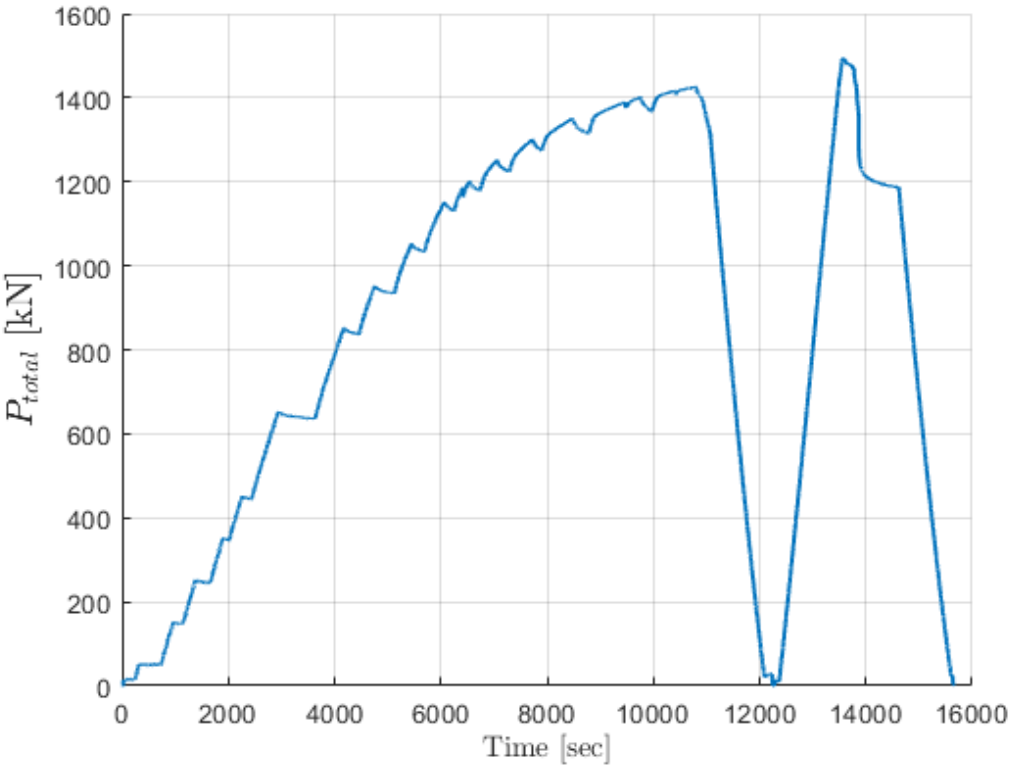

Fig.2.6. LB3. Load history. After 11000 seconds the test was stopped because the maximum displacement range was achieved. The specimen was unloaded to 0 kN and reloaded again.

2.2. SENSOR DESCRIPTION

2.2.1. Load cells

At both ends of the bridge deck three load cells were installed to monitor the reaction forces. Each load cell has a range of 1000 kN. The position of the load cells is shown on Fig.2.7 and a picture of LB1 with the load cells can be seen from Fig.2.8. In addition, one load cell was used for each hydraulic jack, to monitor the applied loads.

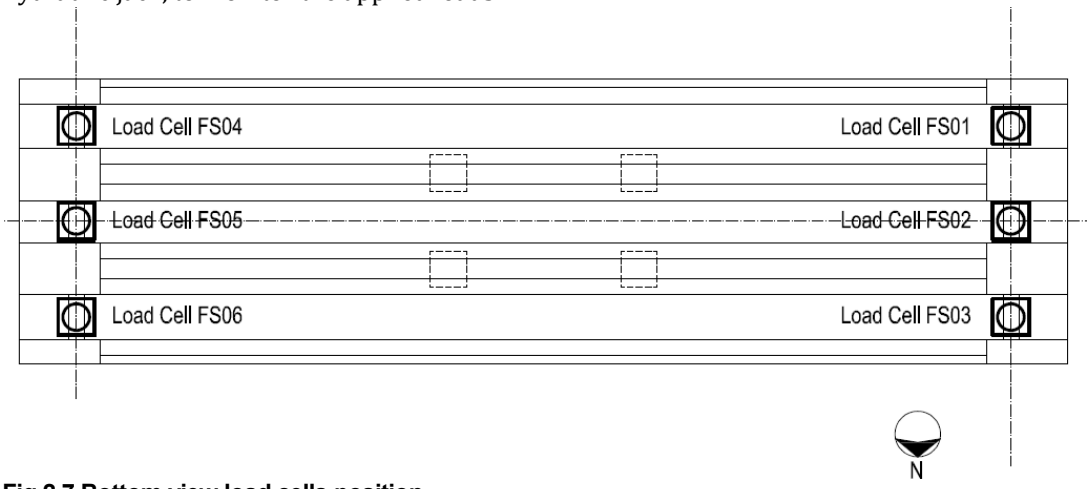

Fig.2.7 Bottom view load cells position.

Fig.2.8. LB1 – Load Cells East view of the specimen.

2.2.2. Lasers

Lasers were used to measure the total vertical displacement of the specimen at different positions. The lasers were attached to a steel frame placed beneath the specimen; the position of the lasers is shown at Fig.2.9 and Fig.2.10. The lasers were pointing upwards at the bottom of the steel beams in the specimen, as shown on figure 2.14. Every laser has a range of 50 mm and a sensitivity of 0.1 mm.

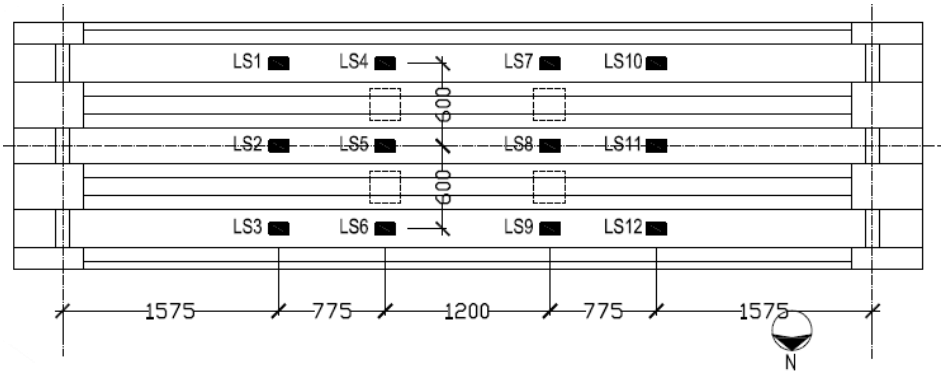

Fig.2.9. LB1 - Bottom view. Position of the lasers.

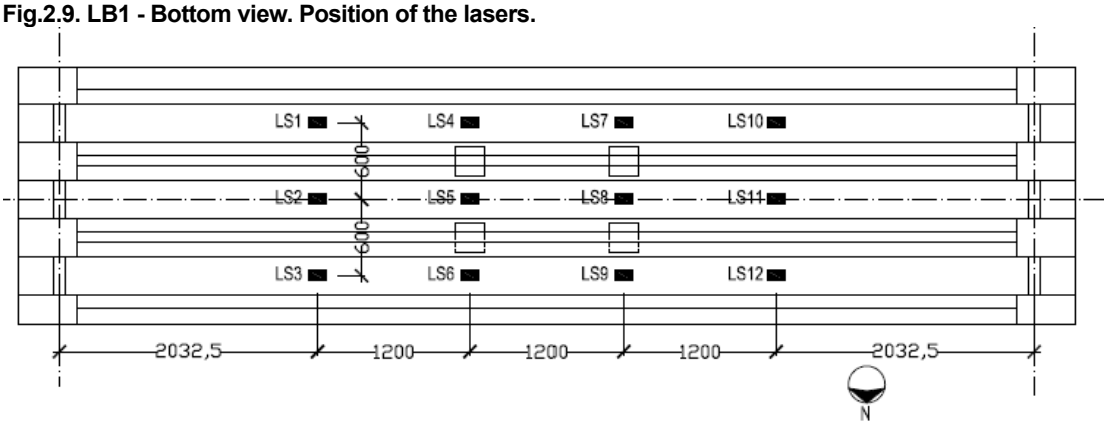

Fig.2.10. LB3 - Bottom view. Position of the lasers.

Fig.2.11. Laser measuring vertical displacement from bottom of a steel beam.

2.2.3. LVDTs

The purpose of the LVDTs 1-4 was to track the behavior of the interface between the bottom steel flange the adjacent concrete. This was done by measuring the longitudinal relative displacement between steel and concrete at different location along the specimen. LVDT 1-4 were placed at the central steel beam (beam 2). See Fig.2.12 and Fig.2.13.

LVDT 5-10 measured the relative transverse displacement between the bottom flange of the beams. The odd numbered LVDTs of LVDT 5-10, measured the transverse displacement between beam 1 and beam 2. The even numbered LVDT measured the transverse displacement between beam 2 and beam 3.

LVDTs 11 to 14 were also used to track the interface behavior by measuring the relative longitudinal displacement between steel and concrete at the end of the specimens. LVDTs 11 and 13 measured the relative longitudinal displacement between the bottom steel flange and the adjacent concrete for beams 2 and 1, respectively. LVDts 12 and 14 measure the relative longitudinal displacement between the top steel flange and the adjacent concrete for beams 2 and 1, respectively. LVDTs 11 to 14 were placed on the east end of specimen LB1, and on the west end for LB3. The LVDTs were positioned as shown at Fig.2.12-Fig.2.16.

LVDTs 1to 10 have a range of 10 mm and a sensitivity of 0.001 mm. LVDT 11-14 have a range of 2 mm and a sensitivity of 0.0005 mm. LVDT 15, was used for replacing a damaged optic fiber sensor, FO-S2-7 for LB1 and FO-C1-7 for LB3. LVDT 15 has a range of 2 mm, a sensitivity of 0.0005 mm and a base length of 200 mm.

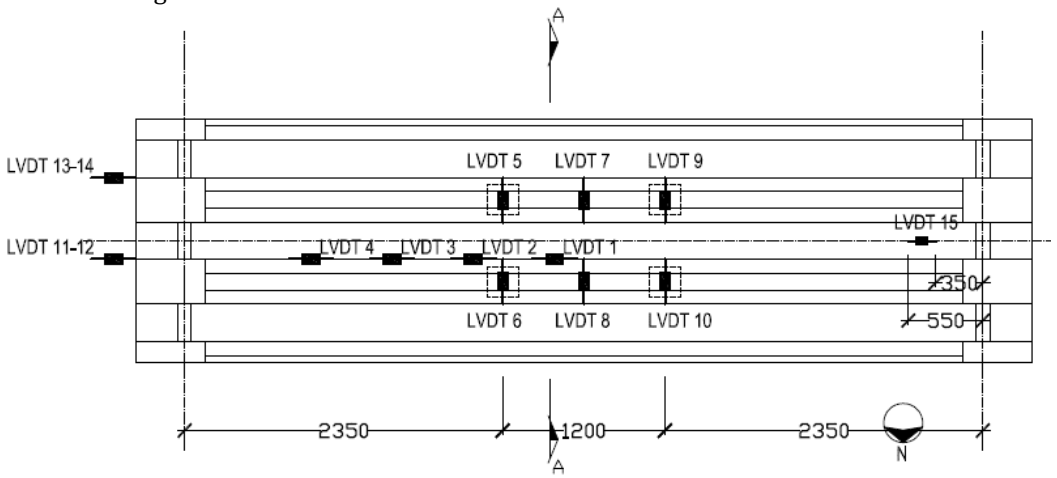

Fig.2.12. LB1 - Bottom view. Position of LVDT 1-15. LVDT 15 position at the west end of beam 2 to replace FO-S2-7.

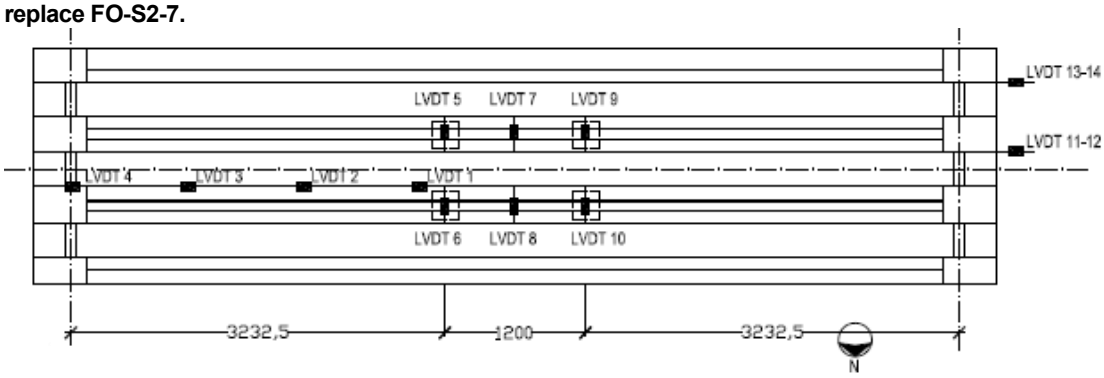

Fig.2.13. LB3 - Bottom view. Position of LVDT 1-14.

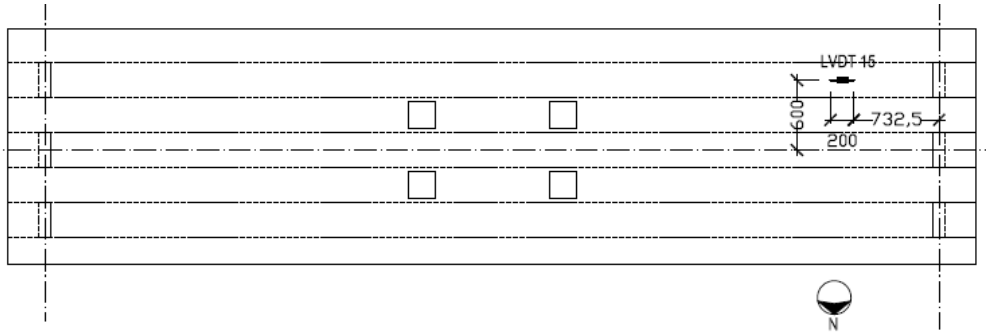

Fig. 2.14. LB3 - Top view. Position of LVDT 15.

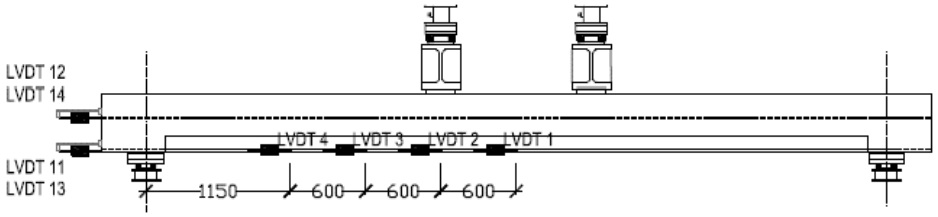

Fig.2.15. LB1 - North side view. Position of LVDT 1-4 and LVDT 11-14.

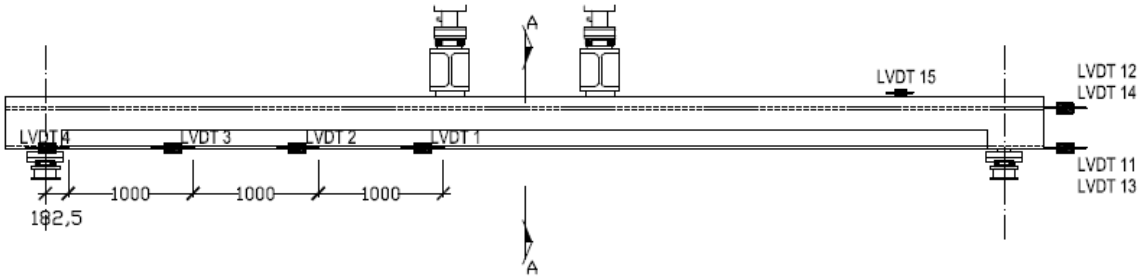

Fig.2.16. LB3 - North side view. Position of LVDT 1- 4 and LVDT 11-15.

The LVDTs measuring the relative transverse displacements between the central and outer steel beams were glued on the bottom flange of the steel beams. The setup of the LVDTs measuring relative transverse displacements is shown at Fig.2.17 and Fig.2.18.

Fig.2.17. LVDT 5-10 measuring relative transverse displacement between the beams.

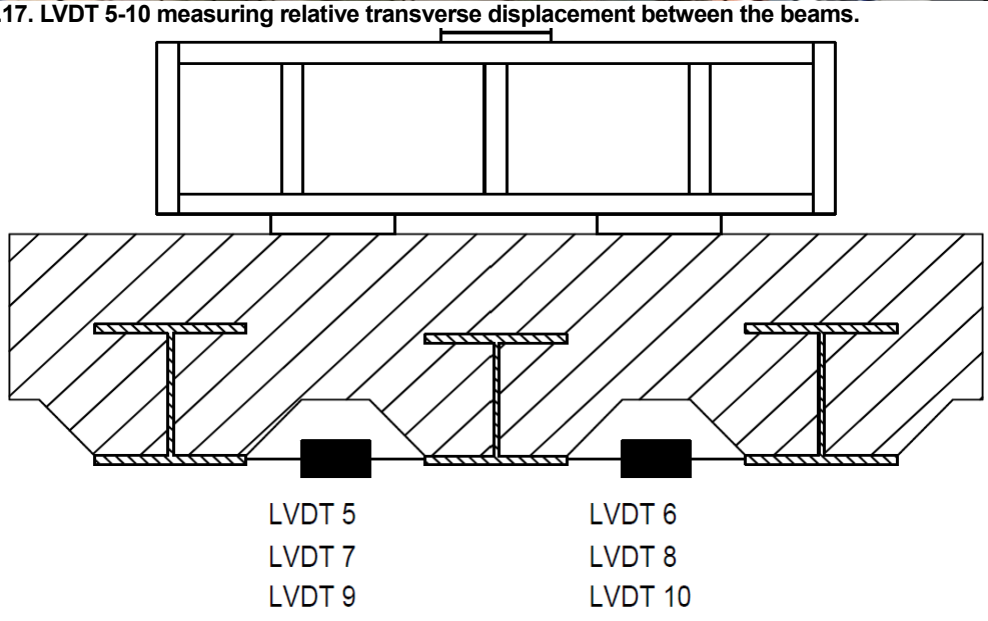

Fig.2.18. Section A-A. Position of LVDT 5-10.

LVDTs 1-4 used for measuring the relative longitudinal displacement between the bottom flange of the steel beam and the adjacent concrete, were installed as shown on Fig.2.19.

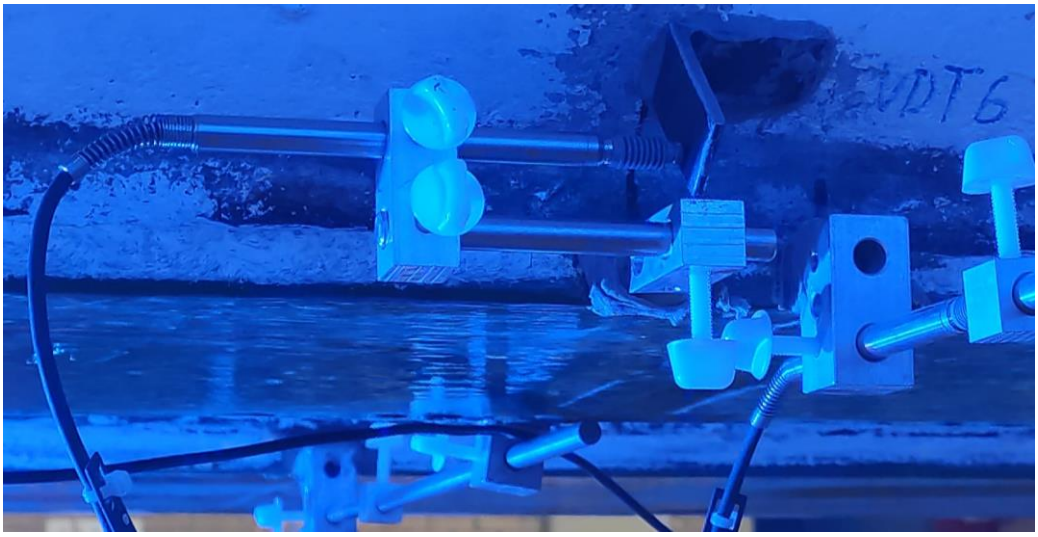

Fig.2.19. Installation of LVDTs 1-4 measuring relative longitudinal displacement.

The LVDTs 11 to 14 at the ends. were installed by fixing it to the concrete while the sensor measures the displacement ofthe steel beam. The position of the LVDTs is shown at Fig.2.20 Fig.2.22. In LB1, the concrete covering the central steel beam (beam 2) at the end was removed so it was possible to perform the measurement.

Fig.2.20. LVDTs 11-14 measuring relative longitudinal displacement at the end of LB1.

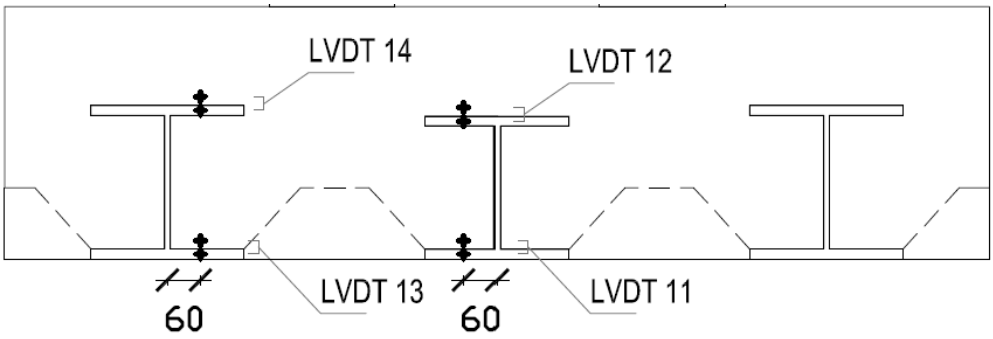

Fig.2.21. LB1 - East view. Position of LVDT 11-14.

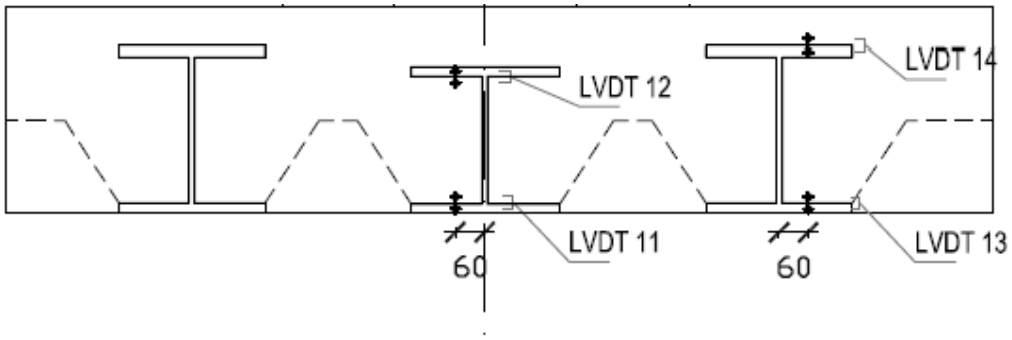

Fig.2.22. LB3 - West view. Position of LVDT 11-14.

2.2.4. Optic-fibers

Optic fibers were used to measure strains both in concrete and steel. The optic fibers used are quasi distributed strain sensors that measure deformations over a base length distance of 200mm which is used to convert deformations into strains, see **Error! Reference source not found.**. The o ptic fibers have a range of $\pm 2500 \mu\varepsilon$ and a sensitivity of $1.2 \mu\varepsilon$.

In particular, optic fibers with multiple Fiber Bragg Gratings (FBGs) are used. Each FBG reflects a specific wavelength of light, when the optic fiber is exposed to external influences, such as changes of strains or temperature, the reflected light shifts and a different wavelength is measured. The relationship between strain and wavelength shifts is linear, which makes them suitable for strain measurement, (Faassen, 2021)

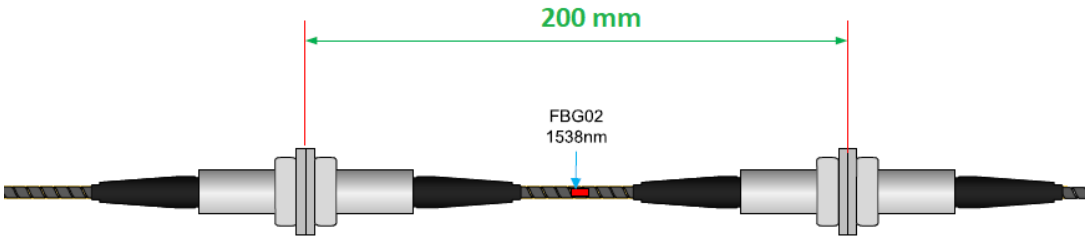

Fig.2.23. Detail of an optic fiber and an FBG sensor. (Faassen, 2021)

Optic-fiber sensors were installed at the top concrete layer and at the bottom flange of the steel beams to measure compressive and tensile strains respectively. They were installed in continuous cables of seven FBG sensors each. In total six cables were used making a total of 42 sensors, 21 for compressive strains in concrete and 21 for tensile strains on steel. Three cables were used on the steel beams and three on the correspondent concrete top. See Fig.2.24, Fig.2.25, Fig.2.28 and Fig.2.29

The optic fibers were attached to holders, that were screwed onto steel plates, that were glued to the specimens as shown at Fig.2.26 and Fig.2.27. To avoid failure of the glue during testing, the steel plates that were glued to the specimens had been sanded to make the surface rough.

The optic-fibers installed at the top concrete layer had been prestressed to ensure the optic fibers always will be in tension, as the concrete will compress when the specimen is loaded. The optic fibers installed at the bottom flanges of the steel beams had also been prestressed, but to a lower level as the fibers are expected to measure tension.

During installation of the optic fibers for LB1 sensor FO-S2-7 was damaged. In replacement LVDT 15 was installed with the same base length as for the optic fibers sensor. For LB3 the damaged sensor was placed as FO-C1-7, hence LVDT 15 replaced FO-C1-7 for LB3.

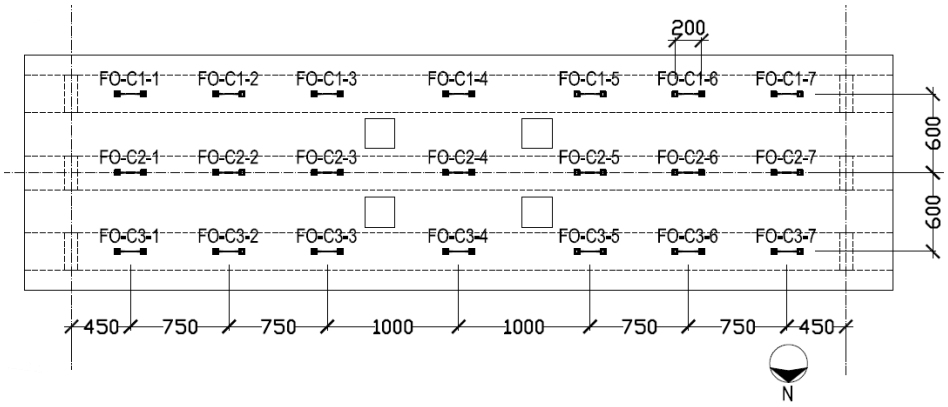

Fig.2.24. LB1 - Top view fiber optic position.

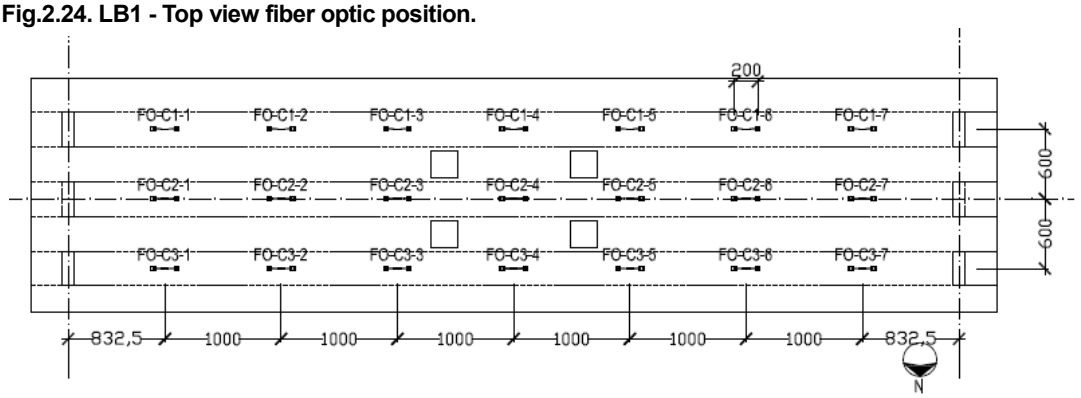

Fig.2.25. LB3 - Top view fiber optic position.

Fig.2.26. Fiber optic glued to the top of the specimen.

Fig.2.27. Fiber optic glued to the bottom of a steel beam.

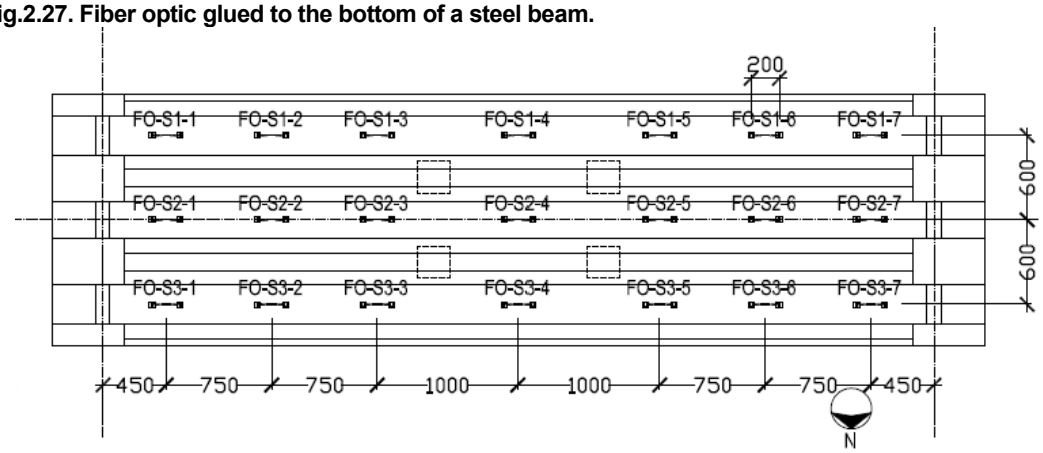

Fig.2.28. LB1 - Bottom view fiber optic position.

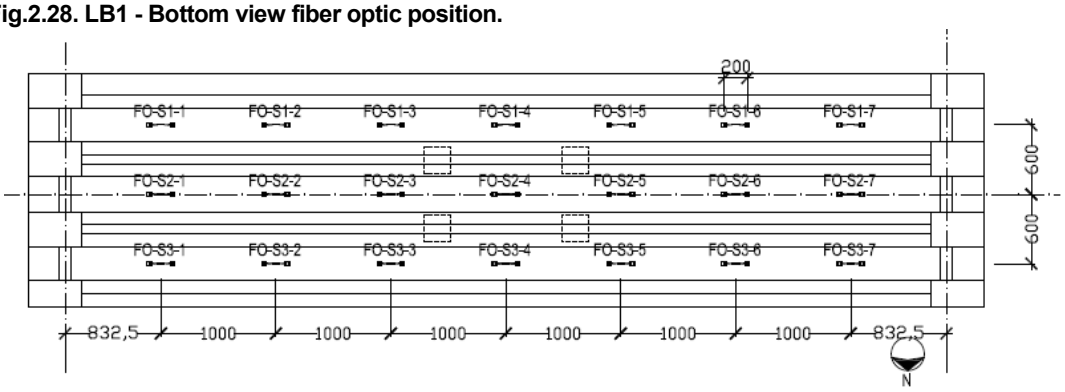

Fig.2.29. LB3 - Bottom view fiber optic position.

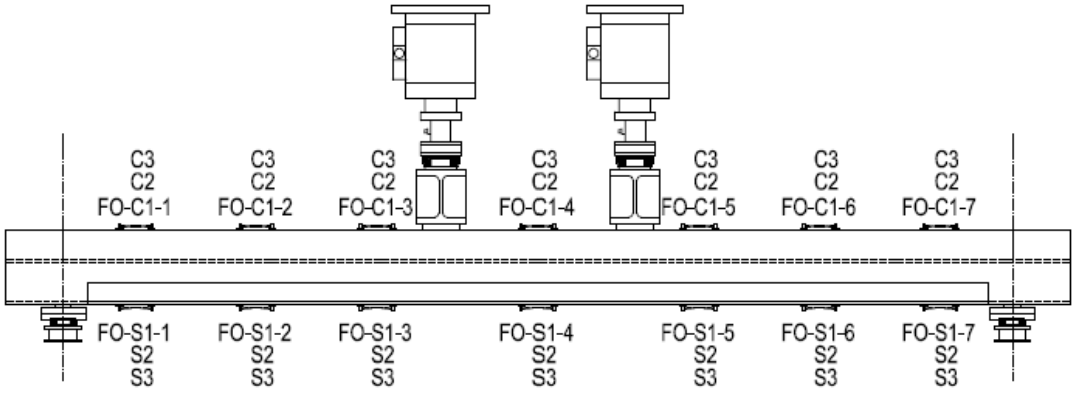

Fig.2.30. LB1 - Side view fiber optic position.

2.2.5. Digital Image Correlation (DIC)

For measuring the displacement field, principal strain distribution and cracks both 2D DIC and 3D DIC were applied. 2D DIC is composed by only one camera, and therefore able to measure the displacements field in a plane. Where out of plane deformations are expected or the measured surface is not contained in a plane, a system with two cameras is used to perform a 3D DIC.

The 2D DIC was positioned on the side of the specimens, as shown on Fig.2.31 and Fig.2.32, respectively for LB1 and LB3. Fig.2.33 showing the setup with camera and flashlight of the 2D DIC. 3D DIC was placed underneath the specimens because the bottom surface was 3-dimensional and out-of-plane deformations are expected. Fig.2.34 and Fig.2.35 shows the position of the 3D DIC for LB1 and LB3. Fig.2.36 showing the camera setup for the 3D DIC.

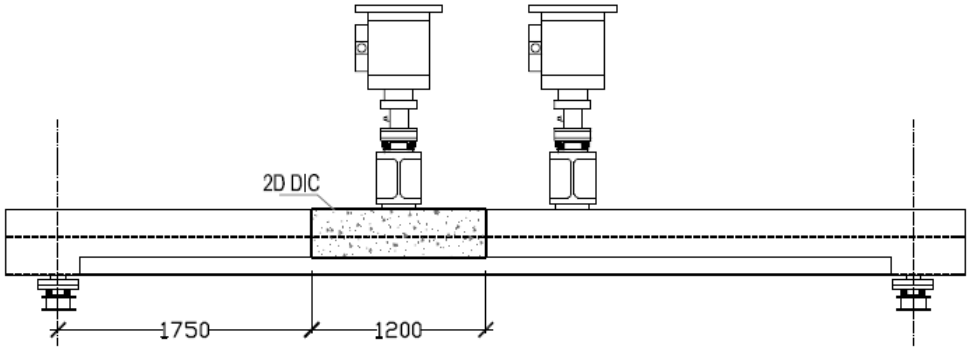

Fig.2.31. LB1 - North view 2D DIC position.

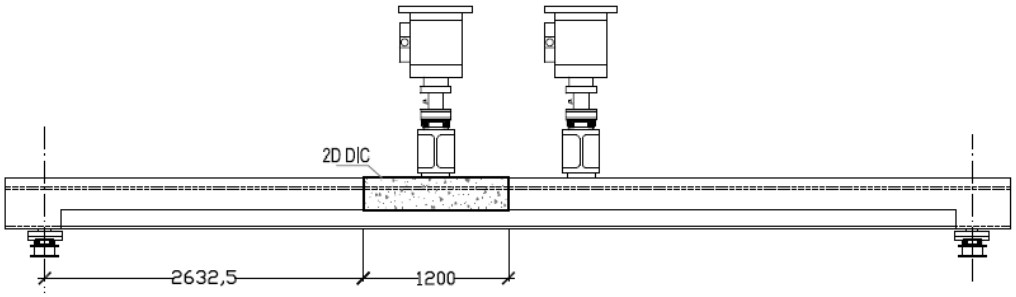

Fig.2.32. LB3 - North view 2D DIC position.

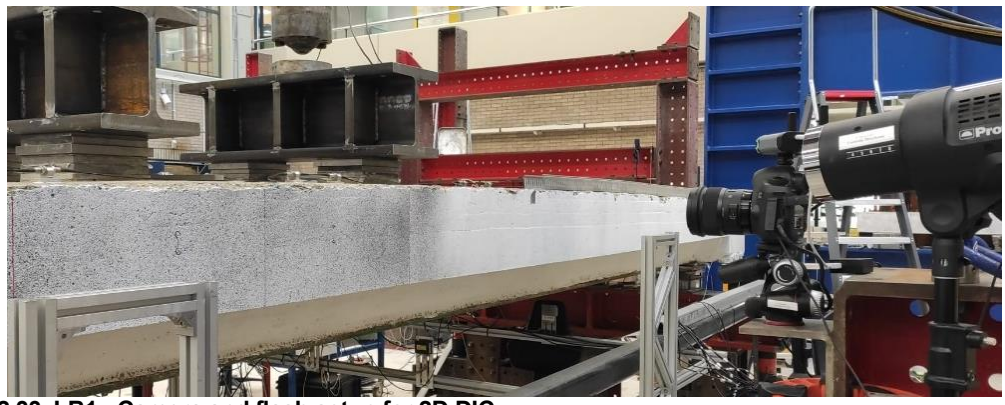

Fig.2.33. LB1 - Camera and flash setup for 2D DIC.

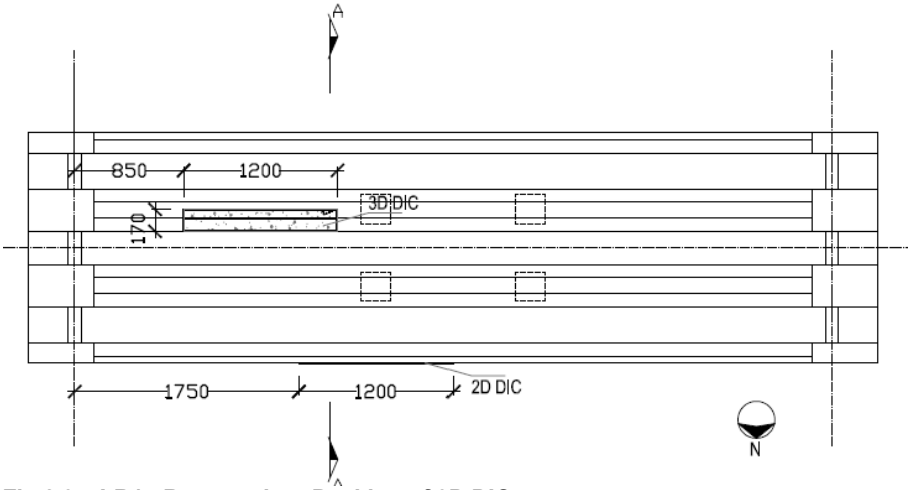

Fig.2.34. LB1 - Bottom view. Position of 3D DIC.

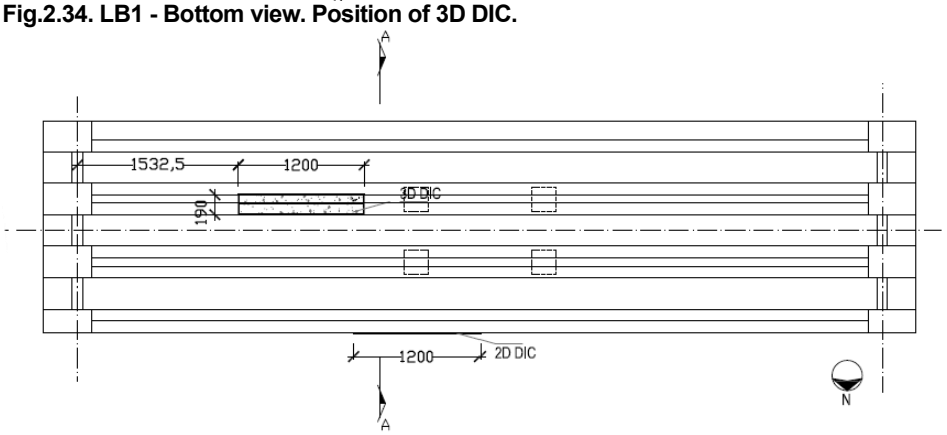

Fig.2.35. LB3 - Bottom view. Position of 3D DIC.

Fig.2.36. Camera and light setup 3D DIC.

3. RESULTS

3.1. RESULTS OF LB1

3.1.1. Detailed description of the test results

Fig.3.1 shows displacement from jack F1 versus the total load. In the following the figure will be used when describing all the experimental observations that occurred during the test of LB1.

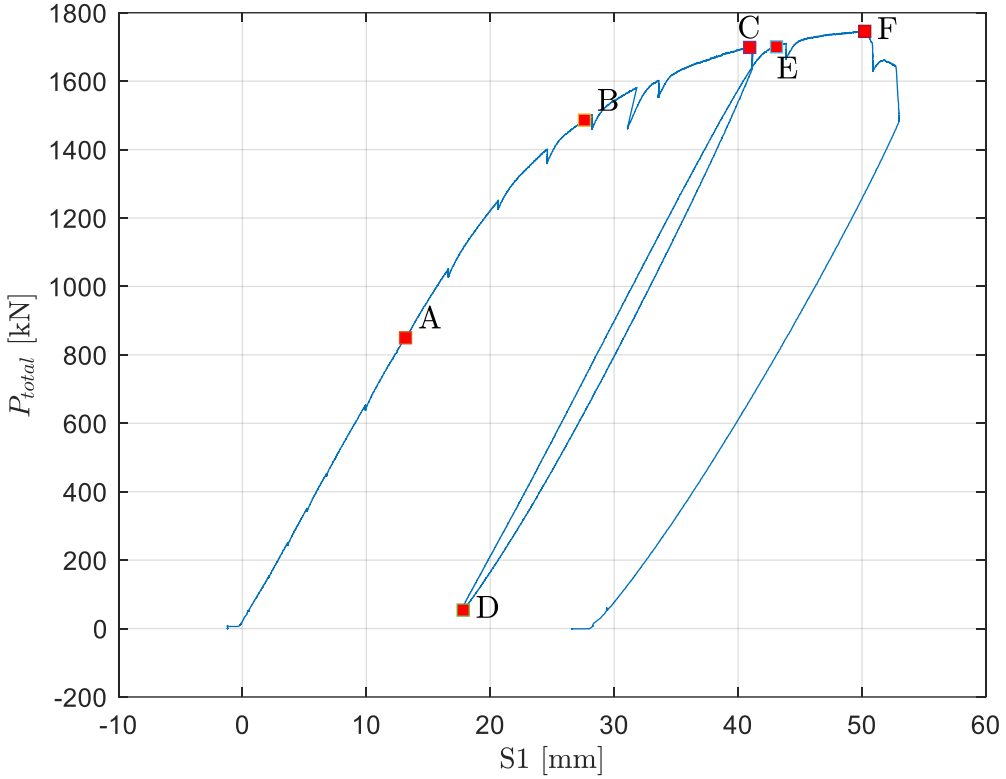

Fig.3.1. Displacement S1 on jack F1 versus total load Ptotal (sum of the forces of both jacks).

Cracking first occurred at 850 kN, point A from Fig.3.1, and the first cracks appeared as flexural cracks. The flexural cracks were first observed from the north side using the 2D DIC, but soon appeared at the 3D DIC measuring from underneath the specimen. For the 2D DIC where cracking starts see Fig.3.2.

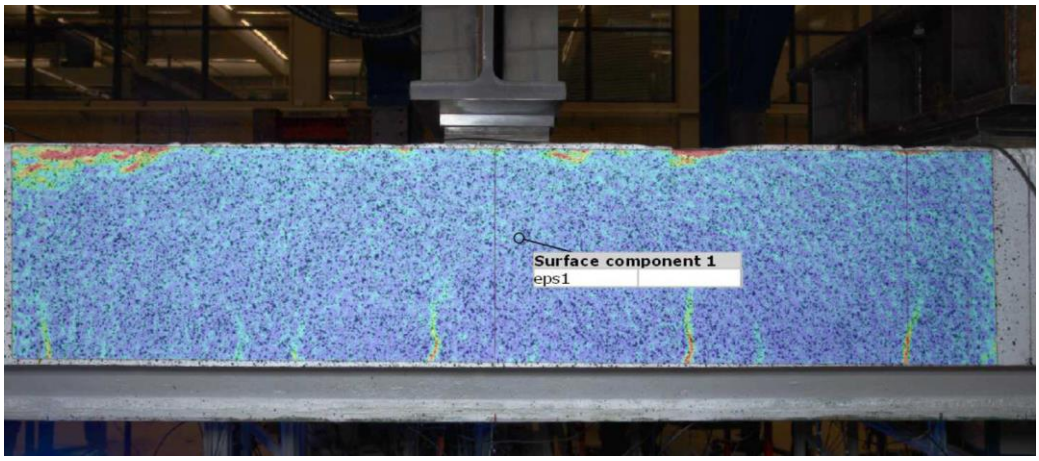

Fig.3.2. LB1. Point A – Principal strain field ε1 - Cracking starts (Ptotal=850 kN). 2D DIC from the north side.

Following cracking, yielding was first measured at mid-span from optic fiber FO-S2-4 at the bottom flange of beam 2. The yielding was observed assuming that yielding begins at 1,75‰. When yielding began, the load was 1447 kN and the adjacent beams had a strain close to yielding but only an elastic strain. The strains at 1447 kN at beams 1, 2 and 3 can be seen from Fig.3.3 and Fig.3.5.

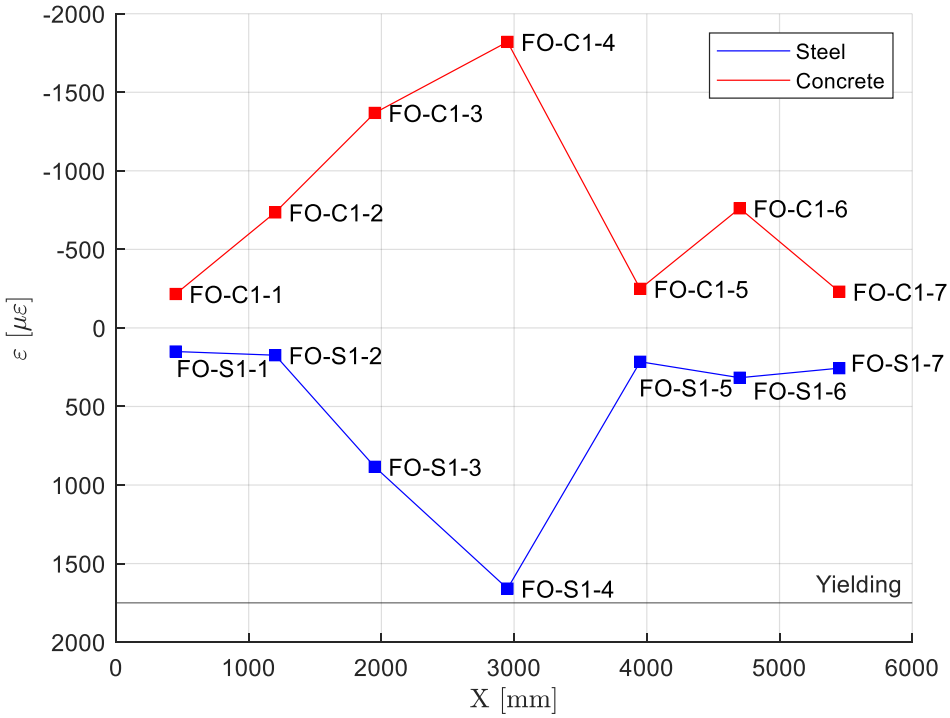

Fig.3.3. LB1. Point B – Beam 1 – Strains - Yielding starts at beam 2 (Ptotal=1447 kN). X, the position of the optic fibers from the support, versus the strain measured for optic fibers above and below beam 1.

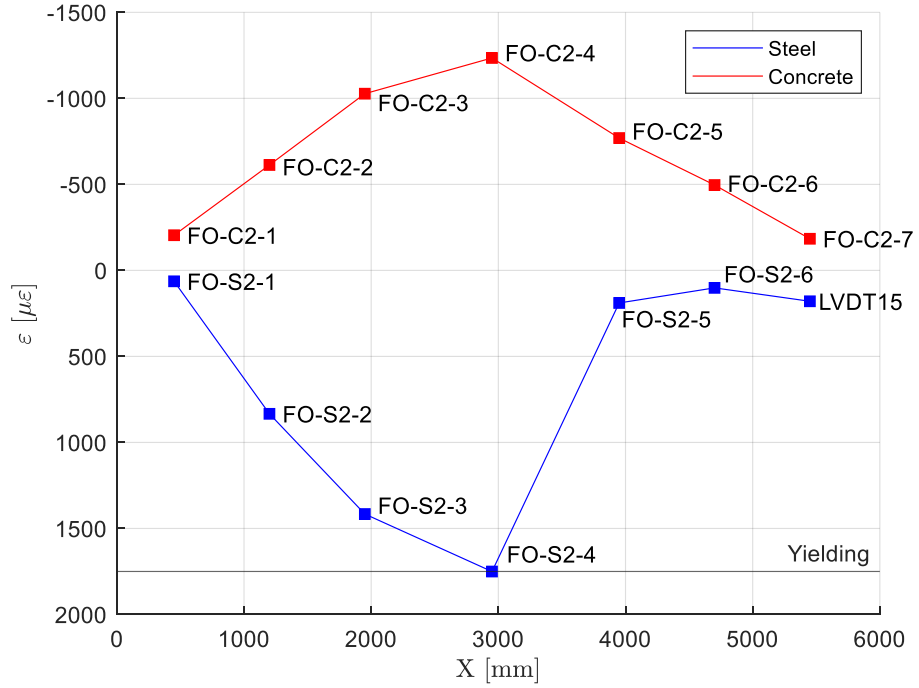

Fig.3.4.LB1. Point B –Beam 2 – Strains - Yielding starts at beam 2 (Ptotal=1447 kN). X, the position of the optic fibers from the support, versus the strain. FO-S2-7 broke during preparation of LB1 and is replaced by LVDT 15. FO-S2-5 and FO-S2-6 show smaller strains which can be considered outliers.

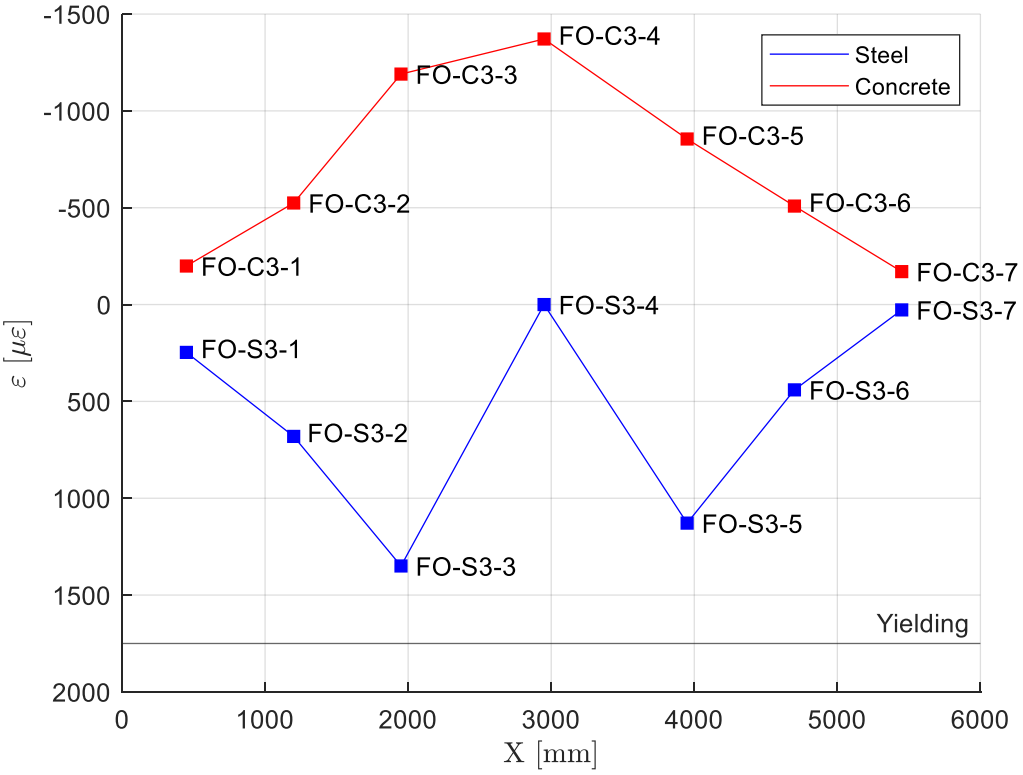

Fig.3.5. LB1. Point B – Beam 3- Strains - Yielding starts at beam 2 (Ptotal=1447 kN). X, the position of the optic fibers from the support, versus the strains. FO-S3-4 is not out of range despite the strain measured being smaller than expected therefore can be considered an outlier.

When the load reached 1700 kN, point C from Fig.3.1, the flexural cracks at the side started to propagate in longitudinal direction at a height approximately corresponding to the top flange of the beams. Moreover, the cracks underneath the specimen started to propagate in longitudinal direction when yielding began, this was observed from the 3D DIC. Underneath the specimen, the cracks closest to the supports were propagating into one continuous crack. The 2D and 3D DIC at 1700 kN can be seen from Fig.3.6 and Fig.3.7.

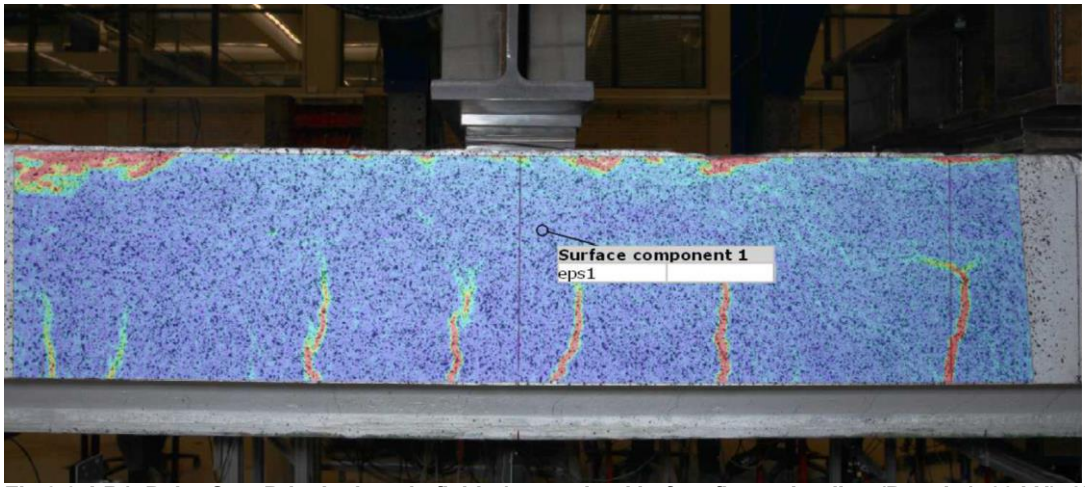

Fig.3.6. LB1. Point C - – Principal strain field ε1 - max load before first unloading (Ptotal=1700 kN). 2D DIC from the north side.

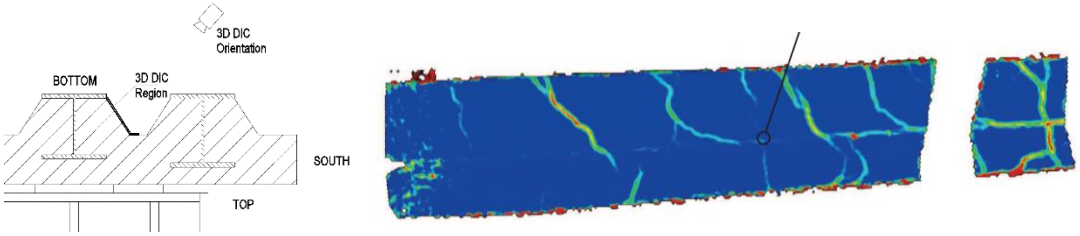

Fig.3.7. LB1. Point C - Principal strain field ε1 - Bottom surface of the concrete.- Max load before first unloading (Ptotal=1700 kN). 3D DIC from underneath the specimen.

At 1700 kN the max strain of the top concrete layer was 2,0‰ and was at midspan of the specimen measured from optic fiber FO-C2-4. The strain of the concrete didn't change significantly when increasing the load in the following. Furthermore, the yielding of 2 beam propagated as yielding was measured at both optic fibers FO-S2-3 and FO-S2-4 at the bottom flange. In addition, the strain at the optic fibers FO-S2-5 and FO-S2-6 was relatively small indicating that either there was an error with the optic fibers or that the behaviour of the beam was different at this position. The strain at 1700 kN for beam 2 is shown at Fig.3.8.

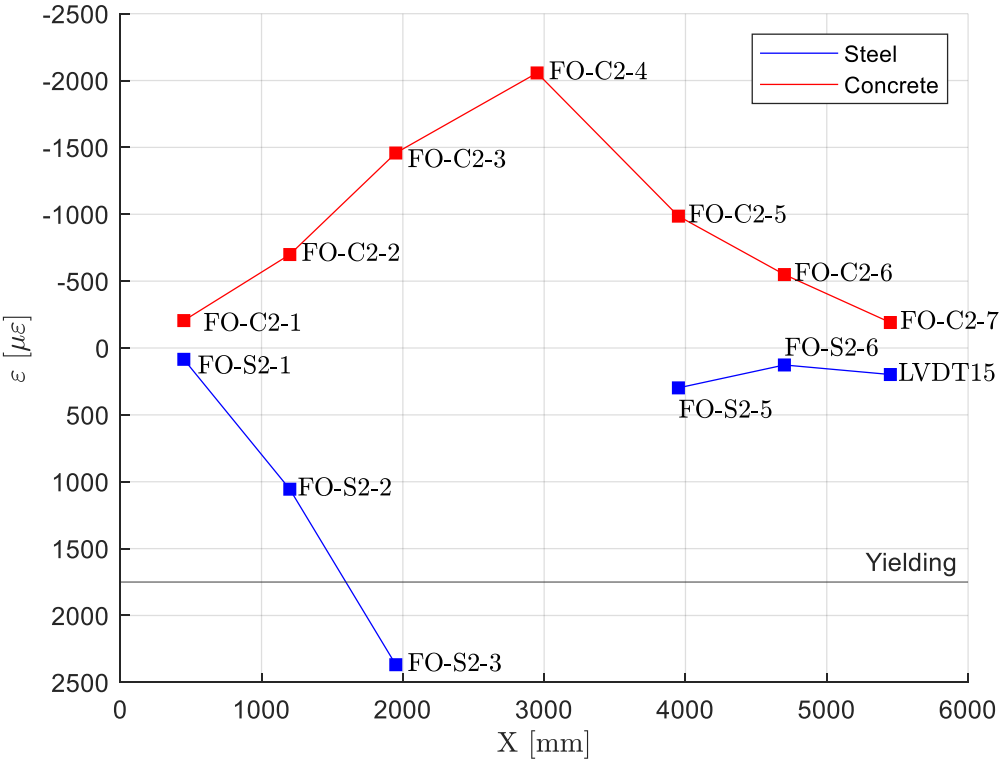

Fig.3.8. LB1. Point C - Max load of first loading (Ptotal=1700 kN). X, the position of the optic fibers from the support, versus the strain measured for optic fibers above and below beam 2. FO-S2-4 fell out of range. FO-S2-7 broke during preparation of LB1 and was replaced by LVDT 15.

After the load reached 1700 kN, point C from Fig.3.1, the specimen was unloaded to 50 kN to preserve the measuring devices, point D from Fig.3.1. From the unloading an irreversible vertical deformation of the specimen was observed, which shows the plastic behaviour of the specimen. The maximum displacement measured from lasers during unloading was 16 mm, measured from laser 5 that is underneath beam 2. Furthermore, the vertical displacement was not symmetrically perfect, due to small variations of the cross section over the length of the specimen. The vertical deformation measured from beam 2 is shown at Fig.3.9 at different load points.

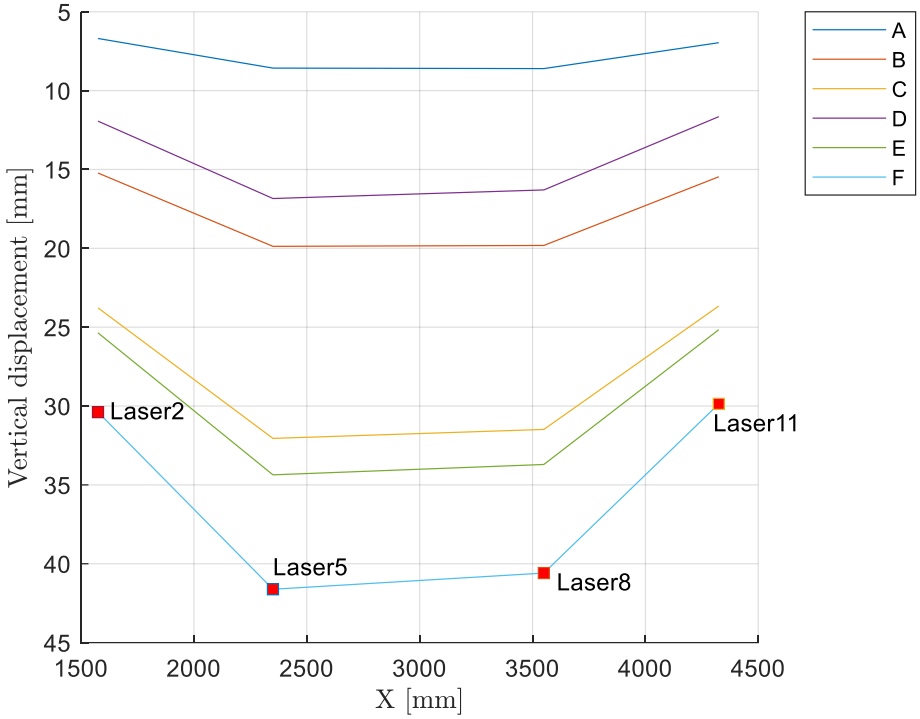

Fig.3.9. LB1. Displacement profile at beam 2 for different load levels (A-F from Fig.3.1). Laser 2, 5, 8 and 11 positioned at beam 2. X, distance to the support, versus the total vertical displacement.

After the specimen was unloaded to 50 kN, point D from Fig.3.1, the specimen was reloaded again. During reloading the deformation of the specimen was increasing linearly with increasing load, until 1600 kN and the specimen started to yield again. When the specimen reached 1700 kN again, point E from Fig.3.1, the displacement started to increase with the same displacement versus load gradient as before it was unloaded to 50 kN. This development during the reloading can be seen from Fig.3.1.

The specimen failed after reloading at 1746 kN, point F from Fig.3.1,. Following the failure, a sudden load drop occurred, and the beam was unloaded. At this load level, delamination between steel and concrete occurred at beam 1. The delamination crack progated through the hole beam reaching also the support. See Fig. 3.10, Fig.3.11, Fig.3.12.

Fig. 3.10 - LB1 - Delamination crack observed at Ptotal = 1746 kN. Steel beam 1. Picture from south view.

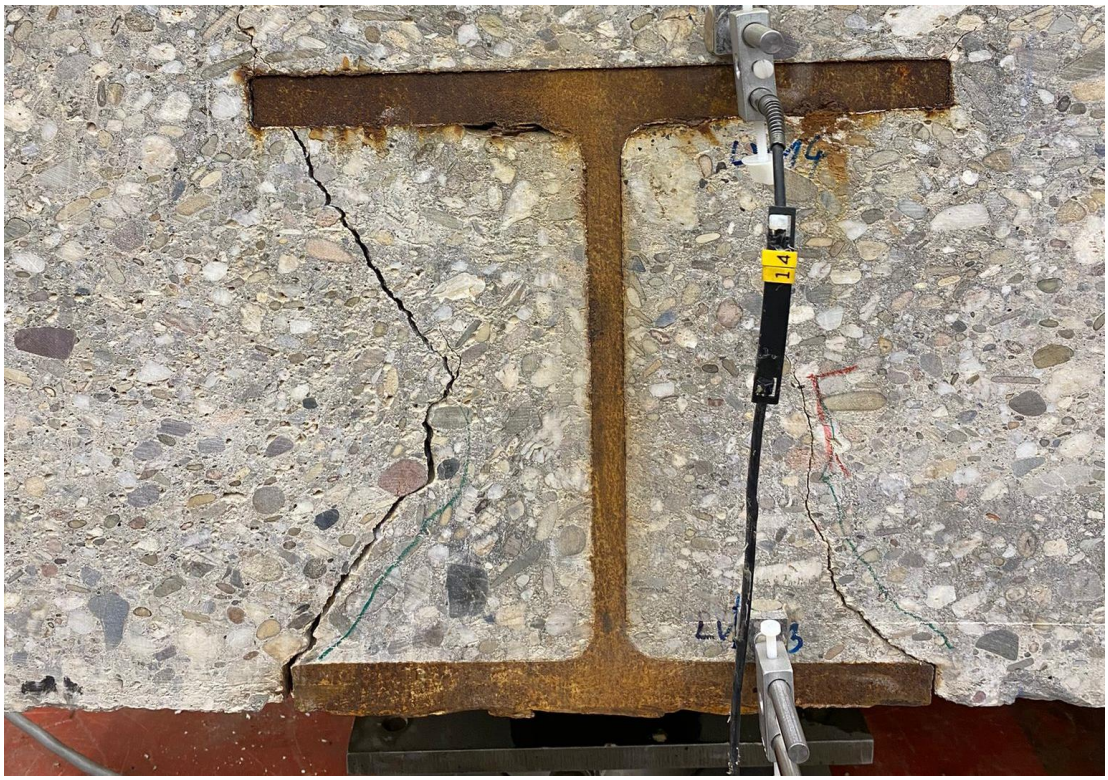

Fig.3.11. LB1. Cracks between flanges of beam 1 at the east end after testing.

Fig.3.12. LB1. Crack at the west end of beam 1 after testing.

The delamination was also measured at LVDT14 which during most of the experiment had values close to zero until the delamination crack propagated until the support and the displacement increased significantly. See Fig. 3.13.

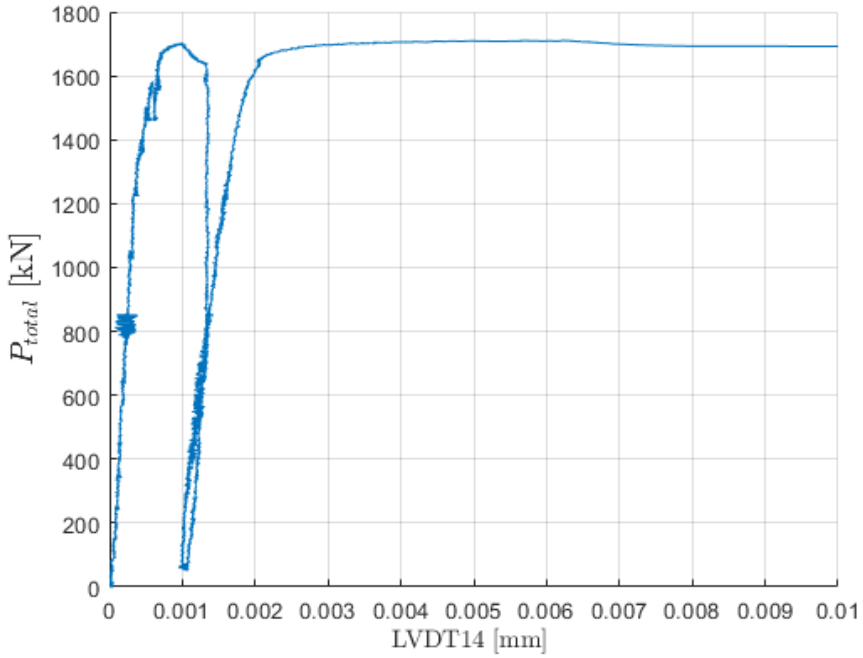

Fig. 3.13 - LB1 - Relative displacement between steel top flange and adjacent concrete at Beam 1 end. The maximum relative displacement measured was 1mm, the graph is limited to keep scale.

A similar behaviour was observed at LVDT 12 which activated showing slip of the beams at the top flange. LVDT 12 measuring slip at beam 1 showed a trend like the vertical displacement, whereas LVDT 14 measuring slip at beam 2 only showed slip at failure. LVDT 12 can be seen on Fig.3.14. LVDT 11 and 13, showed small values of relative displacement.

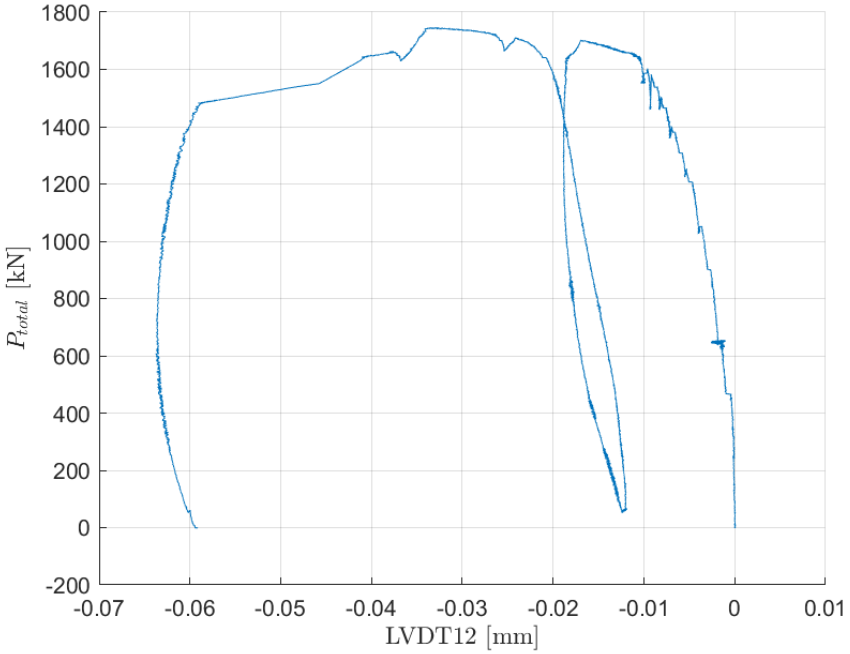

Fig.3.14. LB1. Longitudinal displacement at top flange of beam 2 versus total load.

LVDTs 1-4 measuring relative longitudinal displacement were activated especially LVDT 2 and 3, when the load increased from 1700 kN to 1746 kN, which can be seen from Fig.3.15.

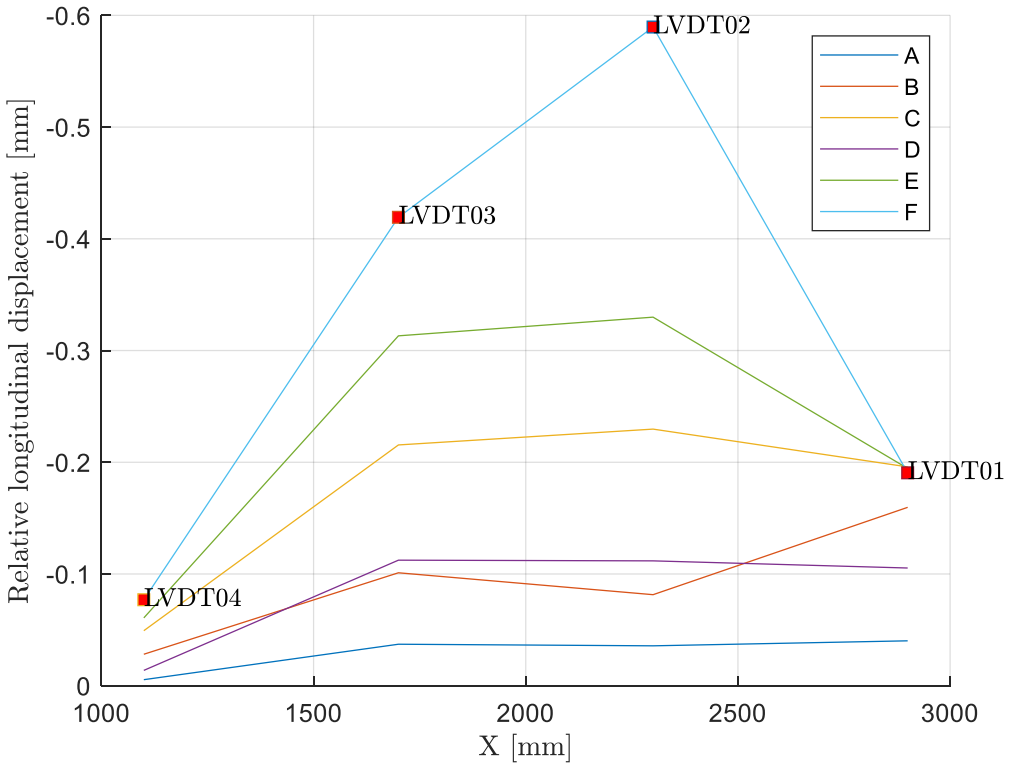

Fig.3.15. Point A-F for LVDT 1-4. Relative longitudinal displacement between steel and concrete versus X, the distance to the support.

Flexural cracks propagated in longitudinal direction at a height around the position of the top flange, especially on the region where the load was applied. The 2D DIC at failure can be seen from Fig.3.16.

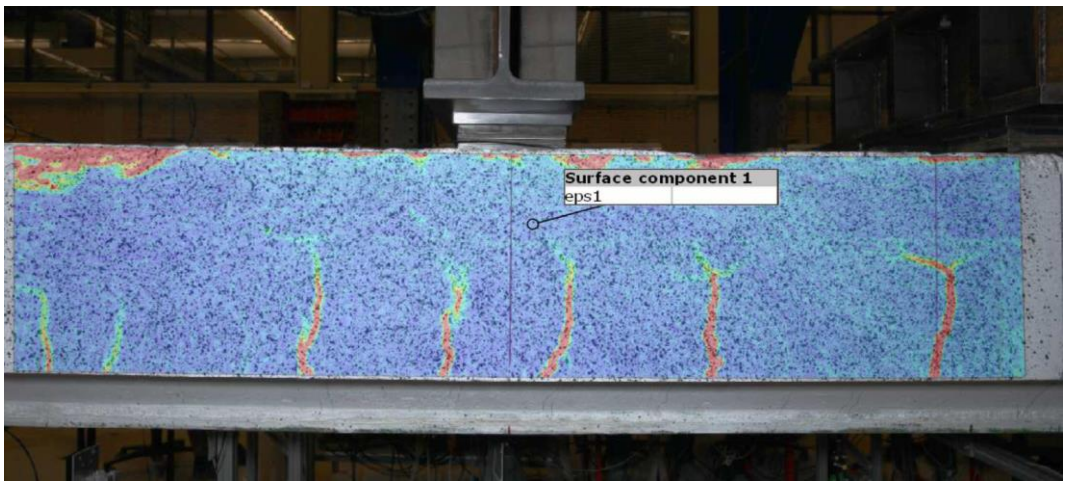

Fig.3.16. LB1. Point F - the max load is achieved (Ptotal=1746). 2D DIC from the north side.

From the south side delamination cracks were observed at beam 1 that propagated to the support at load cell 4, which can be seen from, Fig. 3.10 and Fig.3.17**Error! Reference source not found.**. At the west end of the specimen there was a gap between beam 1 and the concrete, which can be seen from Fig.3.12. At the east side there were cracks in the concrete between the top and bottom flanges of beam 1, which can be seen from Fig.3.11. Underneath the specimen there was a longitudinal crack between beams 1 and 2 going from support to support which can be seen from Fig.3.18.

Fig.3.17. LB1. Crack from the east support along beam 1.

Fig.3.18. LB1. Crack between beam 1 and 2 underneath the specimen. The crack was observed after the test.

LVDT 2 and 3 registered an increase in the displacement at failure, additionally LVDT 14 showed that beam 2 slipped at failure. Before failure LVDT 14 wasn't activated, despite LVDT 2 and 3 showed increasing displacement between the bottom flange of beam 2 and the bottom concrete layer. From the cracks seen between beam 1 and the concrete, as well as the before mentioned

indicates that failure of interface was observed, although the specimen had bending behavior but with limited ductility.

The load distribution among the three beams can be obtained by analyzing the load cells measurements It was observed that the middle beam carried a higher portion of the loads. See Fig. 3.19 and Fig. 3.20. Moreover the response is not completely symmetric.

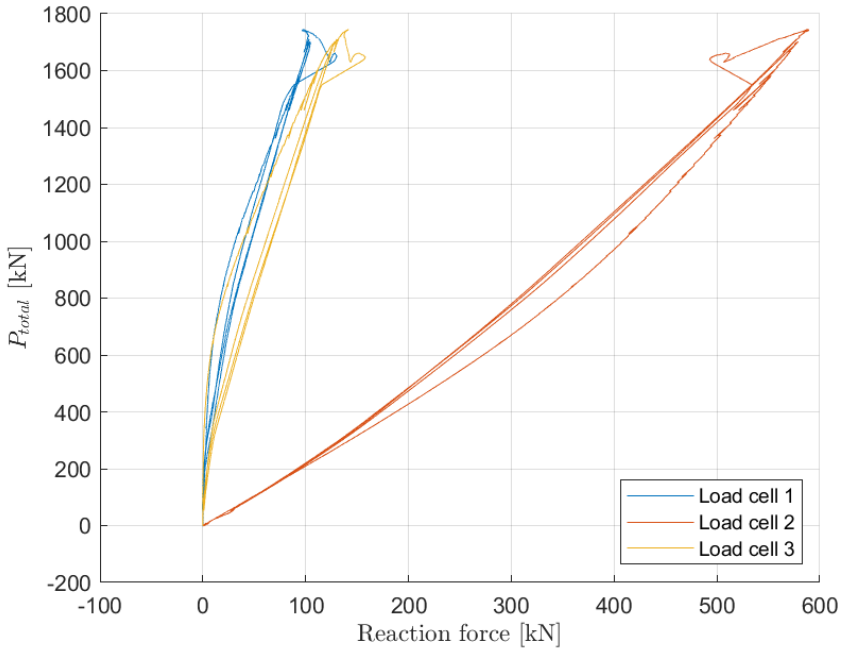

Fig. 3.19 – LB1 - Reaction force from load cells versus total load for load cell 1-3, west side.

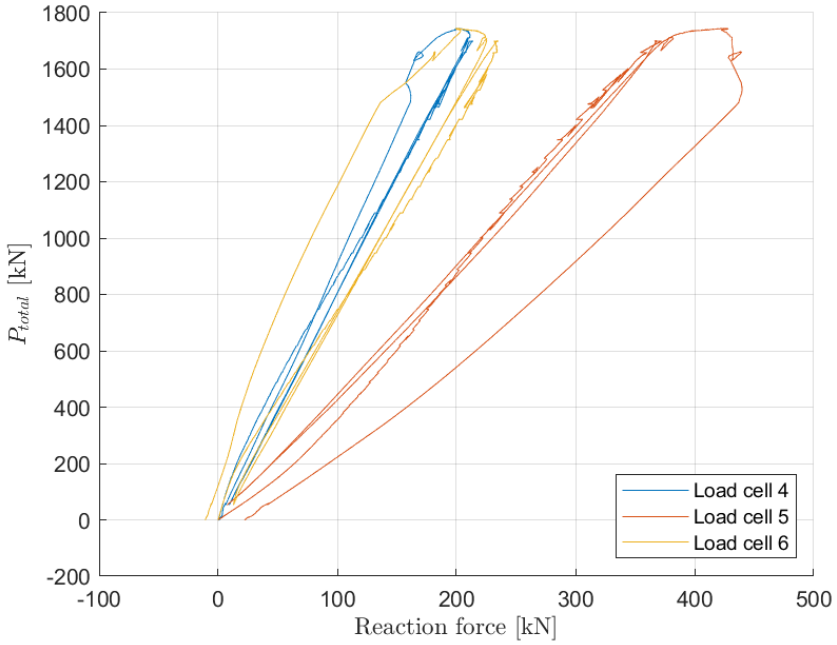

Fig. 3.20 – LB1 - Reaction force from load cells versus total load for load cell 4-6, east side.

On the transverse displacements of the beams, it was observed that Beam 1 (southern beam) experienced a bigger transverse displacement from the middle than Beam 3 (northern beam). This can be seen on the measurements of LVDTs 5 and 6 (LVDTs 7-10 showed a similar behavior), see Fig. 3.21.

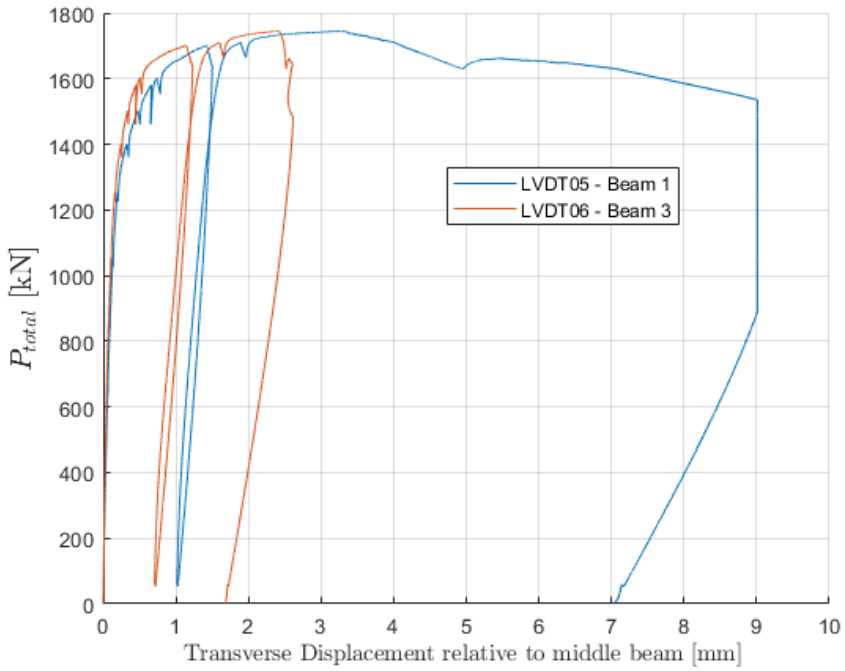

Fig. 3.21- LB1 - Relative transverse displacements from the outer beams measured from the bottom flange.

Regarding the vertical displacement, on a section located under the load it can be seen, Fig. 3.22, that beam 3 had a slightly bigger displacement than beam 1, and that the biggest displacement was under the middle beam.

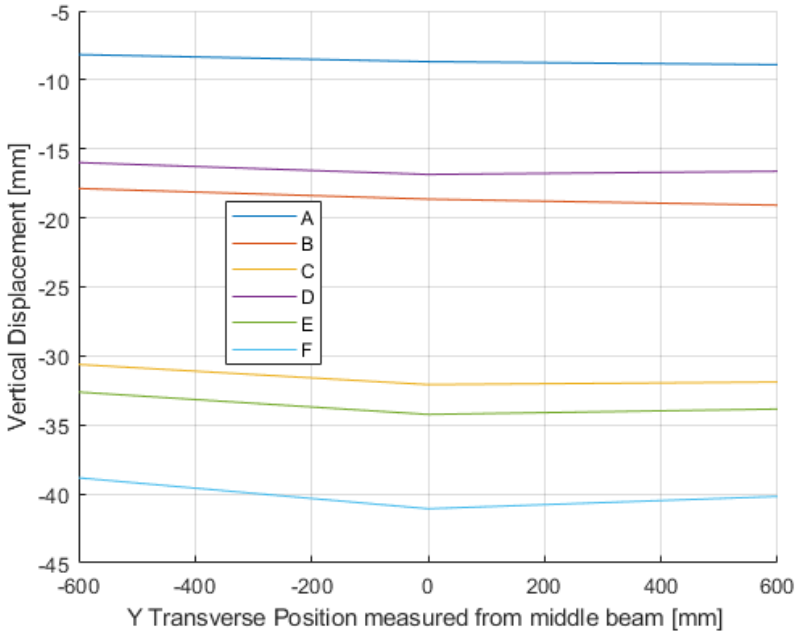

Fig. 3.22 - LB1 - Vertical displacement transverse distribution between the three steel beams for different load stages (A-F). Measurements from Lasers 4, 5 and 6.

Other test results for load cells, optic fibers, lasers, LVDTs, 2D DIC and 3D DIC are shown respectively at Annex A to F.

3.2. RESULTS OF LB3

3.2.1. Detailed description of the test results

Fig.3.23 shows displacement from jack F1 versus the total load. In the following the figure will be used when describing all the experimental observations that occurred during the test of LB3.

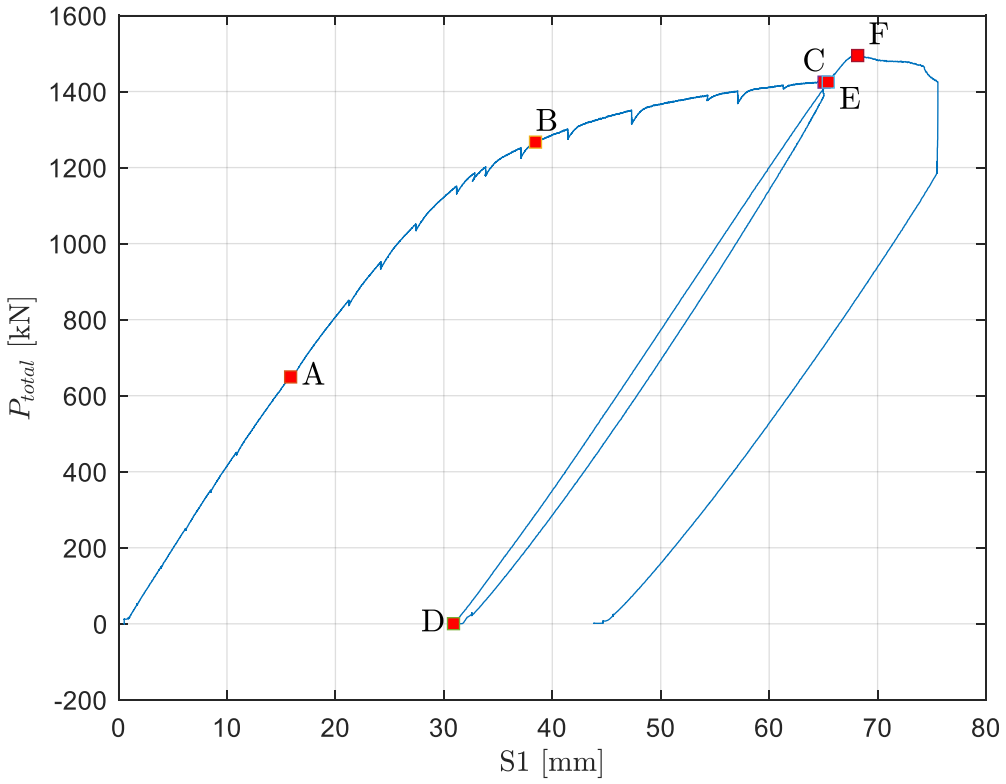

Fig.3.23. Displacement S1 at jack F1 versus total load (sum of both jacks). Characteristic load points shown with capital letters.

Cracking first occurred at 650 kN, point A from Fig.3.23. The first cracks appeared as flexural cracks, these were first observed from the north side of the specimen, using 2D DIC, at this point cracking was also visible from the 3D DIC positioned underneath the specimen. The 2D and 3D DIC at 650 kN can be seen from Fig.3.24 and Fig.3.25.

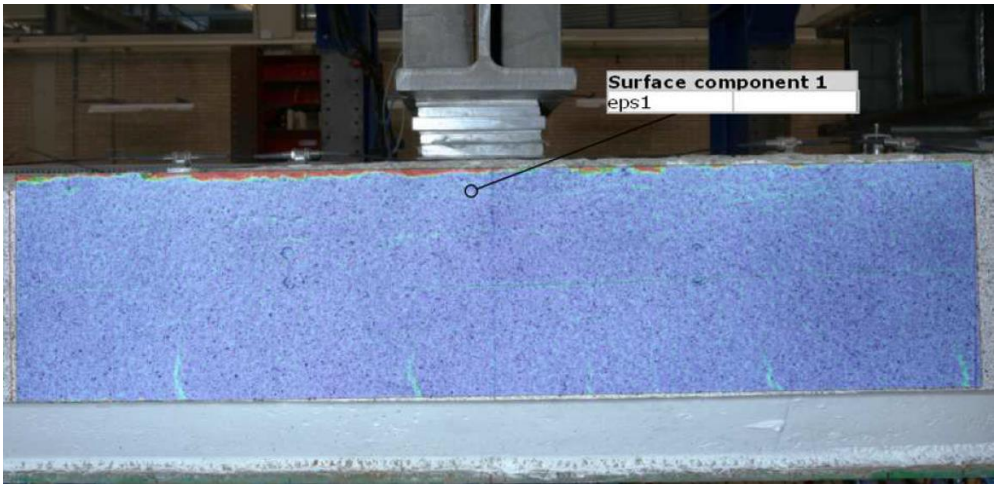

Fig.3.24. LB3. Point A – Principal strain field ε1 - Cracking starts (Ptotal=650 kN). 2D DIC from the north side.

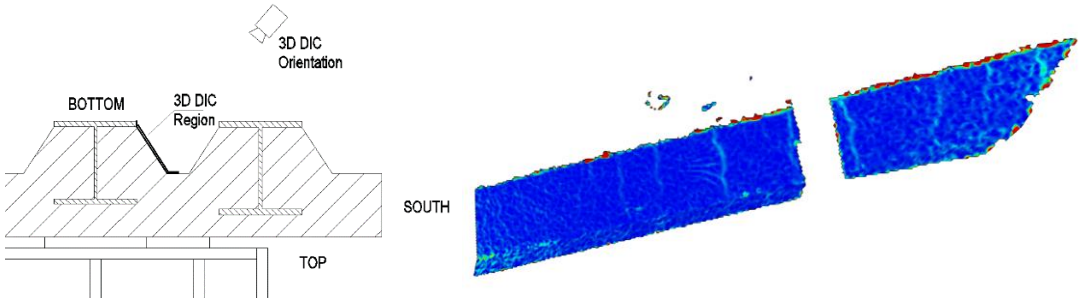

Fig.3.25. LB3. Point A – Principal strain field ε1 - Bottom surface of the concrete - Cracking starts (Ptotal=650 kN). 3D DIC from underneath the specimen.

Following cracking, yielding was first measured at 1267 kN close to mid-span at beam 3 from optic fiber FO-S3-5. At this point FO-S3-4 measured relatively low values, although it was expected that this would measure the highest strains at beam 3, later FO-S3-4 obtained values that seemed reasonable. The maximum strain of the top concrete layer was in the range 2,0‰, measured at midspan from optic fiber FO-C1-4. The strain for beams 1, 2 and 3 are shown at Fig.3.26 to Fig.3.28.

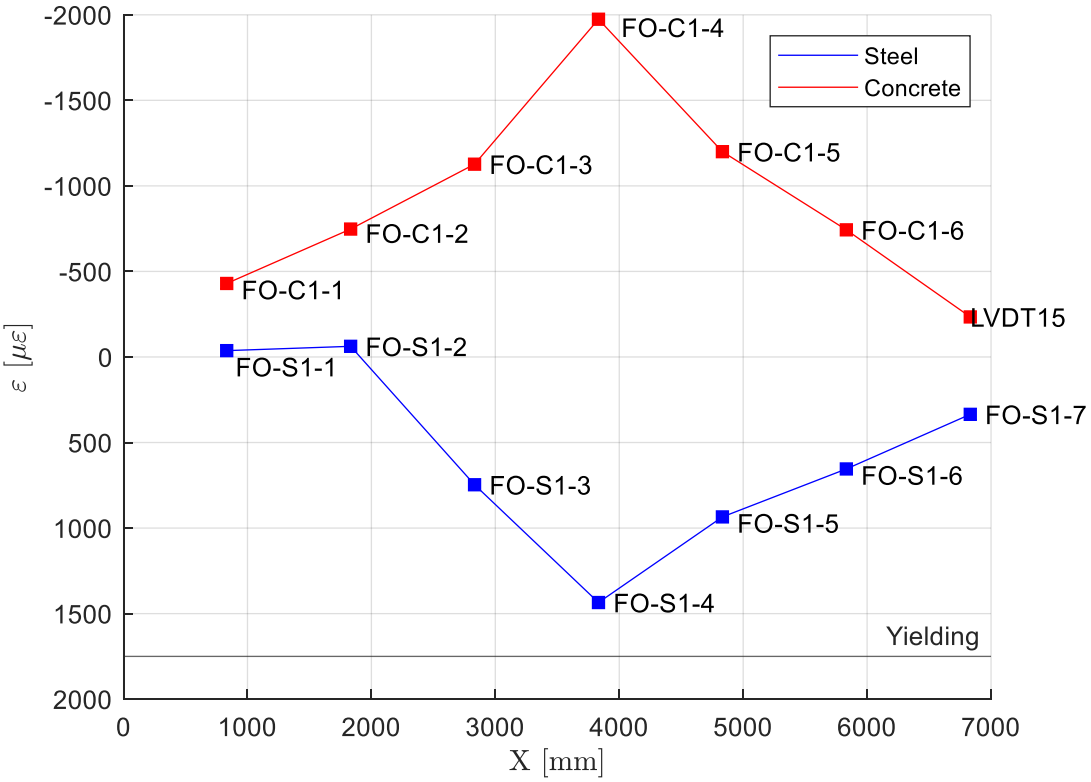

Fig.3.26. LB3. Point B – Beam 1 – Strains - Yielding starts at beam 3 (Ptotal=1267 kN). X, the position of the optic fibers from the support, versus the strain. FO-C1-7 broke during preparation of LB1 and was replaced by LVDT 15.

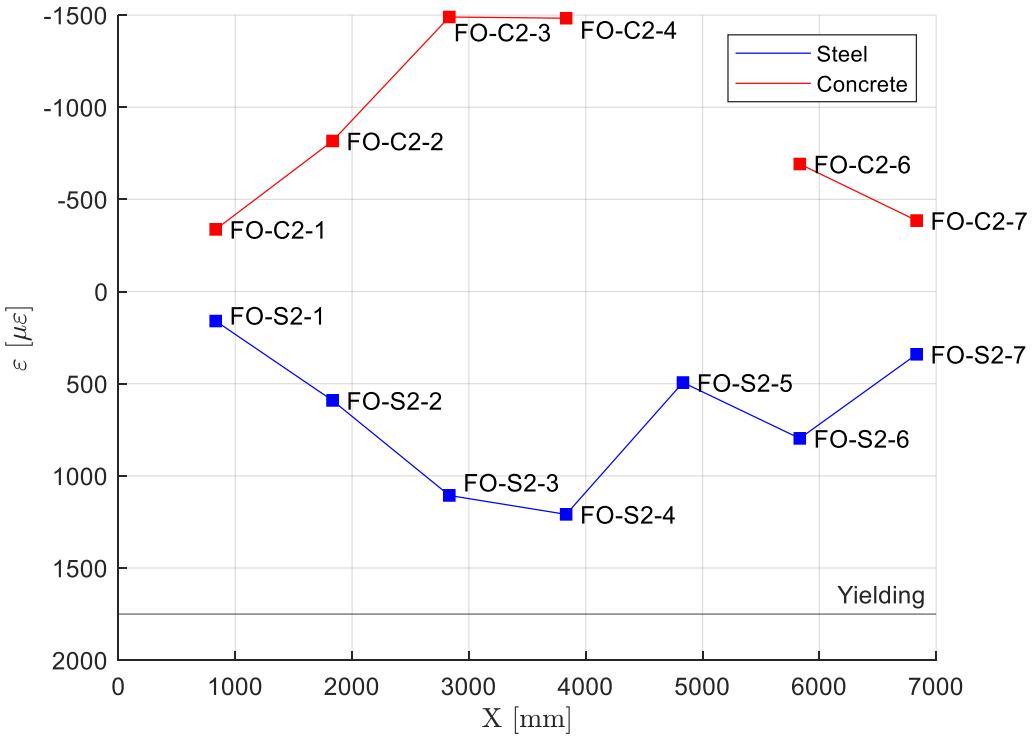

Fig.3.27. LB3. Point B- Beam 2 – Strains - Yielding starts at beam 3 (Ptotal=1267 kN). X, the position of the optic fibers from the support, versus the strain. FO-C2-5 fell out of range.

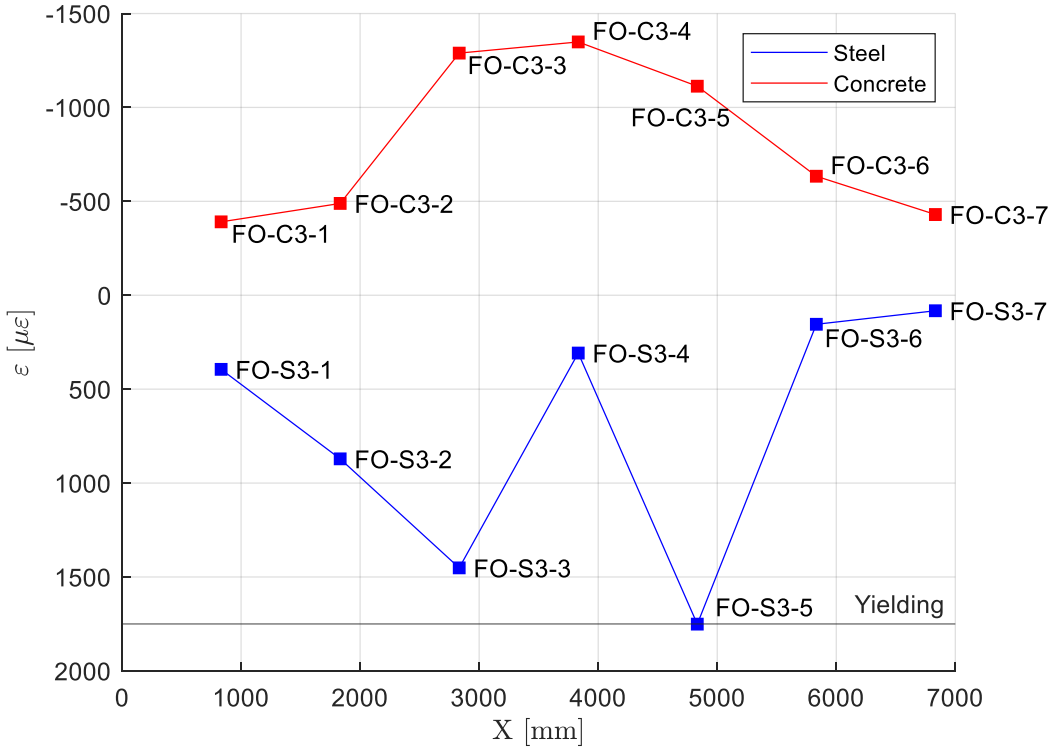

Fig.3.28. LB3. Point B - Yielding starts at beam 3 (Ptotal=1267 kN). X, the position of the optic fibers from the support, versus the strain 3. FO-C2-5 fell out of range. FO-S3-4 shows inconsistent values and can be seen as an outlier.

At 1267 the 2D DIC showed horizontal cracks at the top half of the concrete layer which can be seen as initiation of concrete crushing. At this level concrete compressive strains were 2000με at mid span as it was measured it can be seen in Fig.3.26. In addition, the flexural cracks started to propagate in longitudinal direction, without reaching the position of the top flange of the steel beams. Moreover, the cracks underneath the specimen had grown and became more visible. The 2D and 3D DIC at 1267 kN is shown at Fig.3.29 and Fig.3.30.

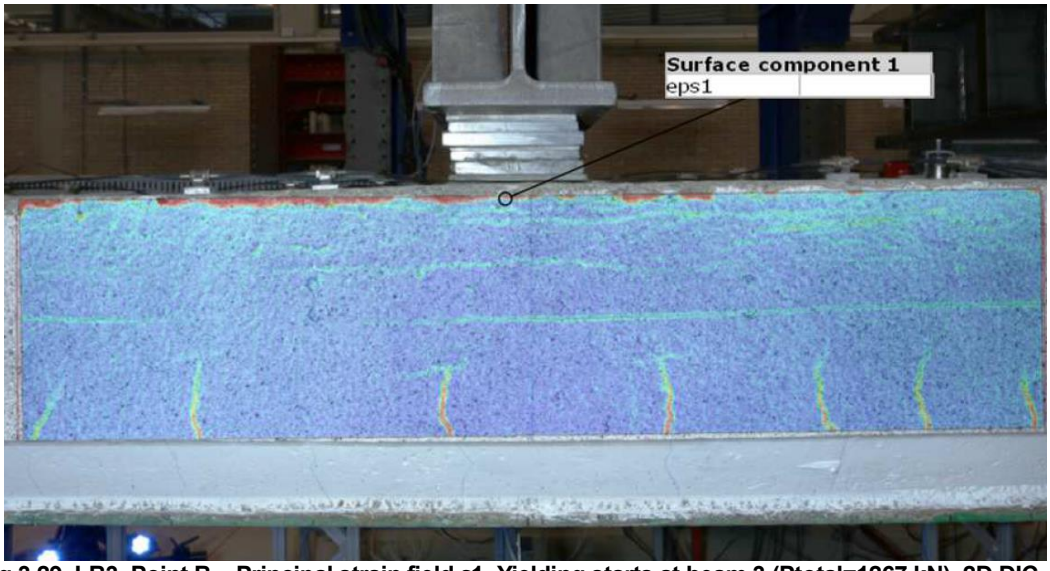

Fig.3.29. LB3. Point B – Principal strain field ε1- Yielding starts at beam 3 (Ptotal=1267 kN). 2D DIC from the north side.

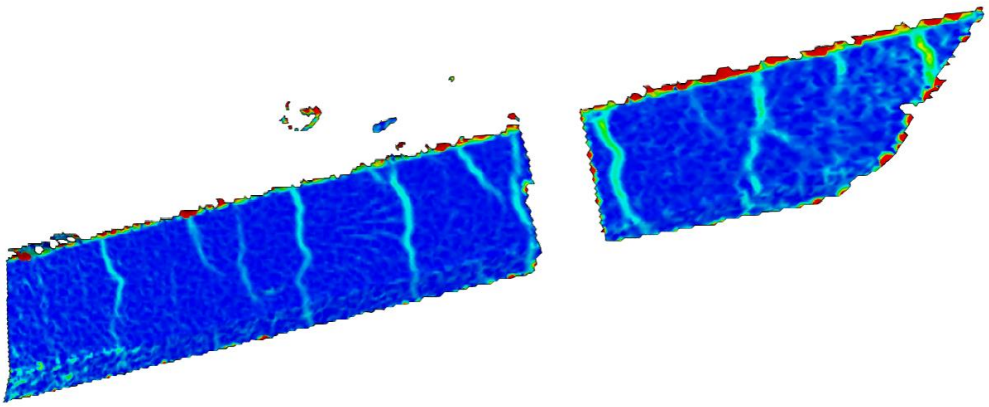

Fig.3.30. LB3. Point B – Principal strain field ε1- Bottom surface of the concrete -Yielding starts (Ptotal=1267 kN). 3D DIC from underneath the specimen.

When the maximum displacement range was achieved at 1426 kN, point C from Fig.3.23, the 2D DIC showed that the flexural cracks had propagated to approximately the position at the top flange of the steel beams, which is shown at Fig.3.31.

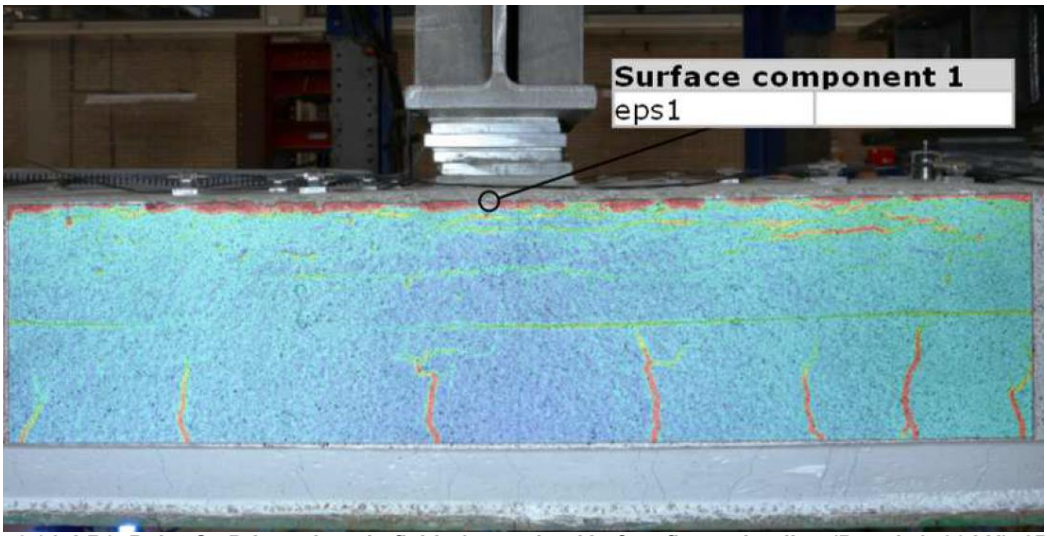

Fig.3.31. LB3. Point C –Princpal strain field ε1- max load before first unloading (Ptotal=1426 kN). 2D DIC from the north side.

At 1426 kN, the specimen was unloaded to 0 kN, point D from Fig.3.23, to increase the displacement range further. From the unloading an irreversible vertical deformation of the specimen was observed, which showed the plastic behaviour of the specimen, this can be seen from Fig.3.23. At 0 kN the vertical displacement of the specimen was close to the vertical displacement of the specimen when cracking first occurred, see Fig.3.32. Following the unloading to 0 kN, the specimen was loaded again, but without the optic fibers and 2D and 3D DIC, hence these will not be included in the following description.

When the load again reached 1426 kN, point E from Fig.3.23, the vertical displacement at mid-span had increased by approximately 20 mm, compared to when it reached 1426 kN before the unloading, point C from Fig.3.23, which can be seen at Fig.3.32 for laser 6 and 9. As can be seen from the figure the response is not perfectly symmetric, but the difference is small, this is because the specimen's cross section has small variations over the length.

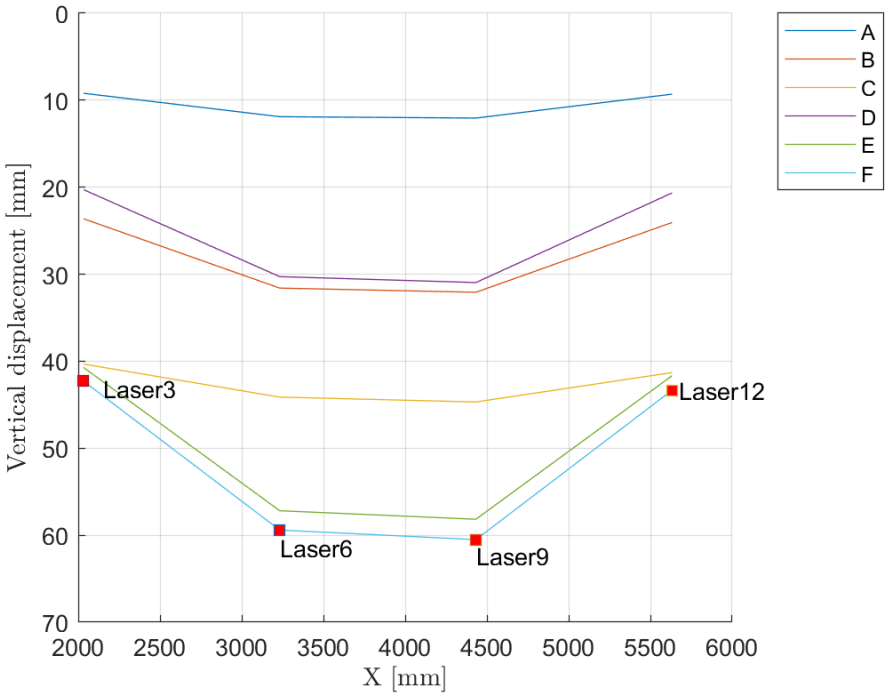

Fig.3.32. LB3. Vertical displacements under beam 3 at different load levels (Point A-F) for laser 3, 6, 9 and 12. X, distance to the support, versus the total vertical displacement.

Between 1426 kN and 1494 kN, point F from Fig.3.23, the vertical displacement merely increased with 3 mm measured from laser 6 and 9. The vertical displacement increased linearly with increasing load during the reloading, till the specimen failed at 1494 kN,

Following the failure, crushing occurred at the top layer of the concrete, see Fig.3.33.

Fig.3.33. LB3. Mid-span from south side after testing showing cracks and crushing.

At failure LVDT 1 and 2 were activated, whereas LVDT 3 and 4 were almost constant throughout the entire testing, see Fig.3.34. In addition, LVDT 11-14 measuring relative longitudinal displacement at the end of the specimen, were not activated, indicating that no slip occurred.

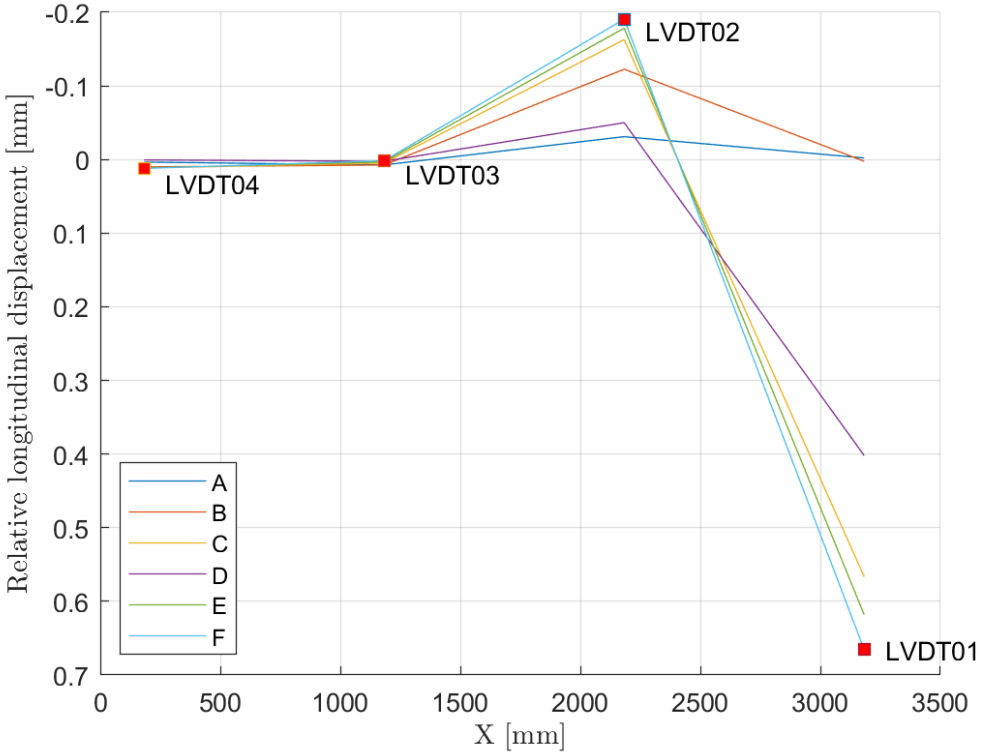

Fig.3.34. LB3. Point A-F for LVDT 1-4. Relative longitudinal displacement between steel and concrete versus X, the distance to the support.

The load distribution among the three beams can be obtained by analyzing the load cells measurements It was observed that the middle beam carried a much higher portion of the loads. See Fig. 3.35 and Fig. 3.36Fig. 3.20. Moreover the response is not symmetric on the longitudinal direction.

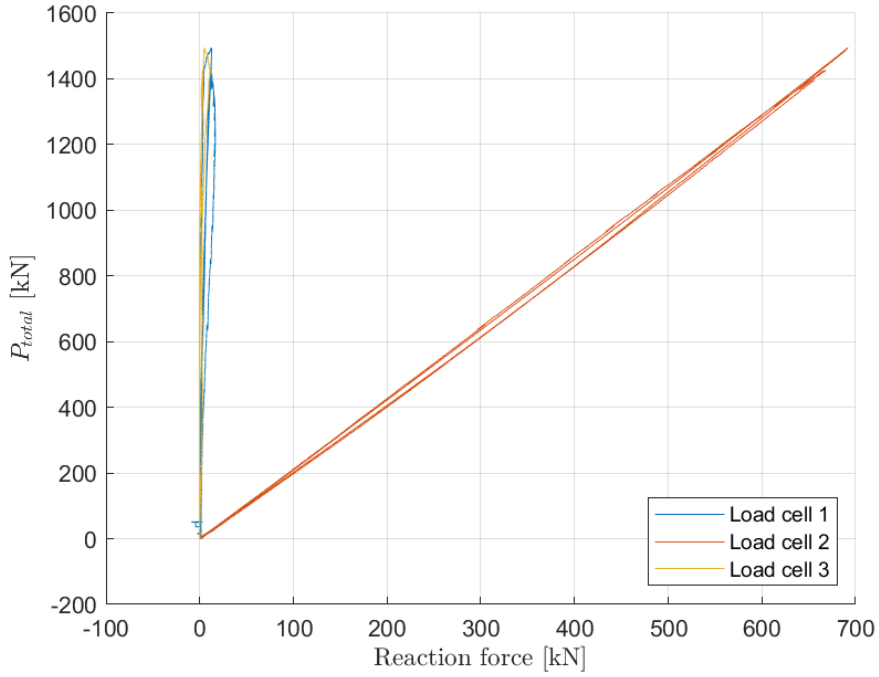

Fig. 3.35 - LB3 - Reaction force from load cells versus total load for load cell 1-3, west side

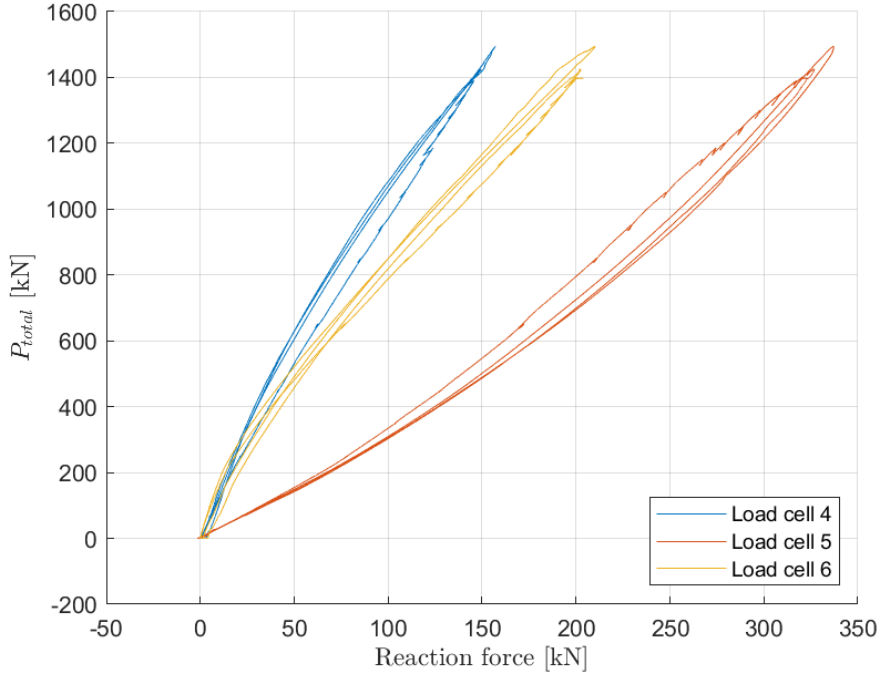

Fig. 3.36 - LB3 - Reaction force from load cells versus total load for load cell 4-6, east side

On the transverse displacements of the beams, it was observed that Beam 3 (northern beam) experienced a bigger transverse displacement relative to the middle than Beam 1 (southern beam). This can be seen on the measurements of LVDTs 5 and 6 (LVDTs 7-10 showed a similar behavior), see Fig. 3.37.

Regarding the vertical displacement, on a section located under the load it can be seen, Fig. 3.38 , that beam 3 had a slightly bigger displacement than beam 1, and that the biggest displacement was under the beam 3.

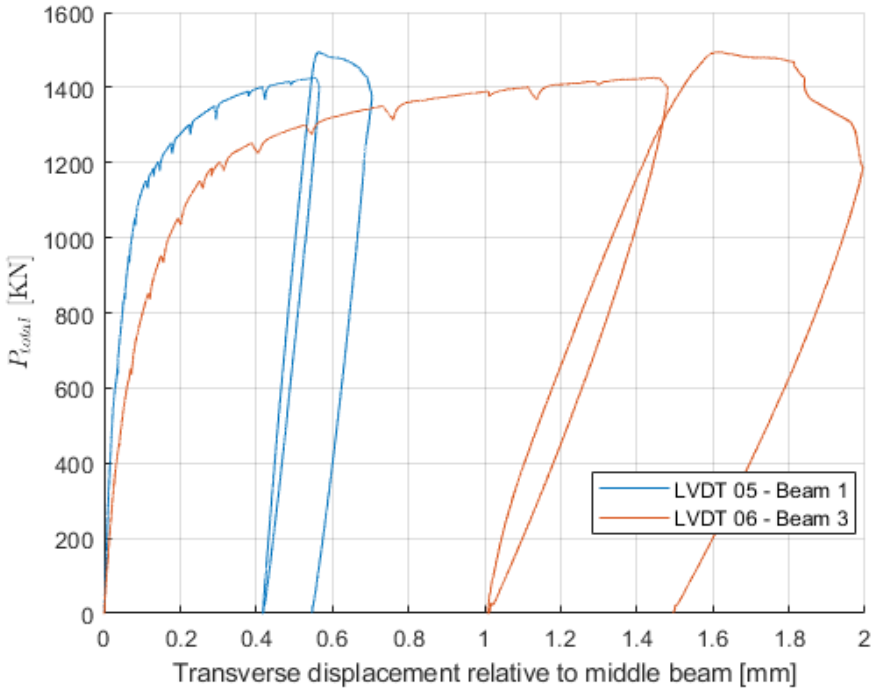

Fig. 3.37 - LB3 - Relative transverse displacements from the outer beams measured from the bottom flange.

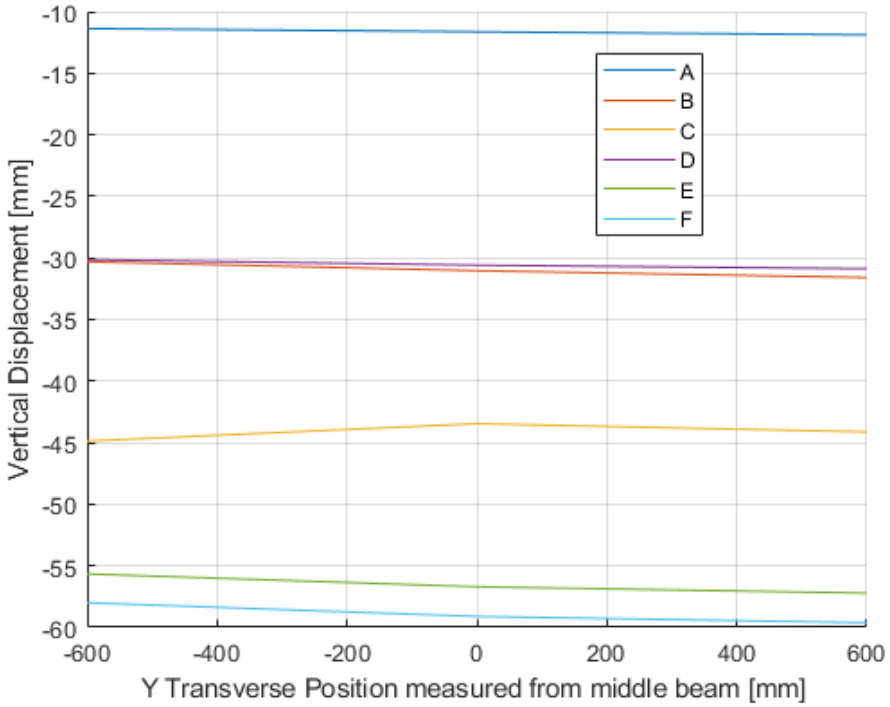

Fig. 3.38 - LB3 - Vertical displacement transverse distribution between the three steel beams for different load stages (A-F). Measurements from Lasers 4, 5 and 6.

Other results from the test for load cells, optic fibers, lasers, LVDTs, 2D DIC and 3D DIC are respectively shown at Annex G to L.

4. CONCLUSION

4.1. SPECIMEN LB1

The main observed phenomena during the test of specimen LB1 are summarized in the following.

- First cracking occurred at a load level of $P_{total,cracking} = 850\ kN$, flexural vertical cracks occurred at mid-span.
- First yielding of the steel beams was observed at a load level of $P_{total,1st\ yielding} = 1447\ kN$.
- The maximum load level was $P_{total,max} = 1746\ kN$
- The load distribution showed that the middle beam carried a higher portion of the load compared to the outer beams.
- Beam 1 experienced a sudden growth of the transverse displacement before failure.
- The steel beams yielded on an approximated length of 2 m, located on the central part of the beams.
- Flexural cracks stopped at the level of the top flange of the steel beams. Moreover, a longitudinal crack on the bottom surface of concrete, specifically on the corner of the trapezoidal shape, propagated through the complete length of the specimen.
- After yielding of the beams, a sudden loss of the capacity was experienced due to failure of the interface between steel beam 1 and the adjacent concrete.
- The interface failure propagated to the supports, where the beams detached from the adjacent concrete in addition to wide cracks.
- The failure mode of the specimen was bending due to yielding of the steel beams, followed by a reduction of the ductility of the element due to interface failure.

4.2. SPECIMEN LB3

The main observed phenomena during the test of specimen LB3 are summarized in the following.

- First cracking occurred at a load level of $P_{total,cracking} = 650\ kN$, flexural vertical cracks occurred at mid-span.
- First yielding of the steel beams was observed at a load level of $P_{total,1st\ yielding} = 1267\ kN$.
- The maximum load level was $P_{total,max} = 1494\ kN$
- The load distribution showed that the middle beam carried a higher portion of the load compared to the outer beams.
- The interface between the bottom flange of the steel beams and the adjacent concrete was only activated on a small region near the load application point.
- No interface failure was observed.
- Transverse displacements of the outer beams relative to the middle beams were measured but displacement remained small compared to specimen LB1.
- Horizontal cracks were also observed at mid-span on the top layer of concrete, showing initiation of crushing.
- The failure mode of the specimen was bending with concrete crushing on the top layer.

5. REFERENCES

Brongers, I. B. (2021). *Meetresultaten trekproven LB2 staal brug 70.* Delft: TNO.

Faassen, L. (2021). *FBG optical fibers in proof loading of concrete slab bridges.* Delft, Building 23, 2628 CN, Stevinweg 1 The Netherlands: Technische Universiteit Delft, Concrete structures.

Rasker, D. P. (2020). *MP0016 resultaten druksterkte Brug 70 1-6.* Delft: TNO.

A. LOAD CELLS- LB1

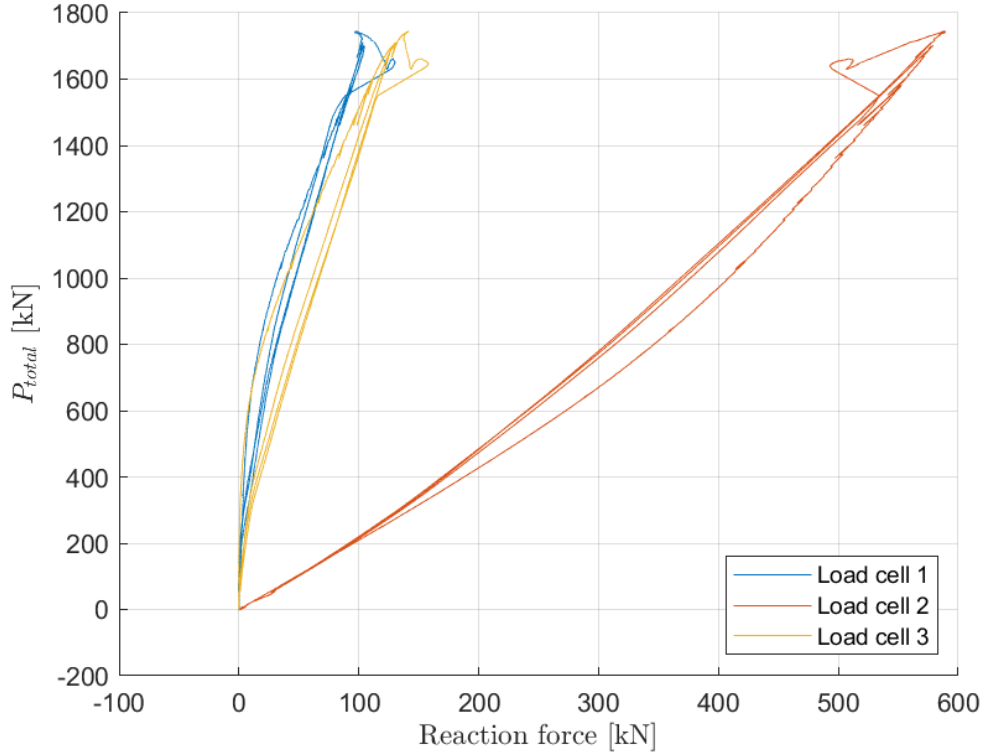

Fig A.1. LB1. Reaction force from load cells versus total load for load cell 1-3.

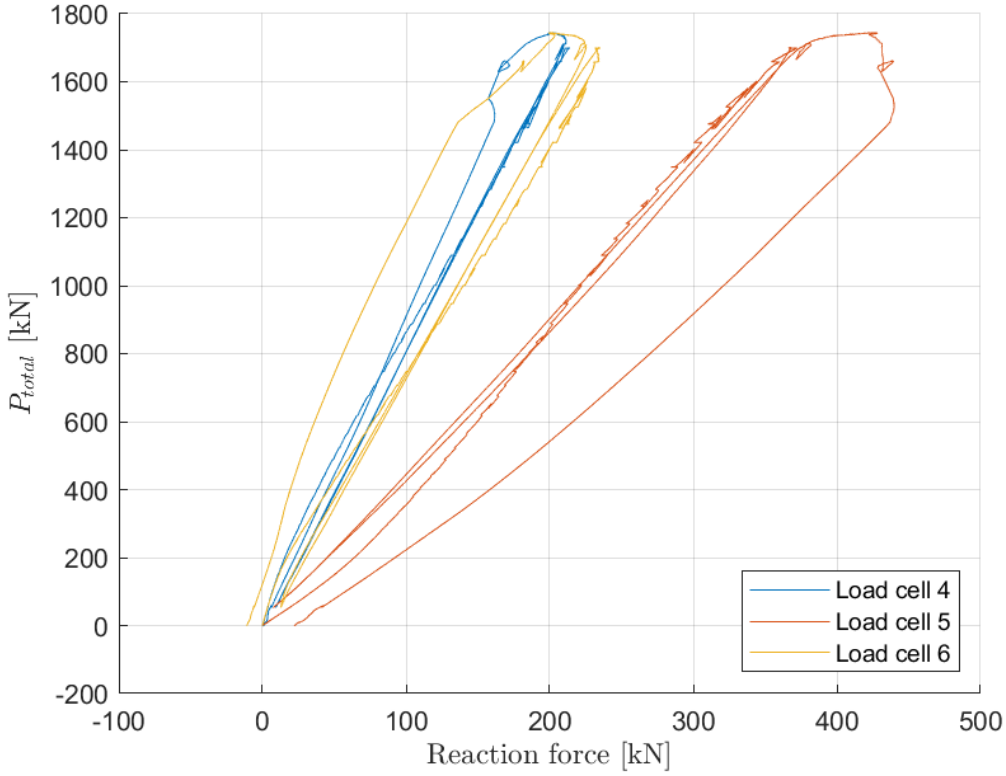

Fig A.2. LB1. Reaction force from load cells versus total load for load cell 1-3.

B. OPTIC FIBERS - LB1

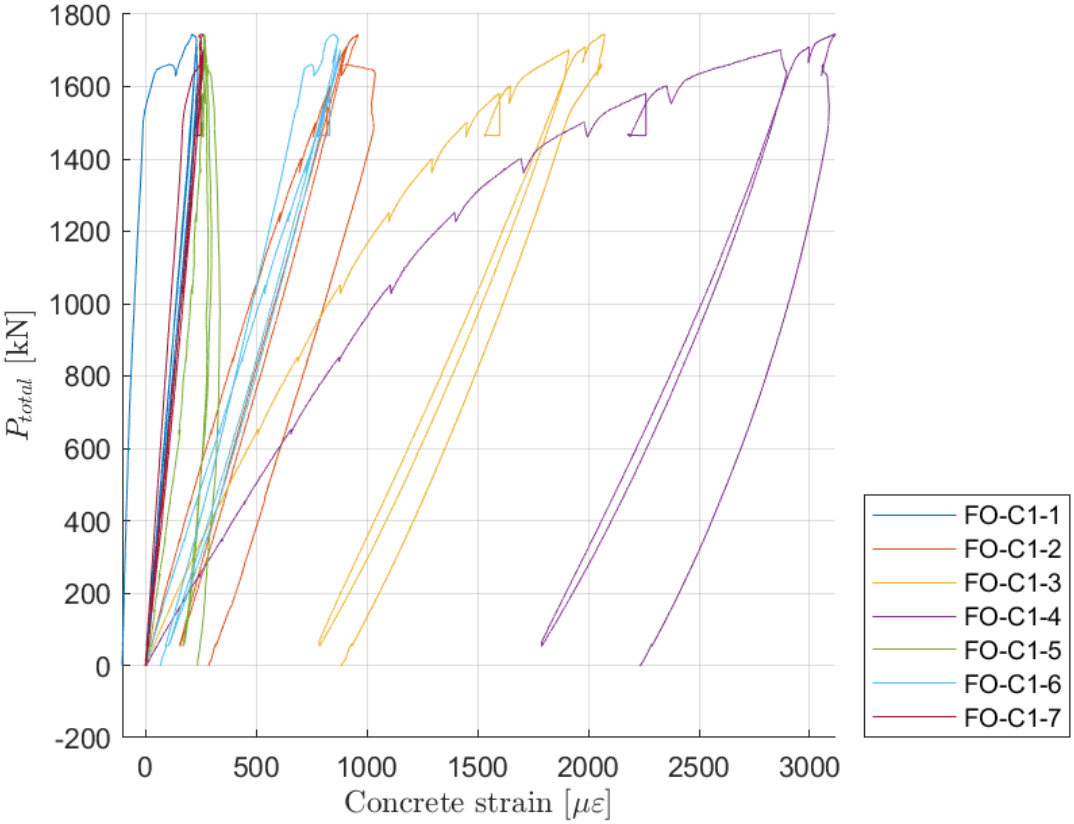

Fig B.1. LB1. Concrete strain versus total load for FO-C1-1 to FO-C1-7 at beam 1.

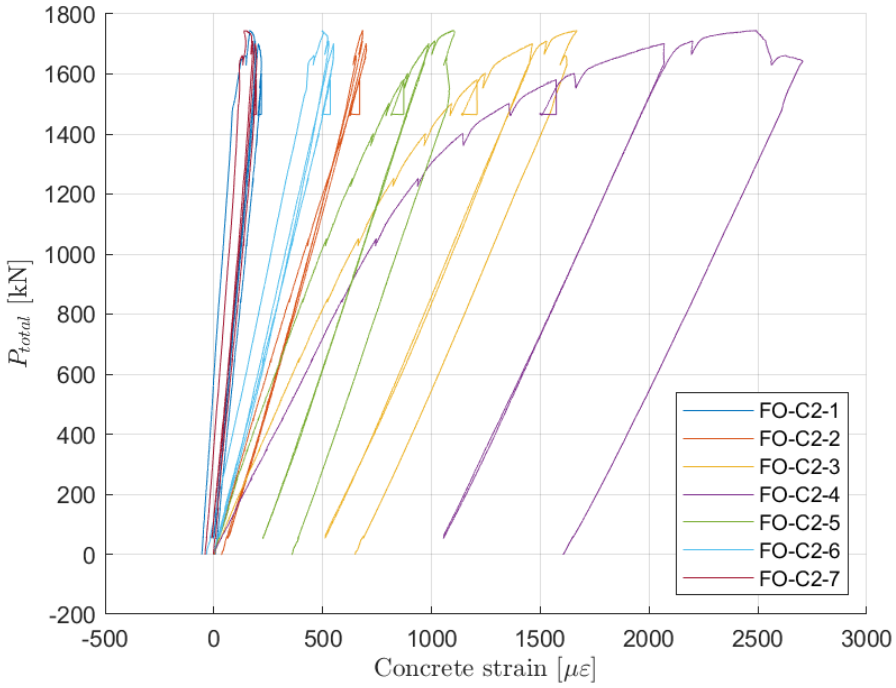

Fig B.2. LB1. Concrete strain versus total load for FO-C2-1 to FO-C2-7 at beam 2.

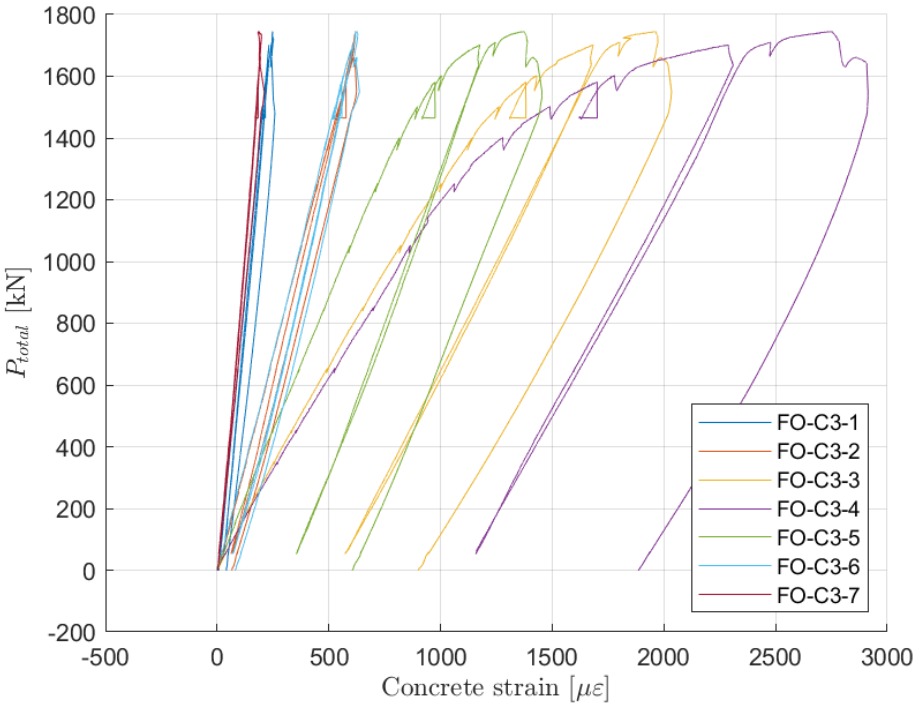

Fig B.3. LB1. Concrete strain versus total load for FO-C3-1 to FO-C3-7 at beam 3.

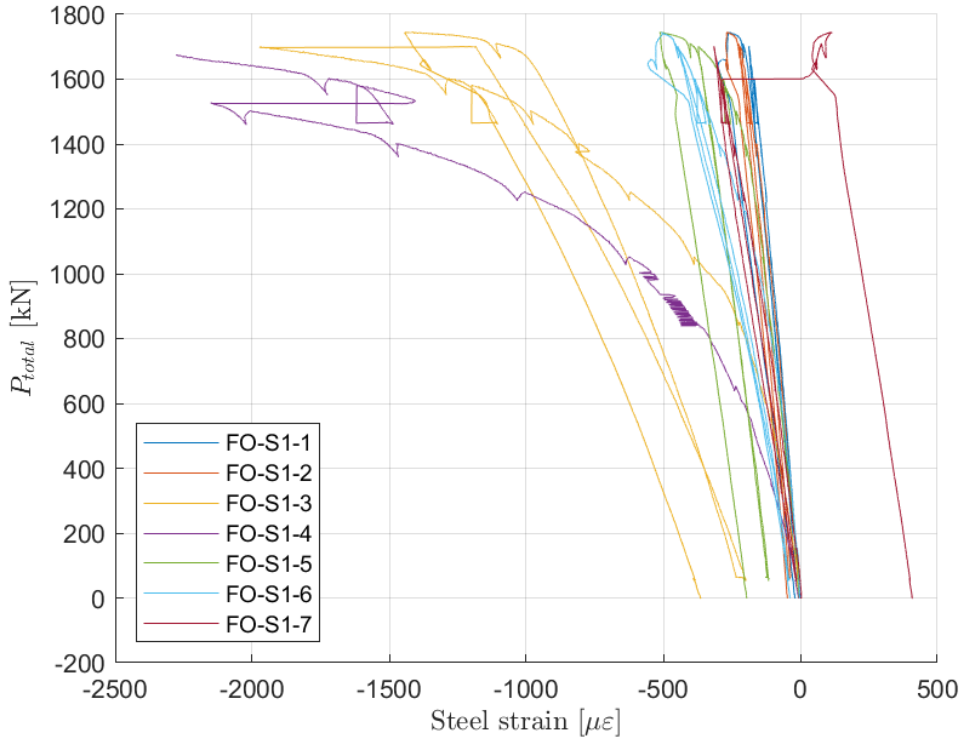

Fig B.4. LB1. Steel strain versus total load for FO-S1-1 to FO-S1-7 at beam 1. FO-S1-4 has been linearized around 800 kN because it fell out of range.

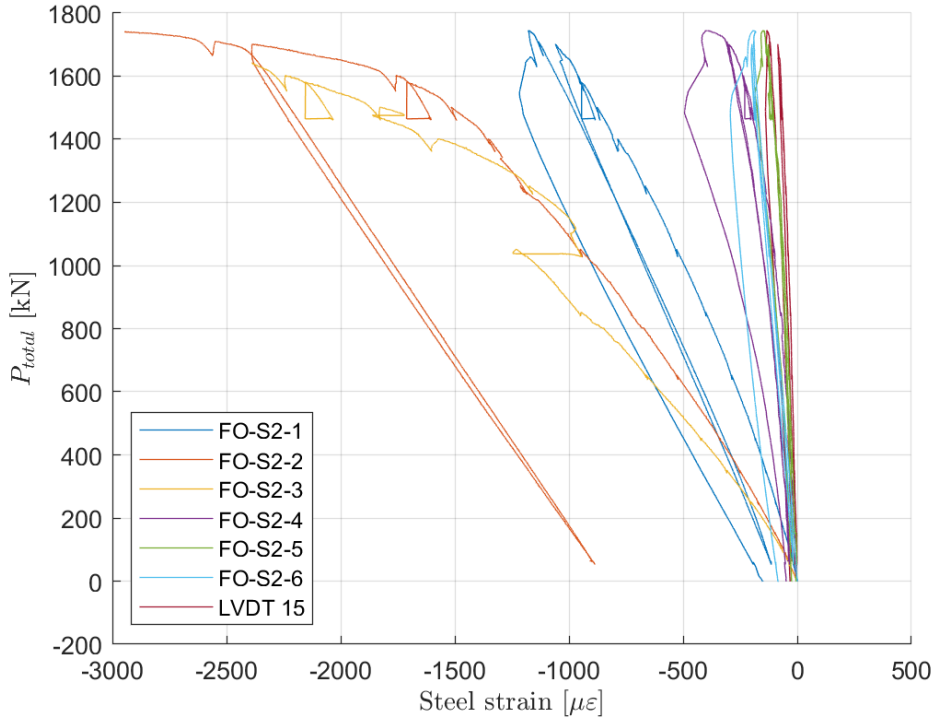

Fig B.5. LB1. Steel strain versus total load for FO-S2-1 to FO-S2-6 and LVDT 15 at beam 2. FO-S2-7 broke during preparation of LB1 and was replaced by LVDT 15. FO-S2-3 and FO-S2-4 fell out of range during testing, so the measurement stopped when they reached their maximum strain.

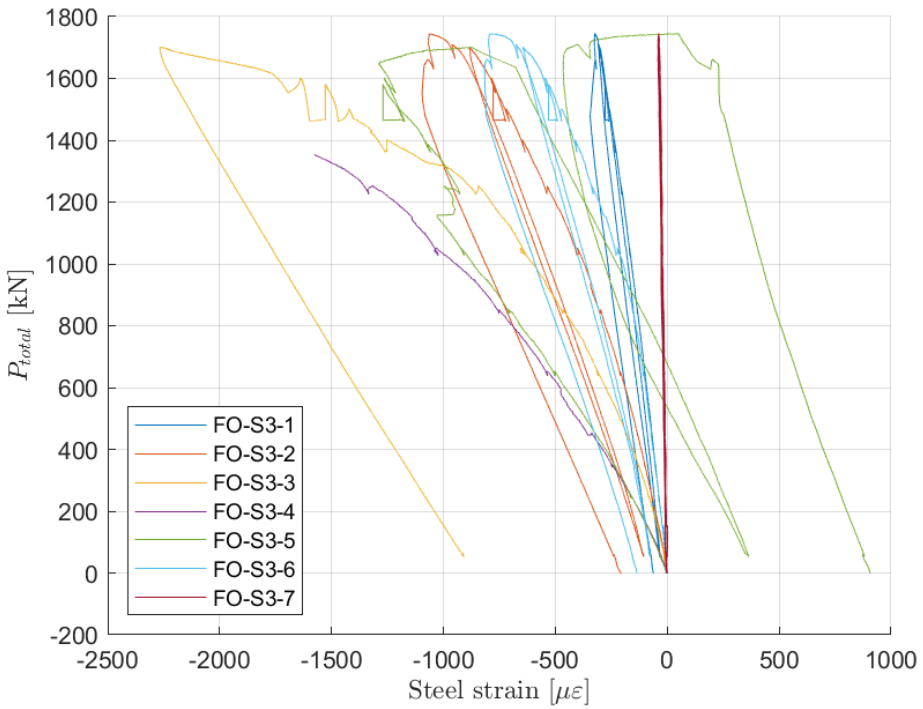

Fig B.6. LB1. Steel strain versus total load for FO-S3-1 to FO-S3-7. FO-S3-3 has been linearized and stopped where it reaches its maximum strain. FO-S3-4 fell out of range for a long time and the results from where it fell out of range have been removed.

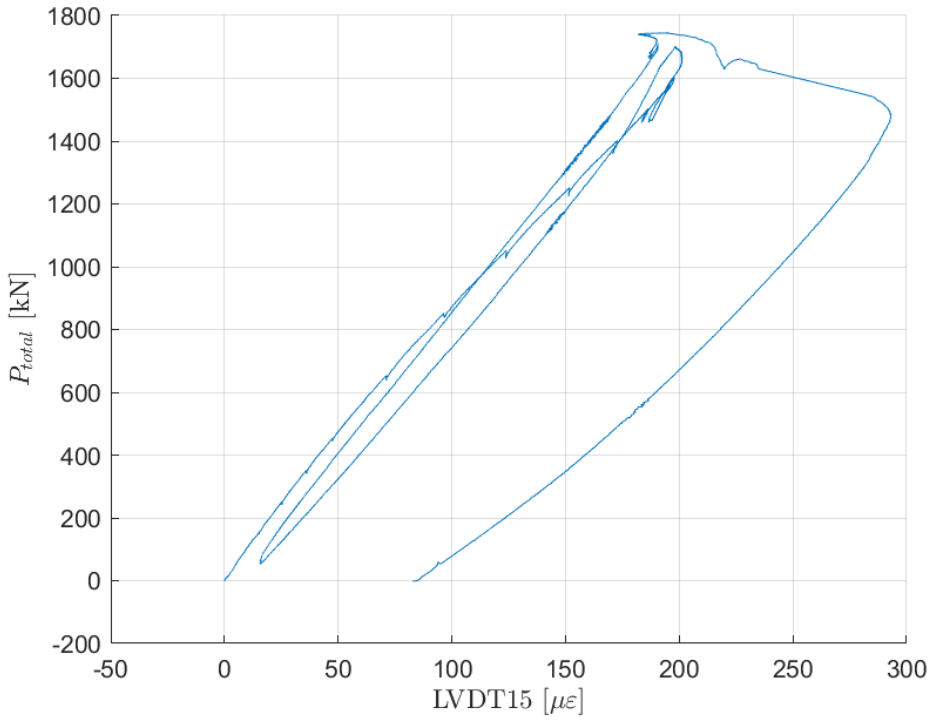

Fig B.7. LB1. Strain versus load for LVDT 15, that is replacing FO-S2-7.

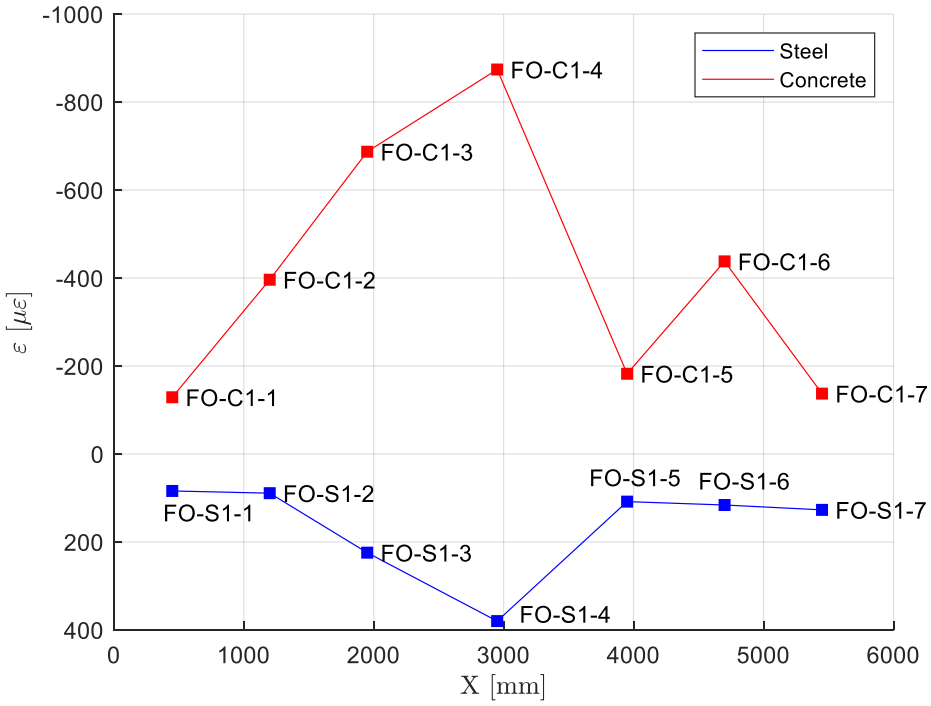

Fig B.8. LB1. Point A - Cracking starts (Ptotal=850 kN). X, the position of the optic fibers from the support, versus the strain measured for optic fibers above and below beam 1.

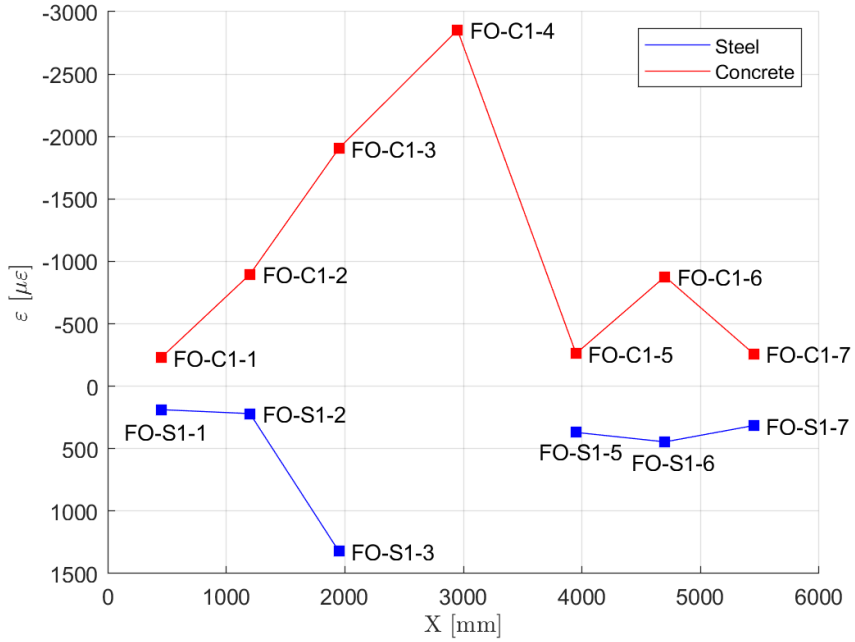

Fig B.9. LB1. Point C - Maximum load before the specimen was unloaded to relax the optic fibers (Ptotal=1700 kN). X, the position of the optic fibers from the support, versus the strain measured for optic fibers above and below beam 1. FO-S1-4 fell out of range.

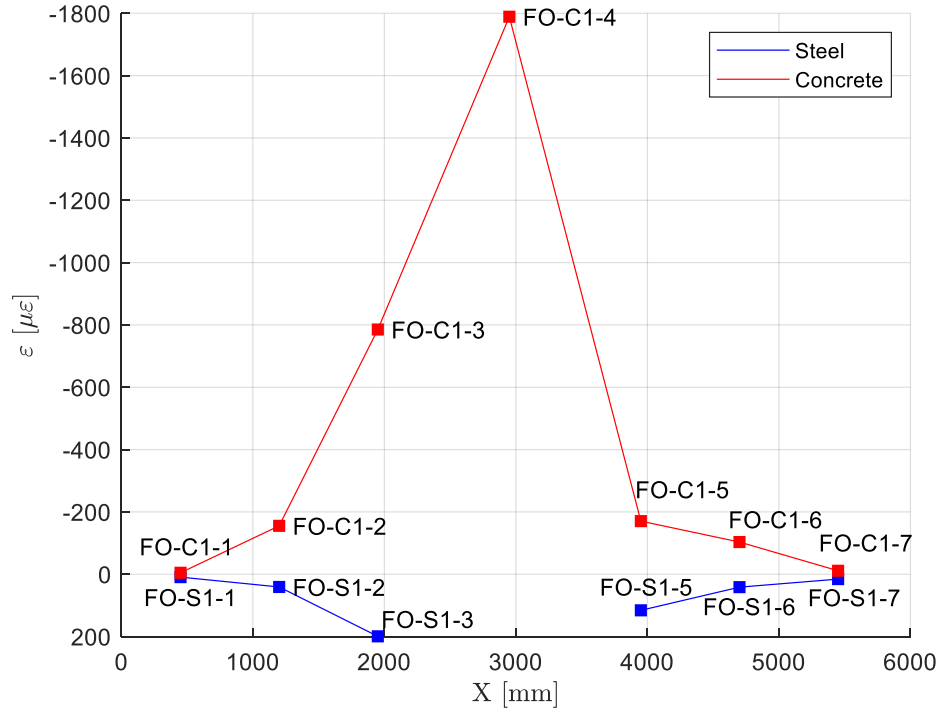

Fig B.10. LB1. Point D - Unloading to relax optic fibers before reloading (Ptotal=50 kN). X, the position of the optic fibers from the support, versus the strain measured for optic fibers above and below beam 1. FO-S1-4 fell out of range.

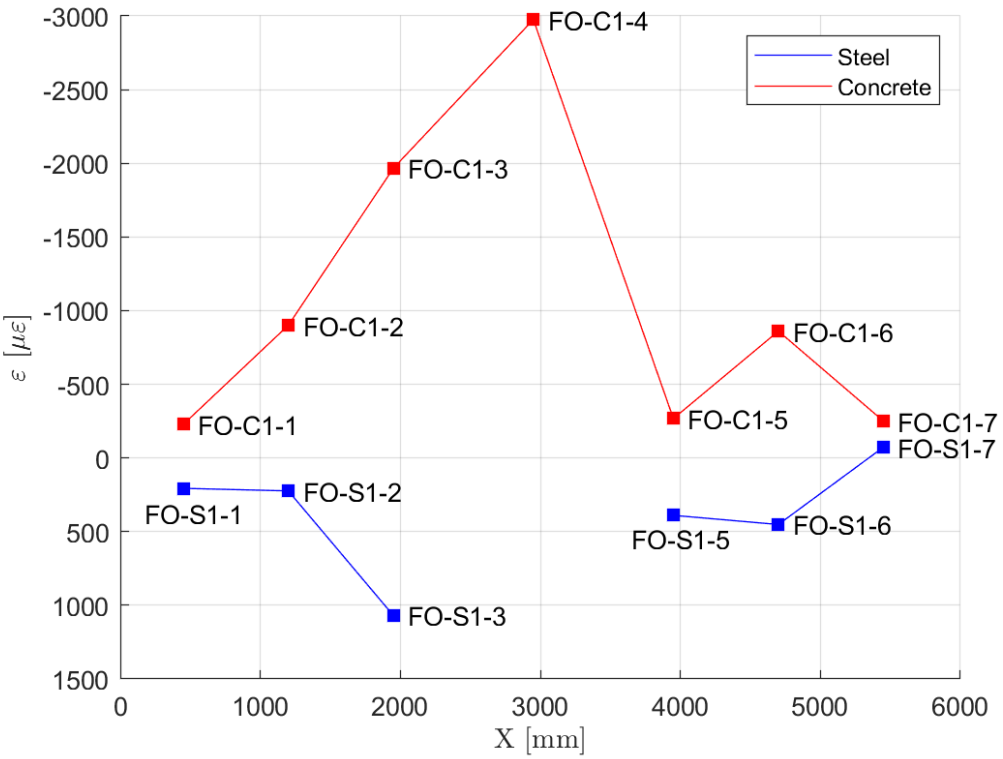

Fig B.11. LB1. Point E - Second loading reaches same load as the max load of first loading (Ptotal=1700 kN). X, the position of the optic fibers from the support, versus the strain measured for optic fibers above and below beam 1. FO-S1-4 fell out of range.

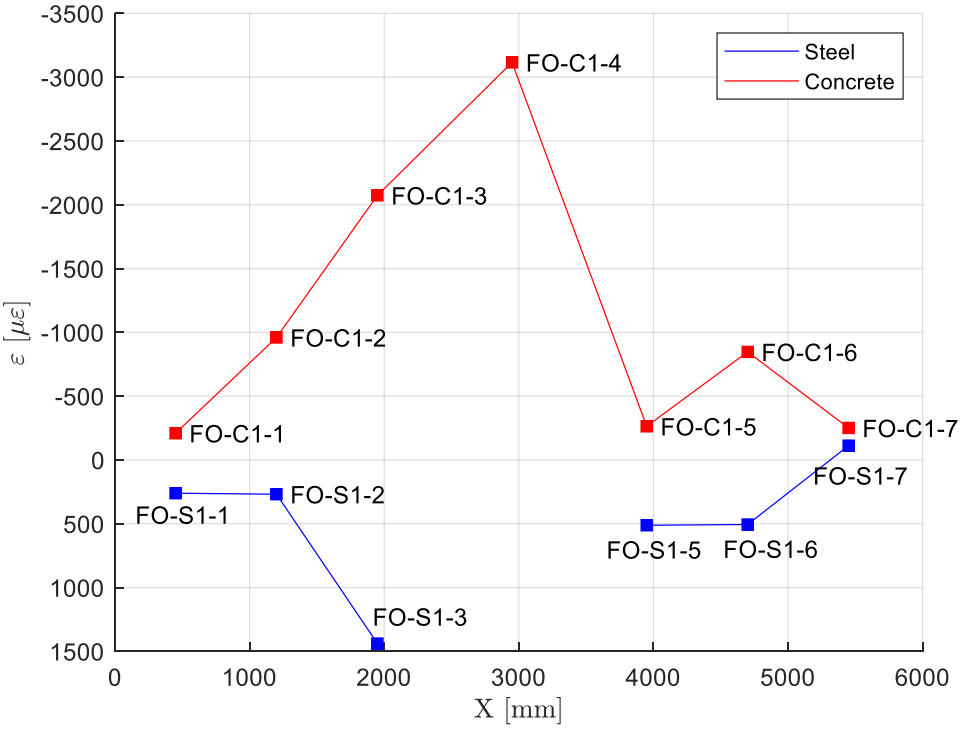

Fig B.12. LB1. Point F - Max load is reached load (Ptotal=1746 kN). X, the position of the optic fibers from the support, versus the strain measured for optic fibers above and below beam 1. FO-S1-4 fell out of range.

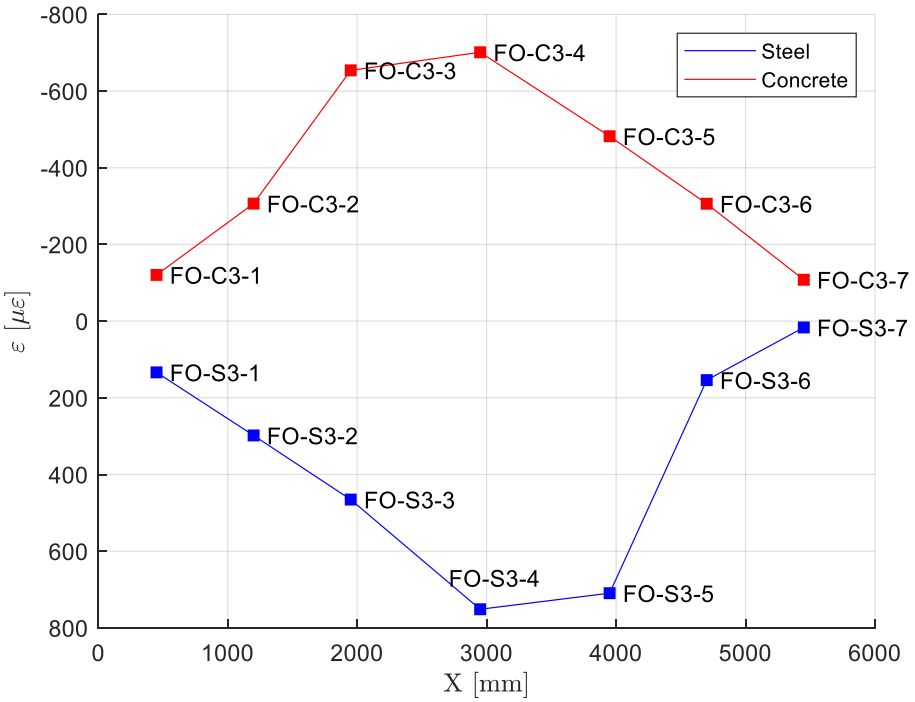

Fig B.13. LB1. Point A - cracking starts (Ptotal=850 kN). X, the position of the optic fibers from the support, versus the strain measured for optic fibers above and below beam 1.

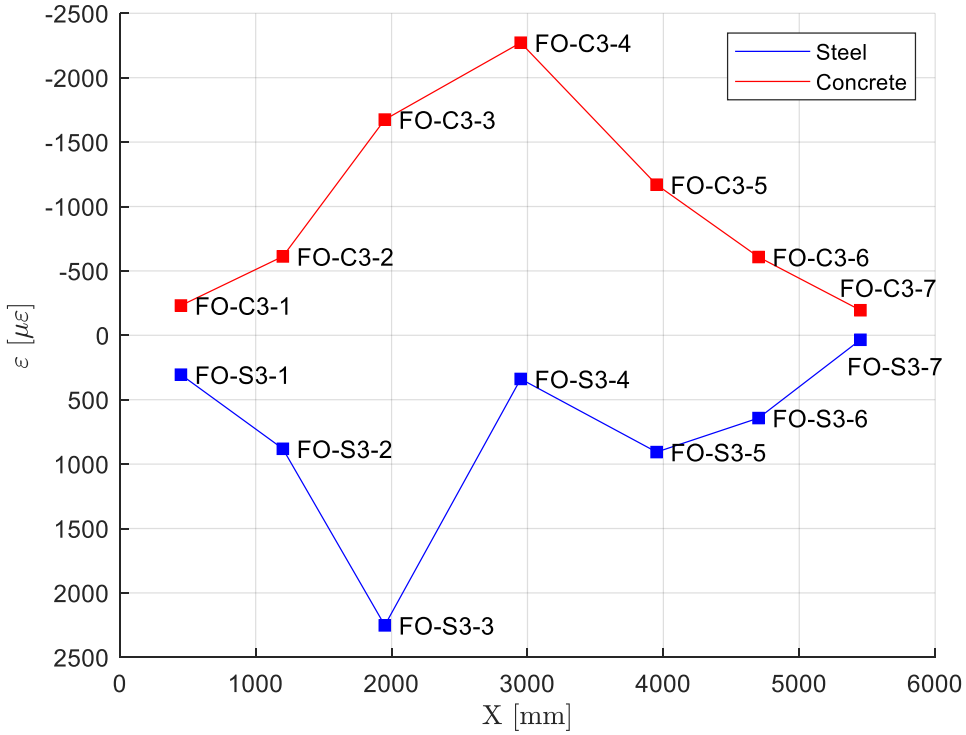

Fig B.14. LB1. Point C - Maximum load before the specimen was unloaded to relax the optic fibers (Ptotal=1700 kN). X, the position of the optic fibers from the support, versus the strain measured for optic fibers above and below beam 3. Results from FO-S3-4 may not be valid at this loading point.

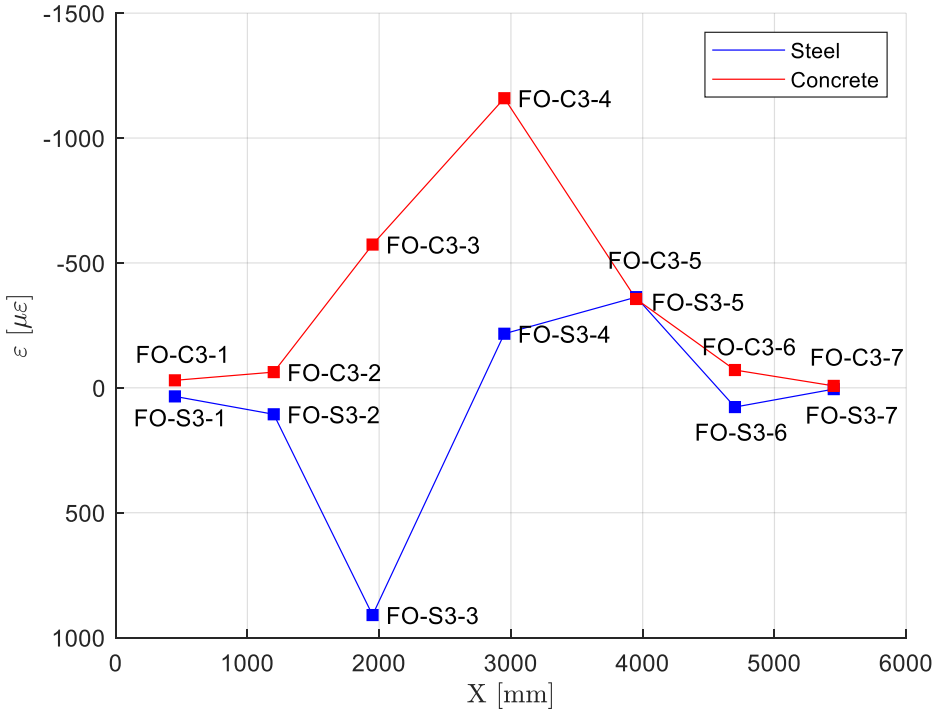

Fig B.15. LB1. Point D - Unloading to relax the optic fibers before reloading (Ptotal=50 kN). X, the position of the optic fibers from the support, versus the strain measured for optic fibers above and below beam 3. Results from FO-S3-4 and FO-S3-5 may not be valid.

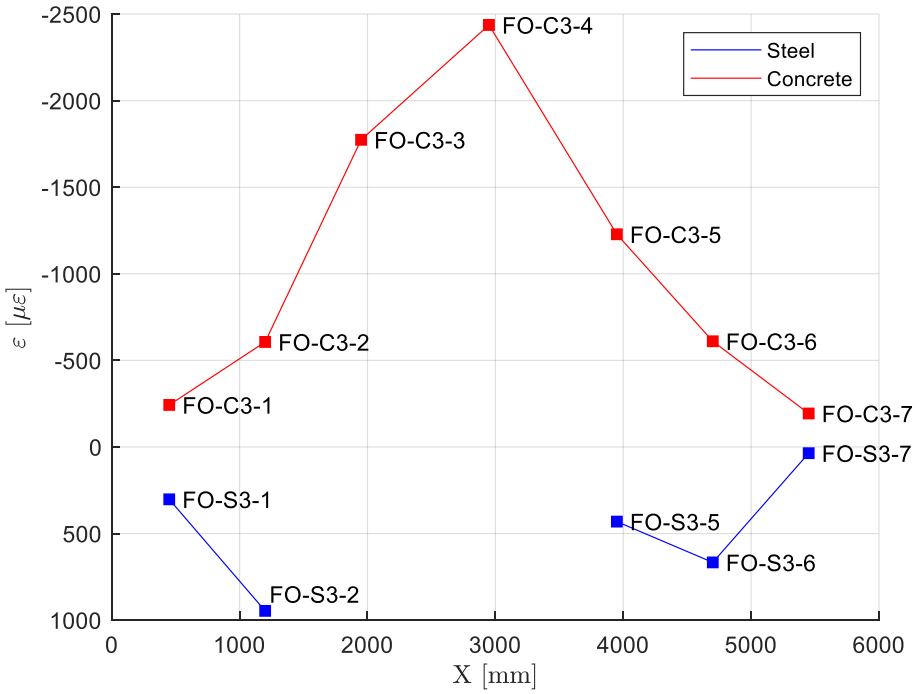

Fig B.16. LB1. Point E - Second loading reaches same load as the max load of first loading (Ptotal=1700 kN). X, the position of the optic fibers from the support, versus the strain measured for optic fibers above and below beam 3. FO-S3-4 fell out of range.

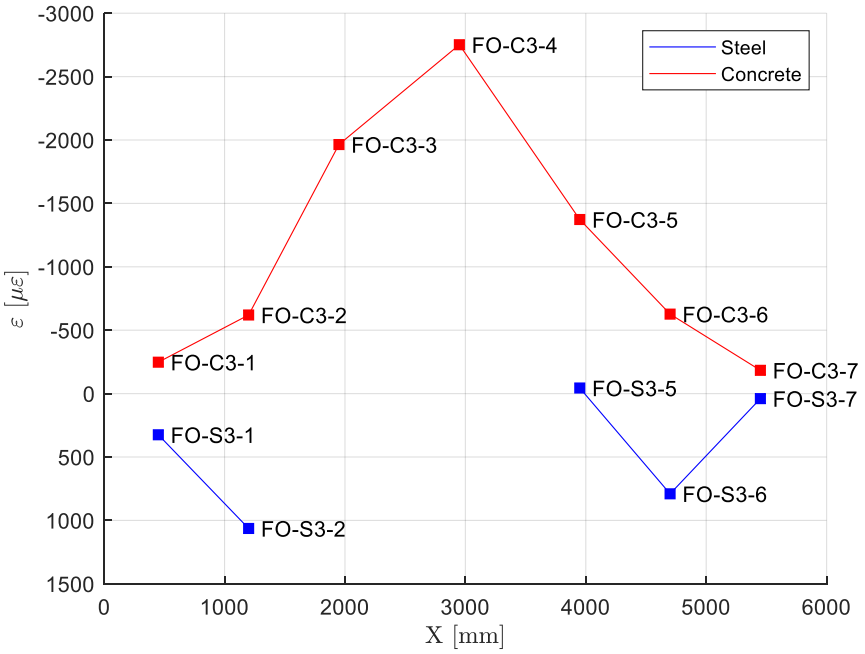

Fig B.17. LB1. Point F - Max load is reached load (Ptotal=1746 kN). X, the position of the optic fibers from the support, versus the strain measured for optic fibers above and below beam 3. FO-S3-4 fell out of range. Results from FO-S3-5 may not be valid.

C. LASERS - LB1

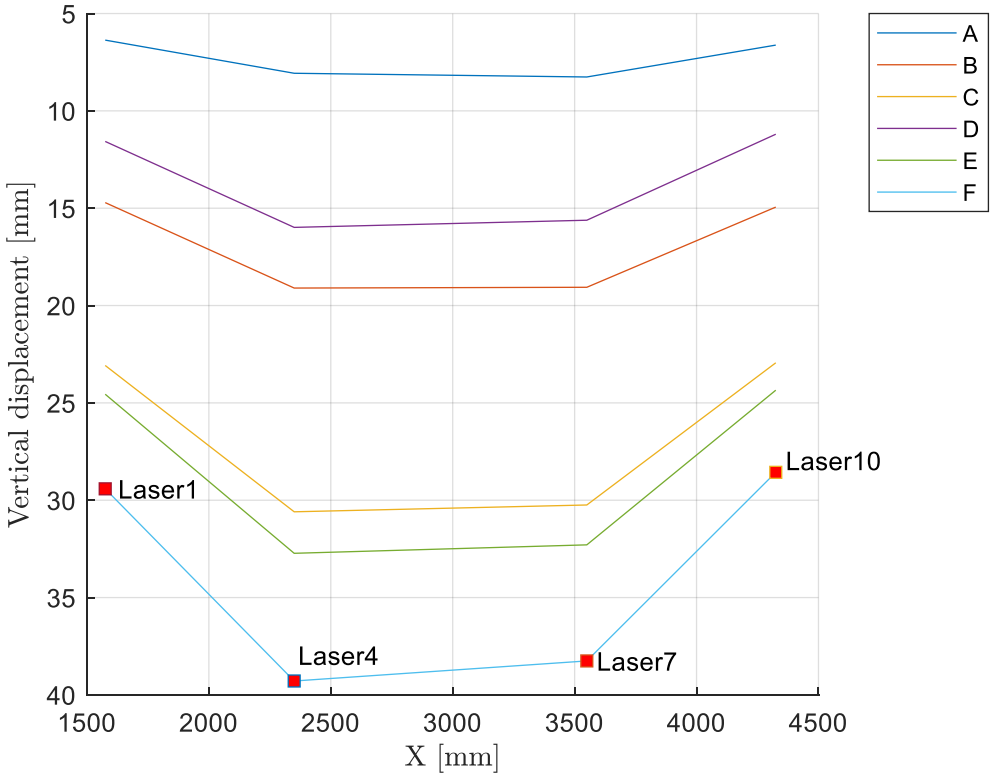

Fig C.1. LB1. Laser 1, 4, 7 and 10 positioned at beam 1. X, distance to support, versus vertical displacement for point A-F.

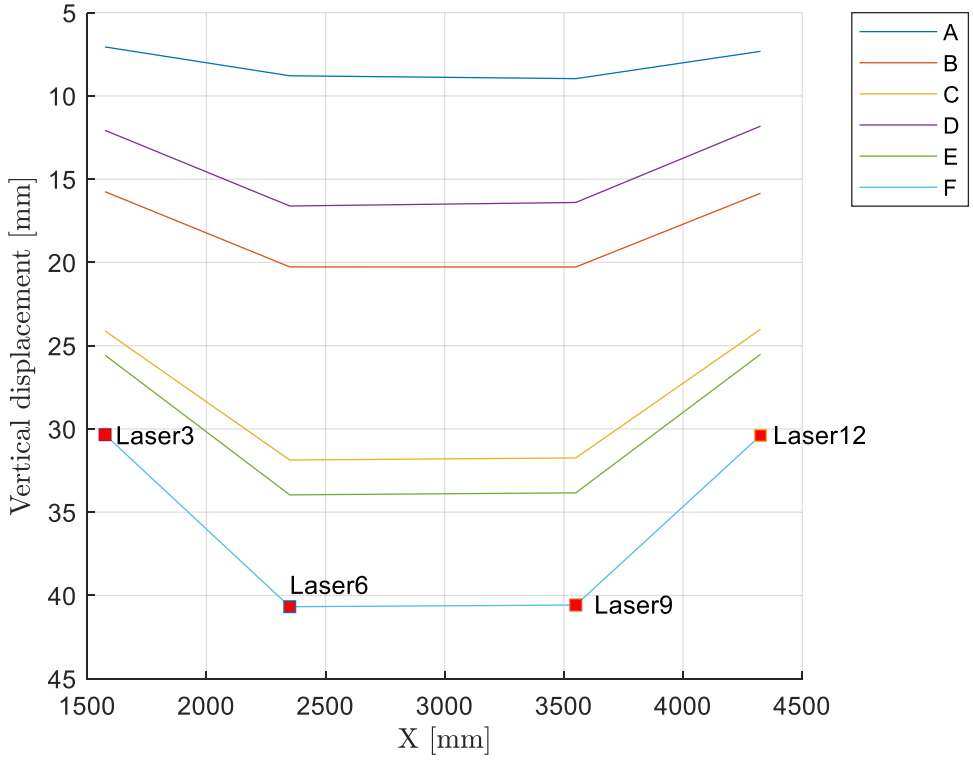

Fig C.2. LB1. Laser 3, 6, 9 and 12 positioned at beam 3. X, distance to support, versus vertical displacement for point A-F.

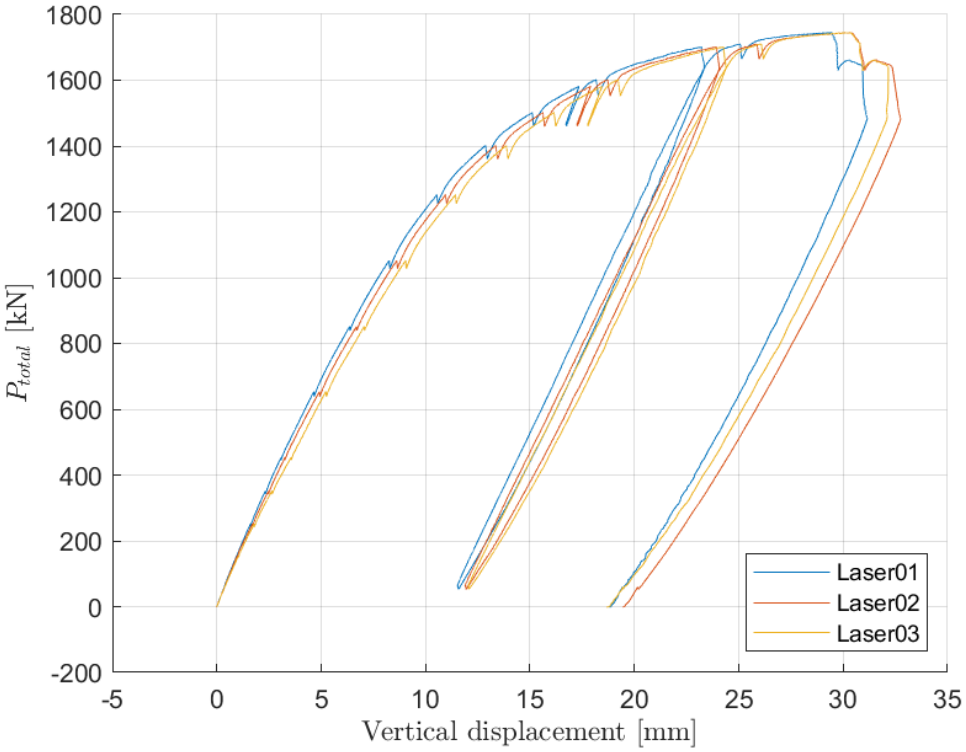

Fig C.3. LB1. Total vertical displacement versus total load for laser 1-3.

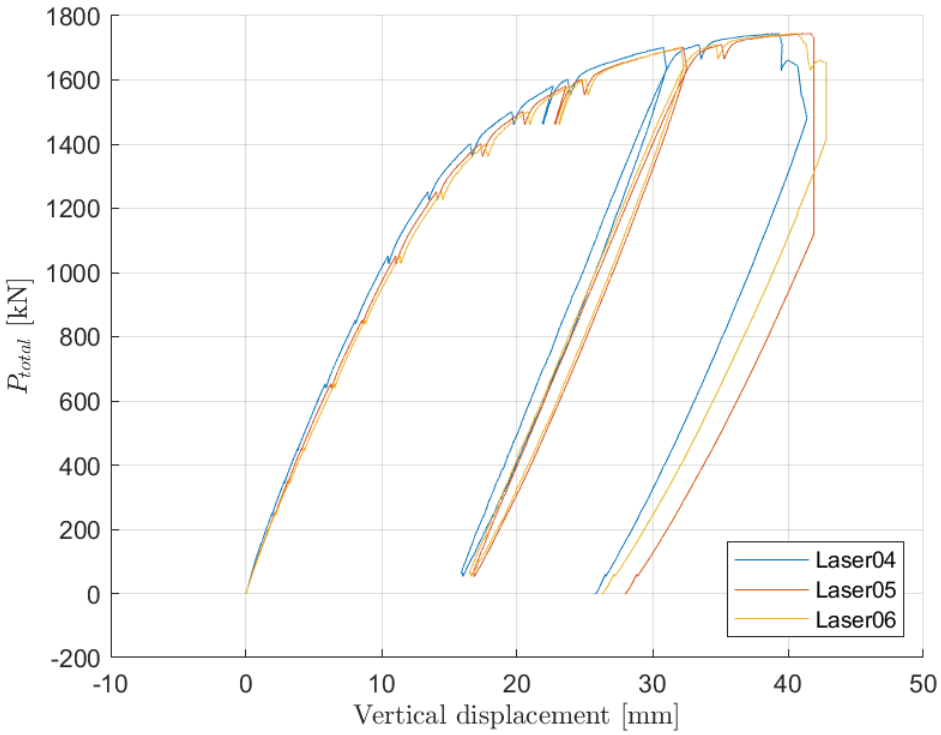

Fig C.4. LB1. Total vertical displacement versus total load for lasers 4-6.

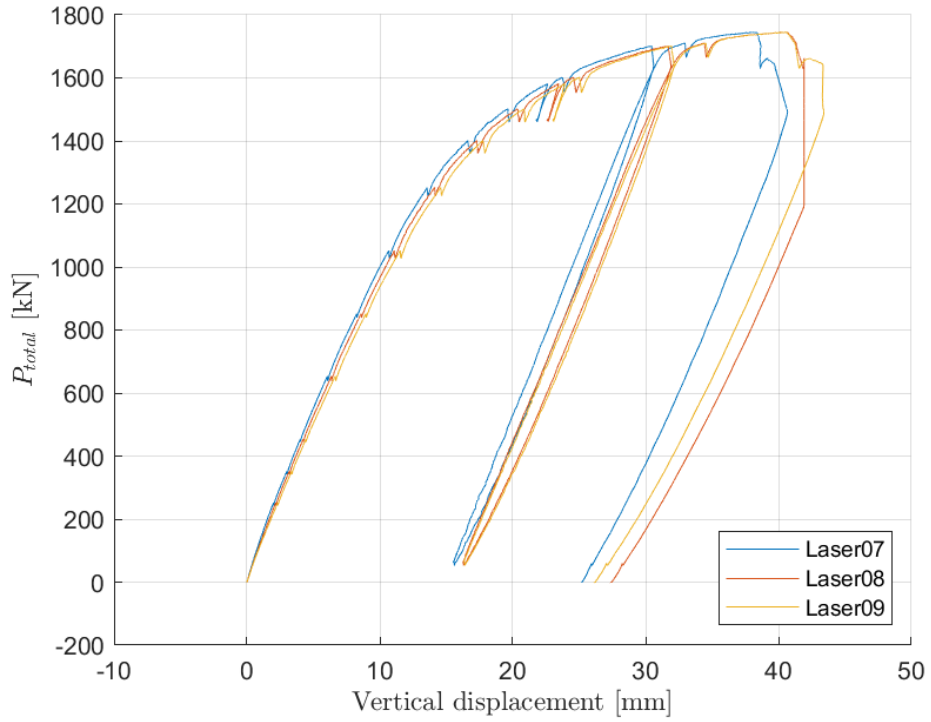

Fig C.5. LB1. Total vertical displacement versus total load for laser 7-9.

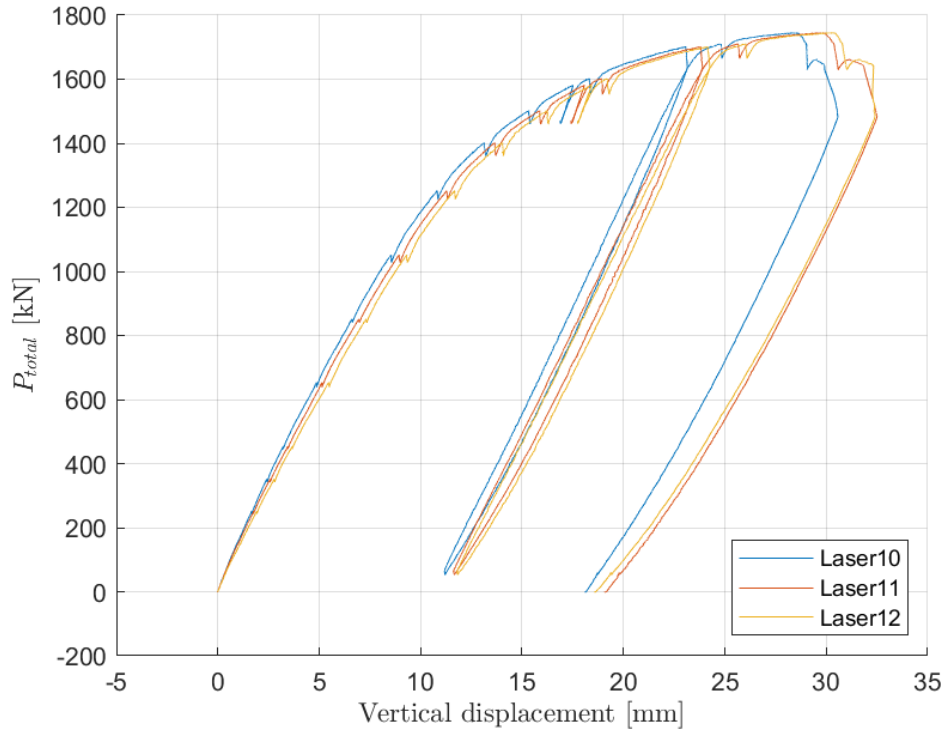

Fig C.6. LB1. Total vertical displacement versus total load for laser 10-12.

D. LVDTS - LB1

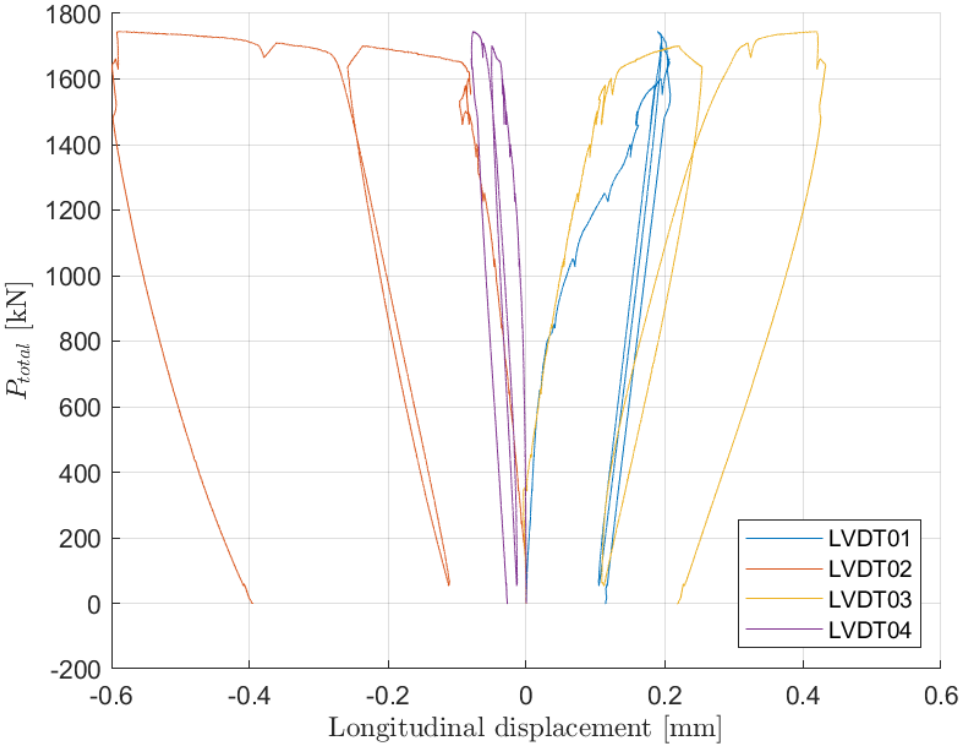

Fig D.1. LB1. Relative longitudinal displacement between steel and concrete versus total load for LVDT 1-4.

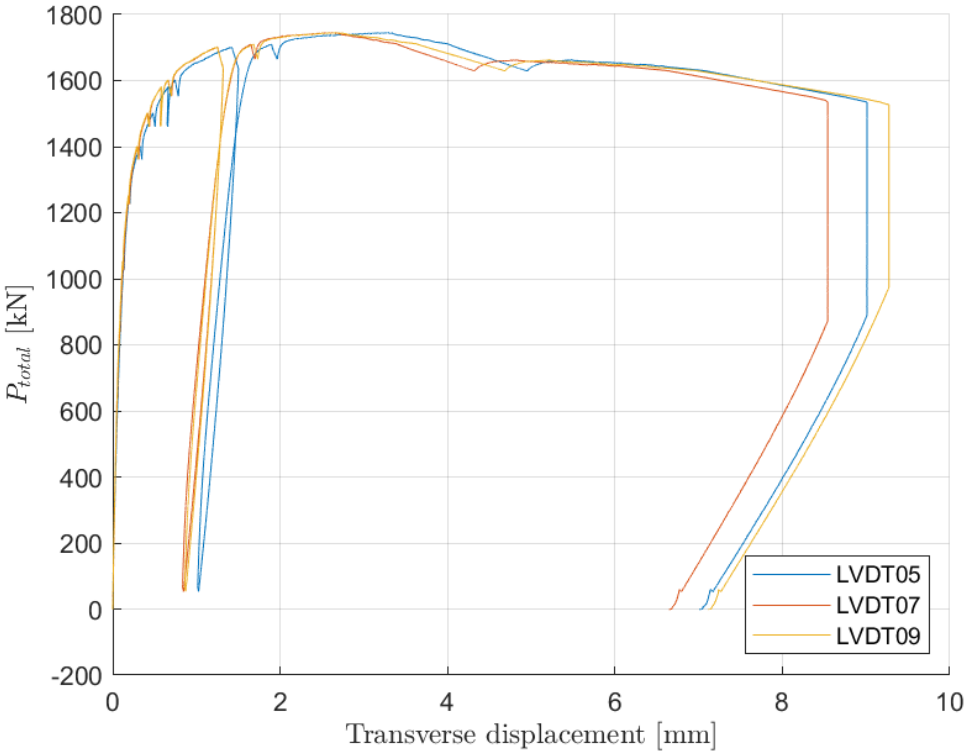

Fig D.2. LB1. Relative transverse displacement between beam 1 and 2 versus total load for LVDT 5, 7 and 9.

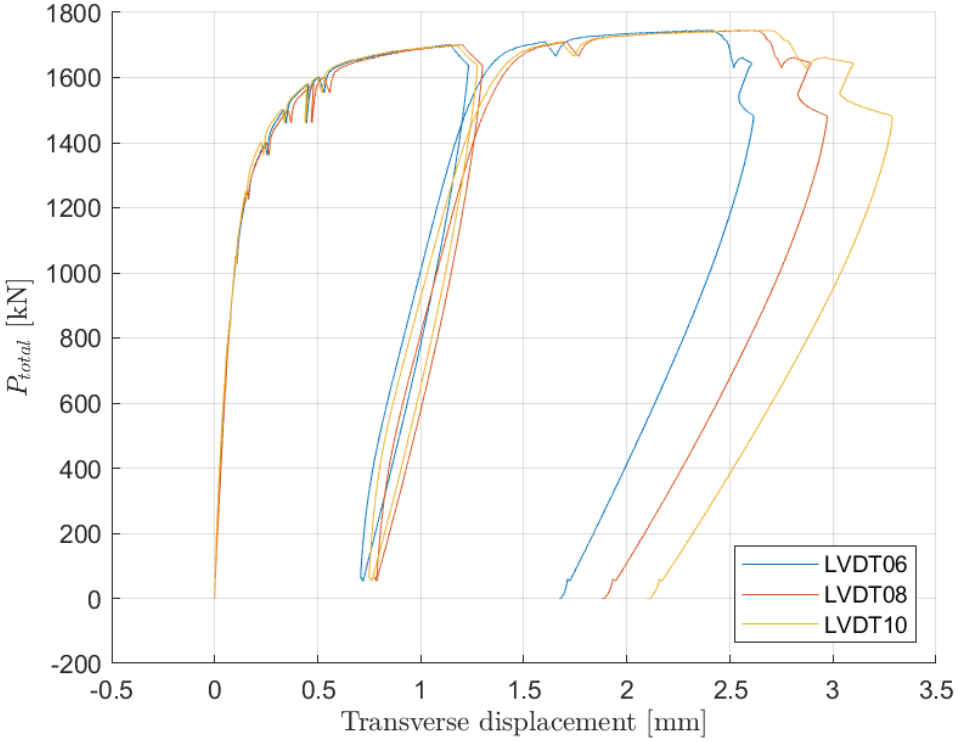

Fig D.3. LB1. Relative transverse displacement between beam 1 and 2 versus total load for LVDT 6, 8 and 10.

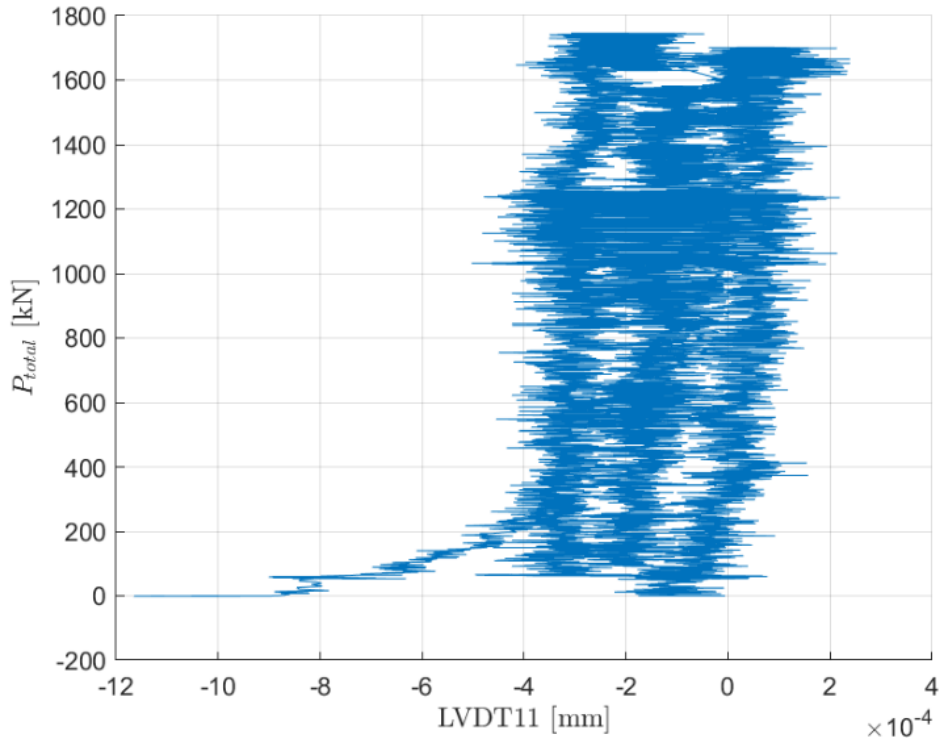

Fig D.4. LB1. Relative longitudinal displacement of concrete and bottom flange at beam 2 versus total load.

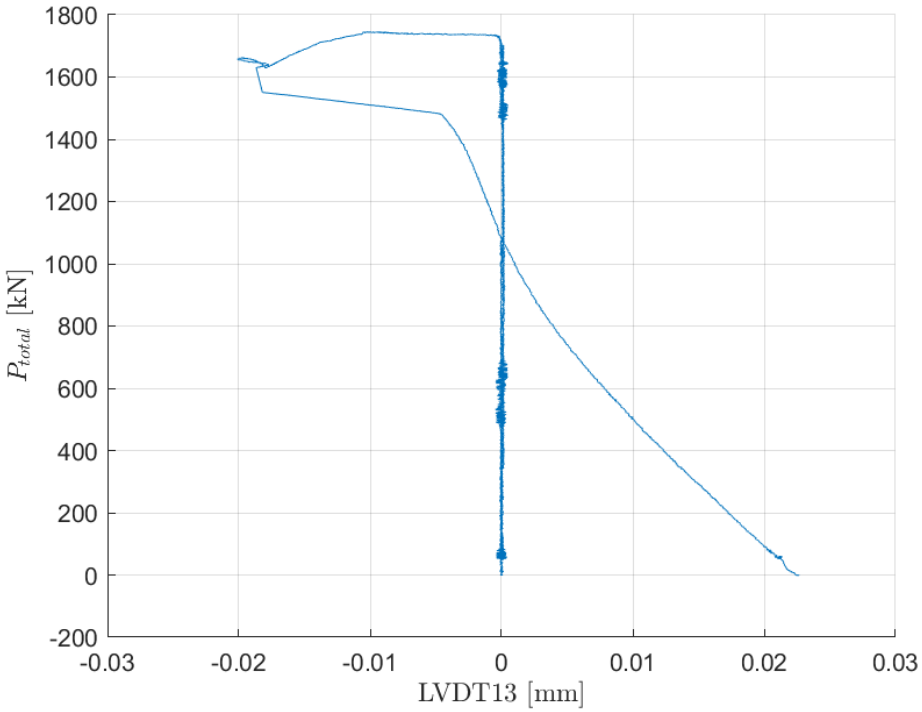

Fig D.5. LB1. Relative longitudinal displacement of concrete and bottom flange at beam 1 versus total load.

E. 2D DIC - LB1

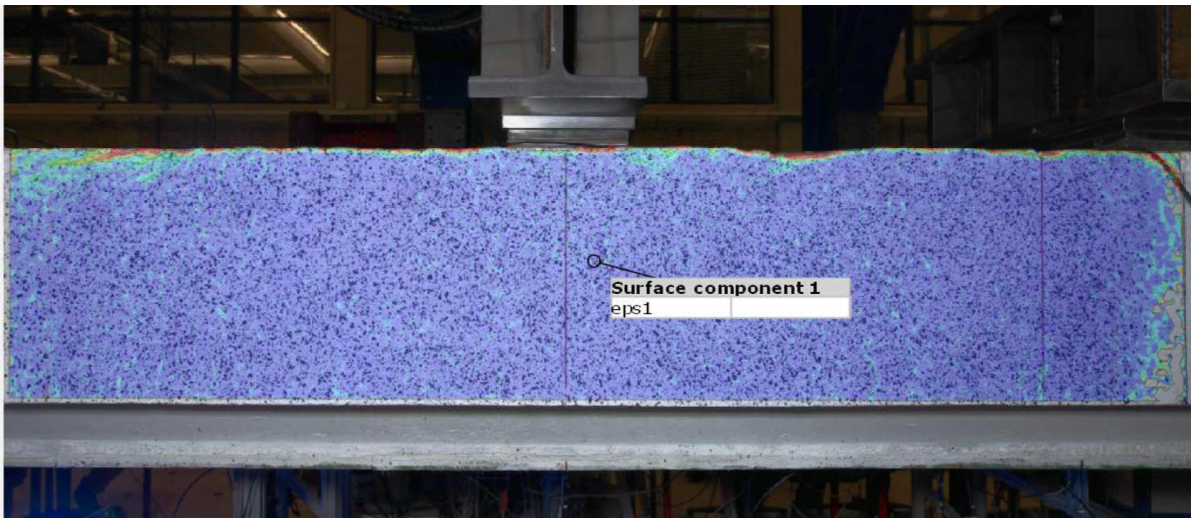

Fig E.1. LB1. Principal Strain Field ε1. 2D DIC at 350 kN.

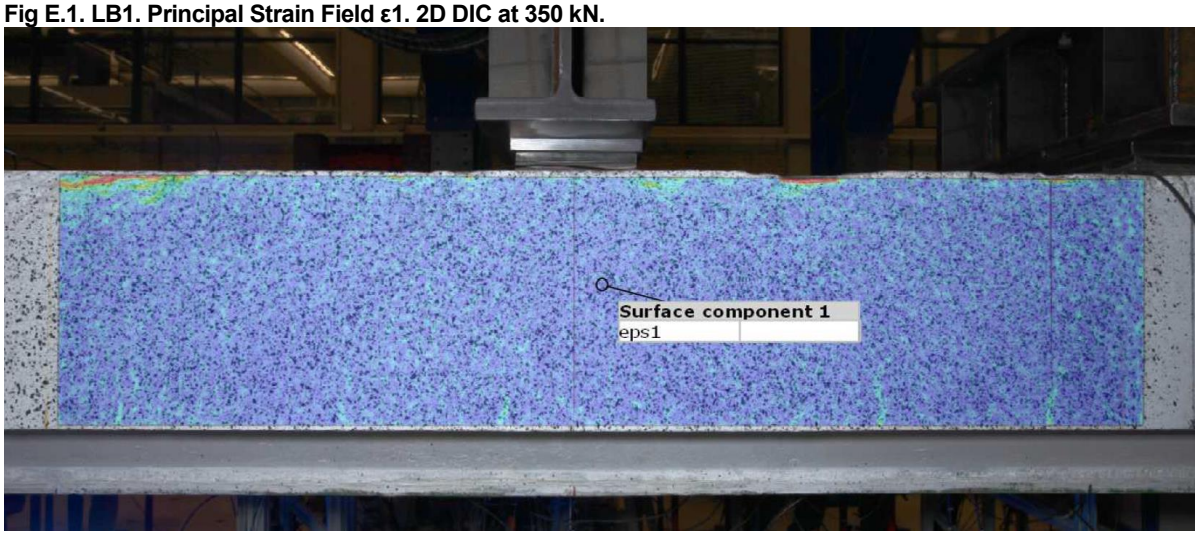

Fig E.2. LB1. Principal Strain Field ε1 2D DIC at 450 kN.

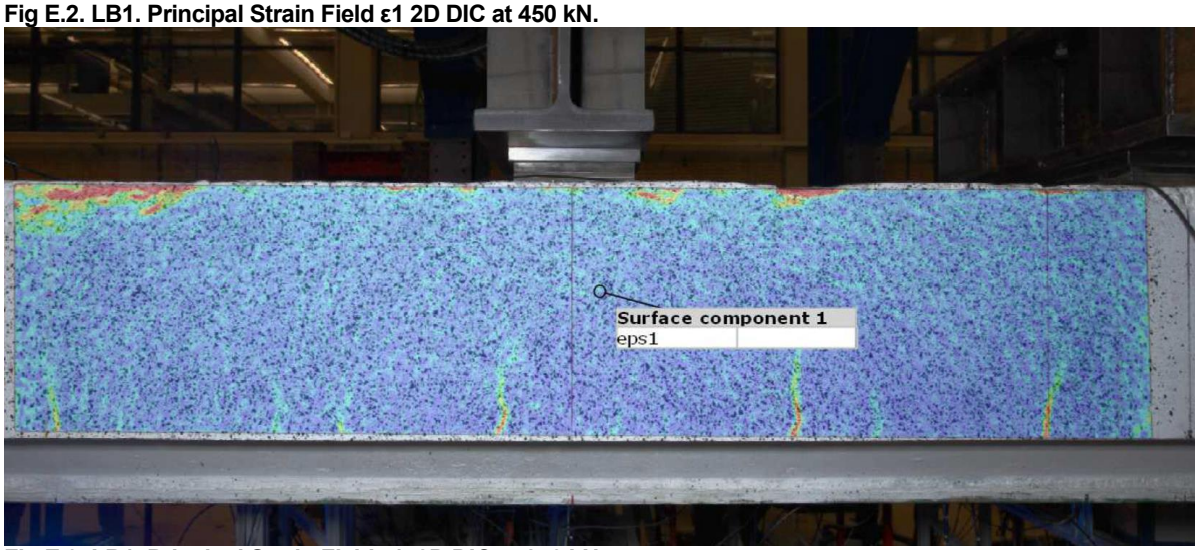

Fig E.3. LB1. Principal Strain Field ε1. 2D DIC at 850 kN.

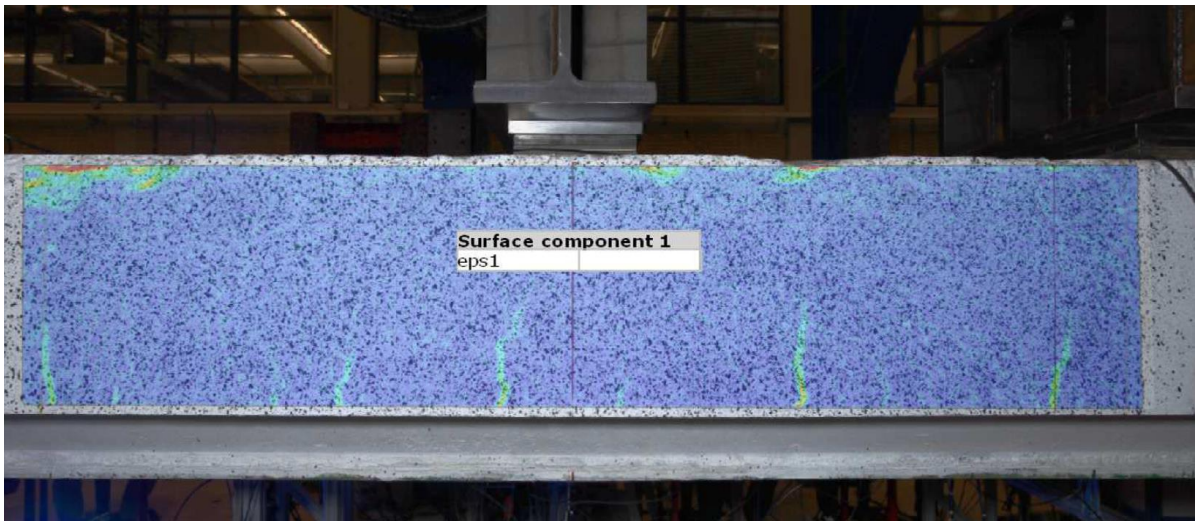

Fig E.4. LB1. Principal Strain Field ε1. 2D DIC at 1050 kN.

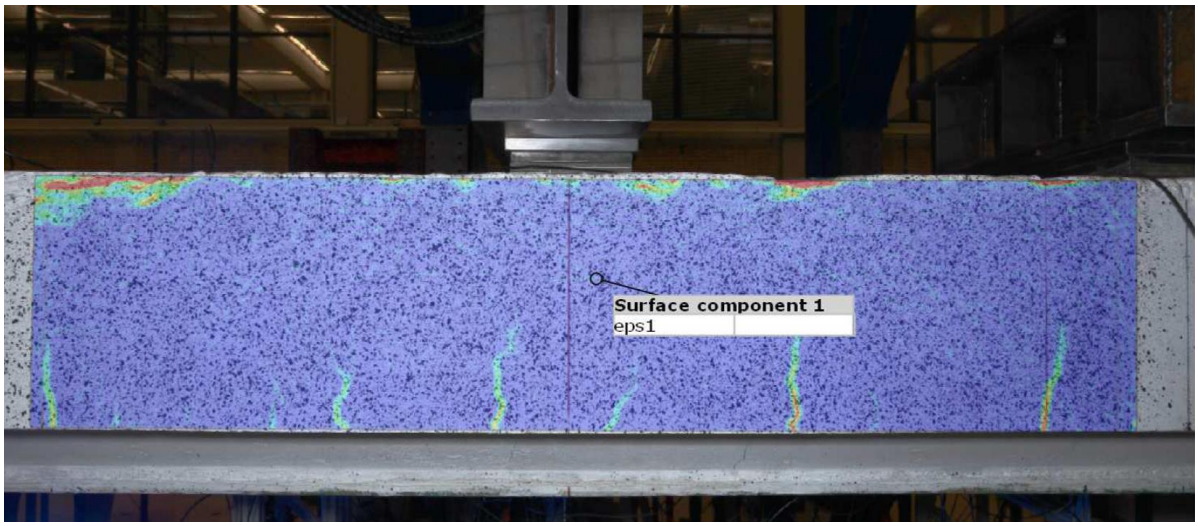

Fig E.5. LB1. Principal Strain Field ε1. 2D DIC at 1250 kN.

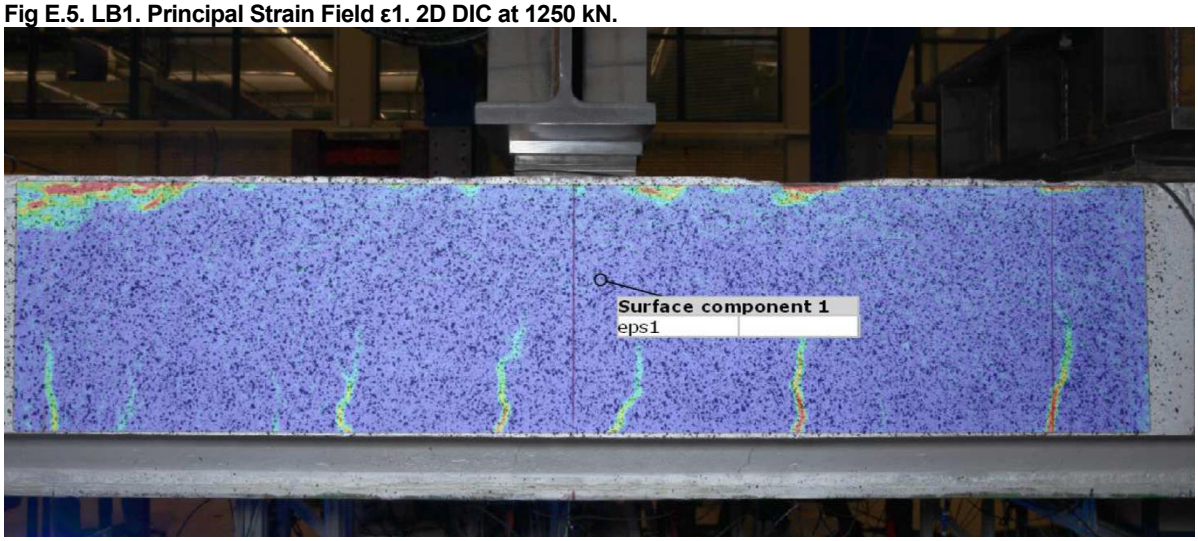

Fig E.6. LB1. Principal Strain Field ε1. 2D DIC at 1400 kN.

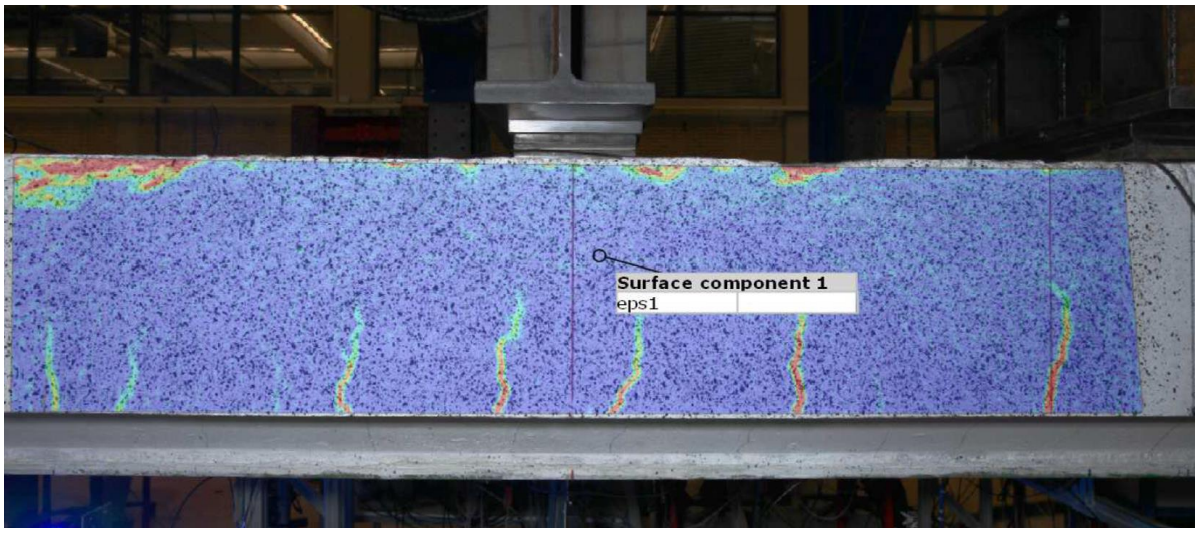

Fig E.7. LB1. Principal Strain Field ε1. 2D DIC at 1460 kN.

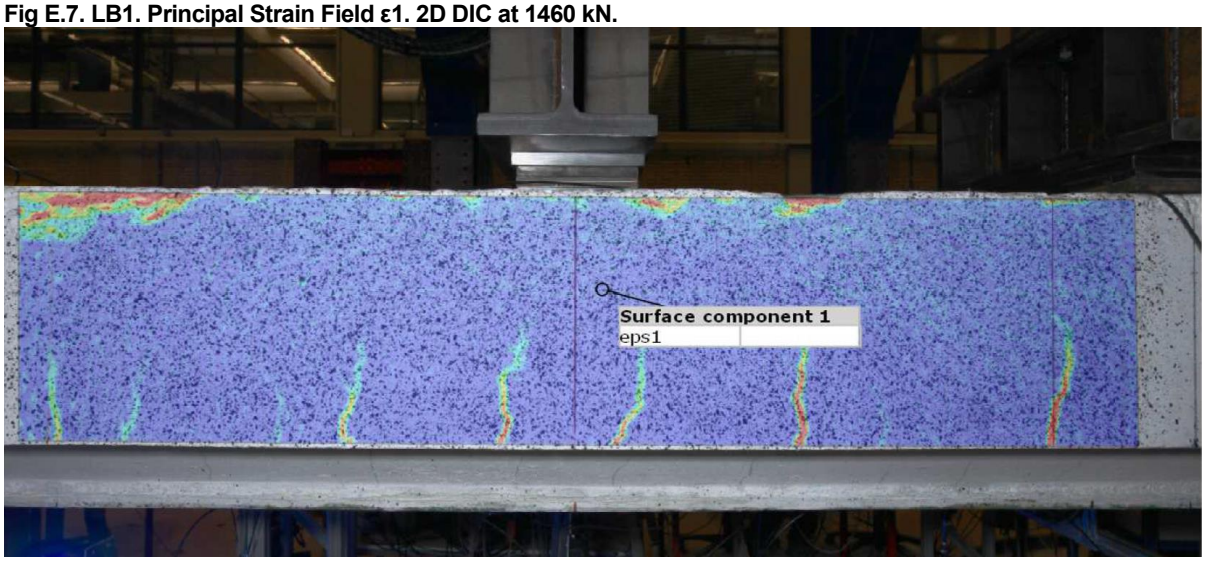

Fig E.8. LB1. Principal Strain Field ε1. 2D DIC at 1500 kN.

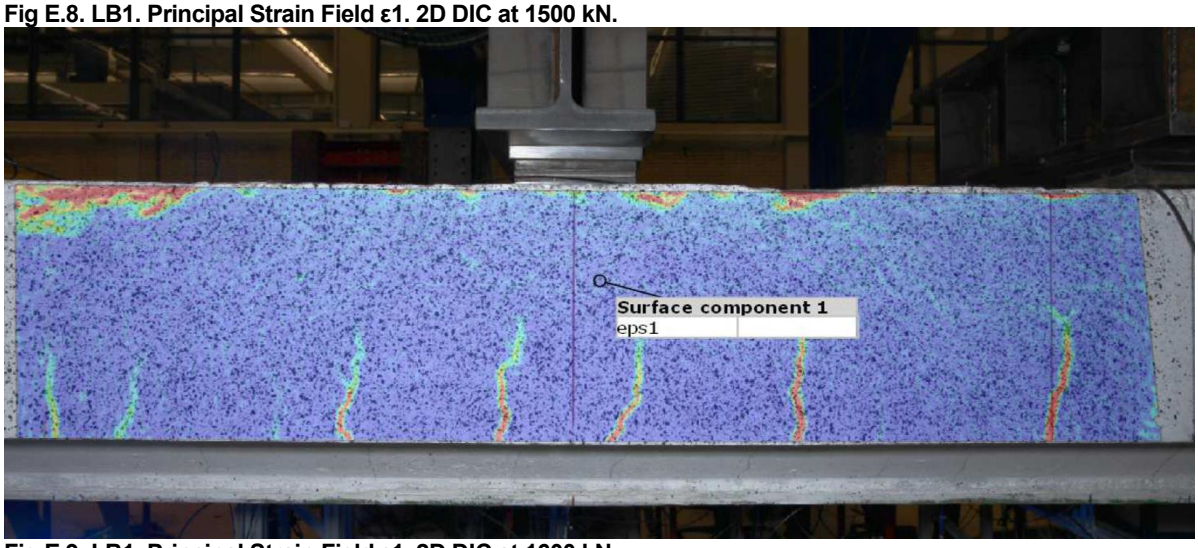

Fig E.9. LB1. Principal Strain Field ε1. 2D DIC at 1600 kN.

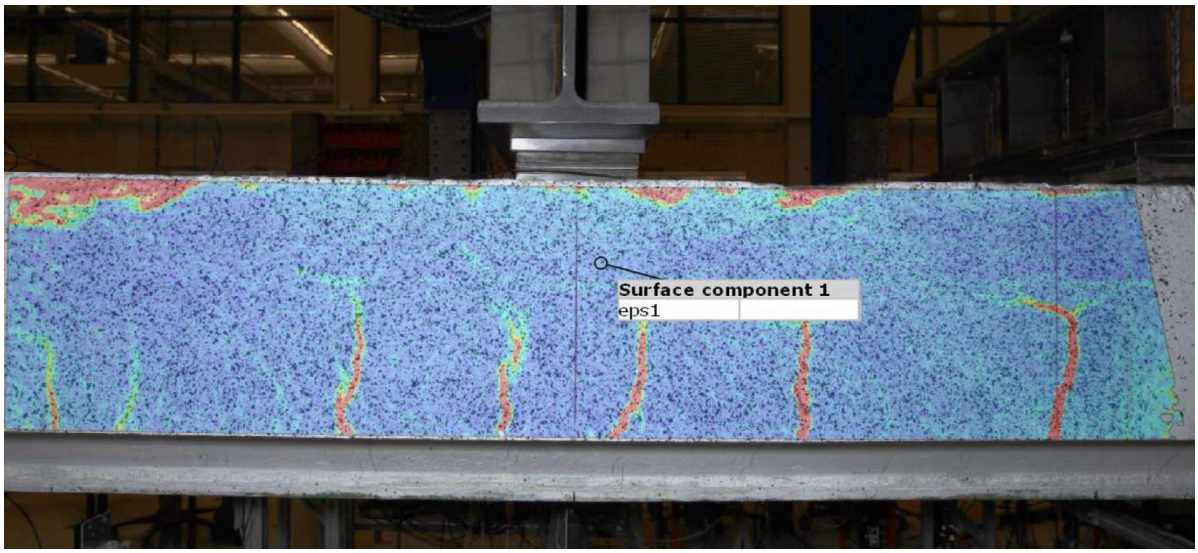

Fig E.10. LB1. Principal Strain Field ε1. 2D DIC at 1638 kN.

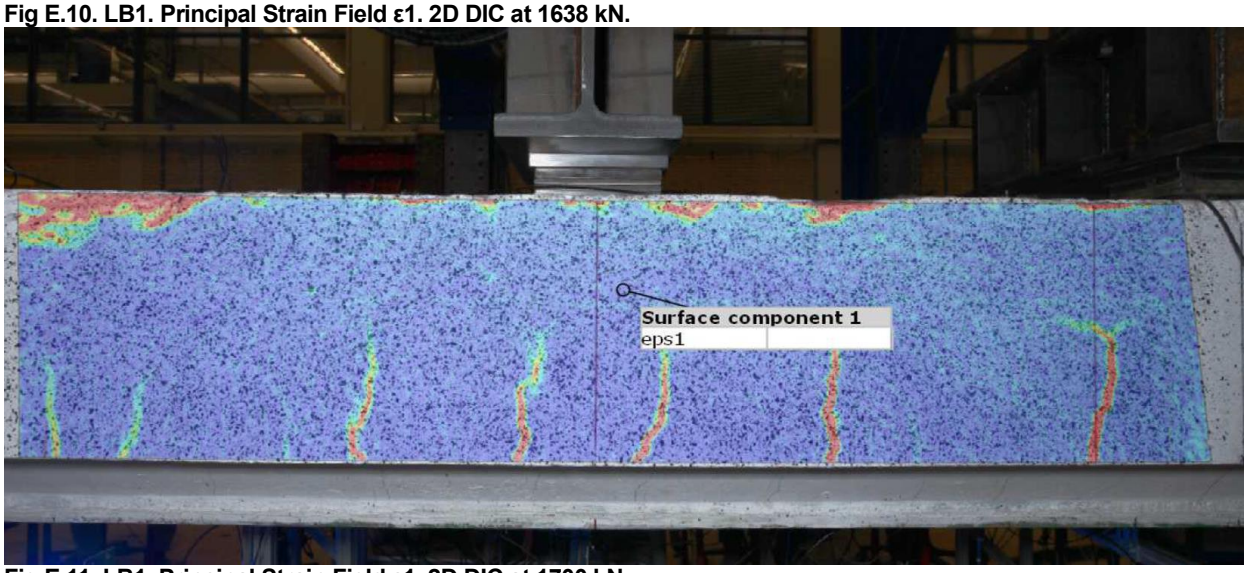

Fig E.11. LB1. Principal Strain Field ε1. 2D DIC at 1700 kN.

F. 3D DIC - LB1

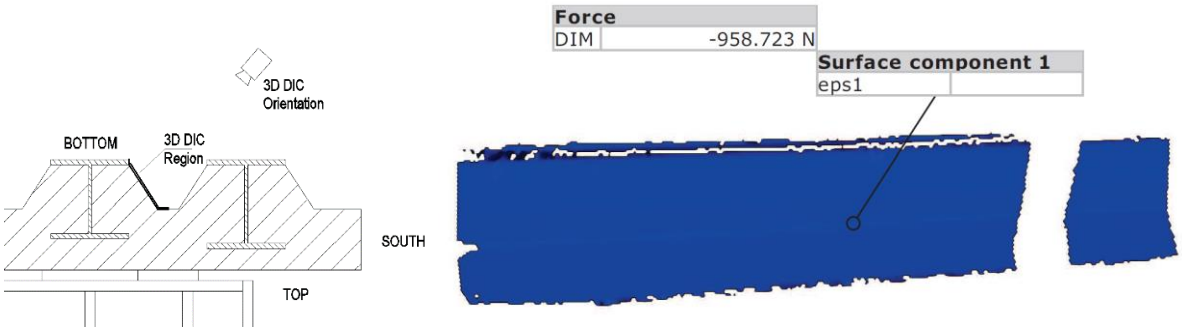

Fig F.1. LB1. Principal Strain Field ε1 3D DIC before loading starts.

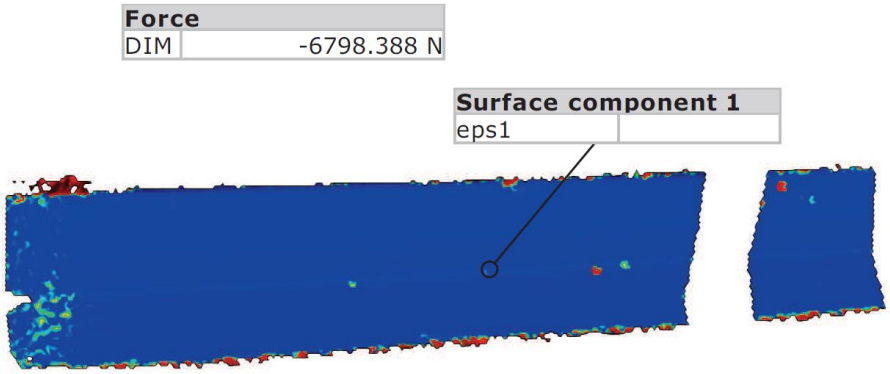

Fig F.2. LB1. Principal Strain Field ε1. 3D DIC at 10 kN.

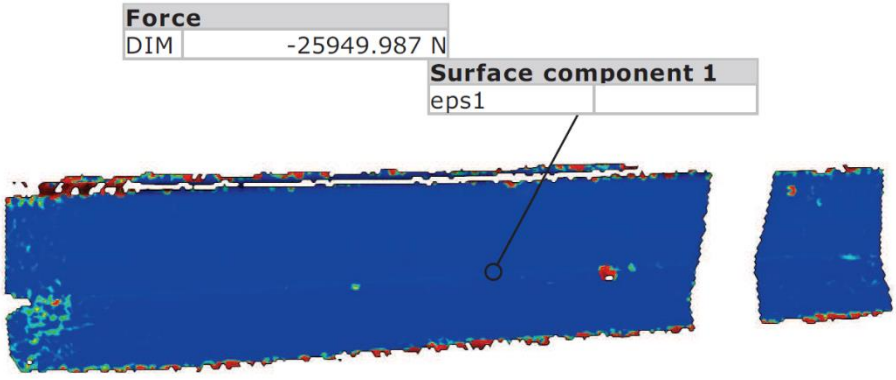

Fig F.3. LB1. Principal Strain Field ε1. 3D DIC at 50 kN.

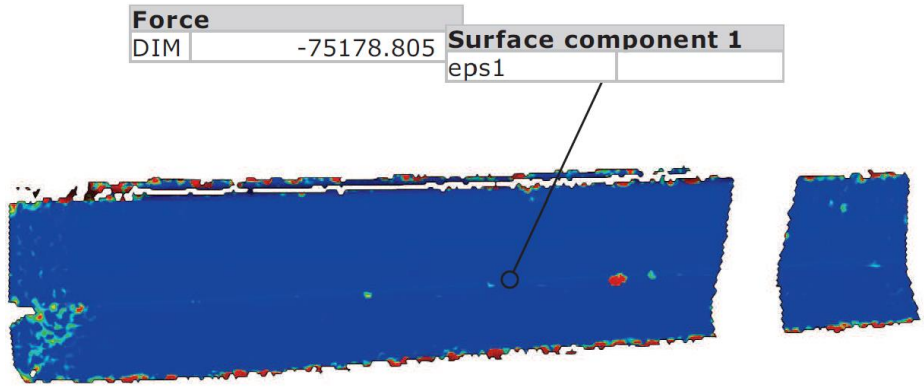

Fig F.4. LB1. Principal Strain Field ε1. 3D DIC at 150 kN.

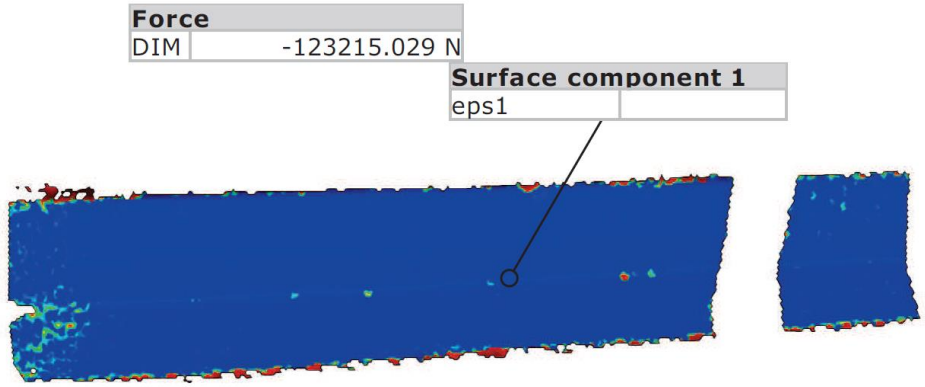

Fig F.5. LB1. Principal Strain Field ε1. 3D DIC at 250 kN.

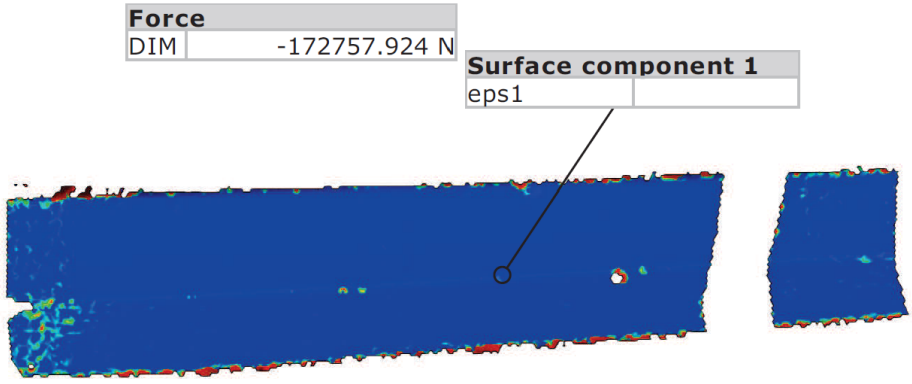

Fig F.6. LB1. 3D DIC at 350 kN.

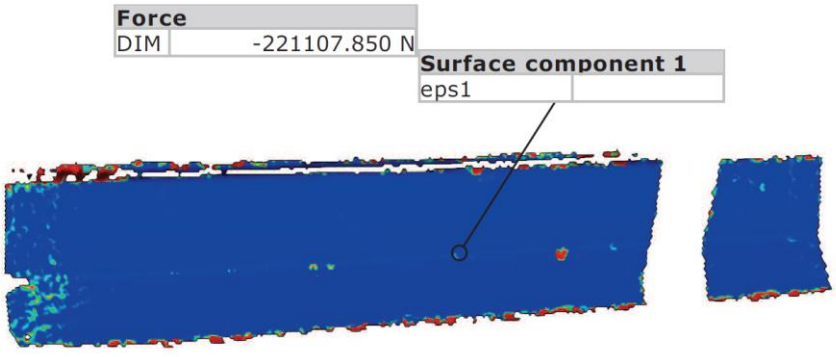

Fig F.7. LB1. Principal Strain Field ε1. 3D DIC at 450 kN.

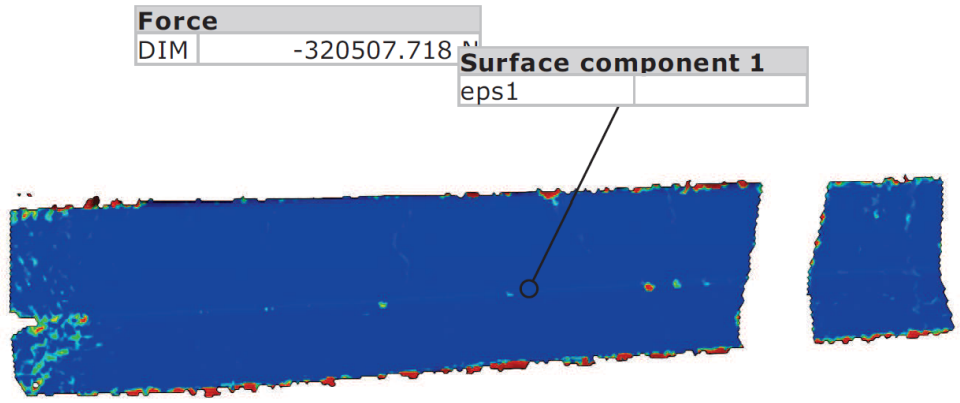

Fig F.8. LB1. Principal Strain Field ε1. 3D DIC at 650 kN.

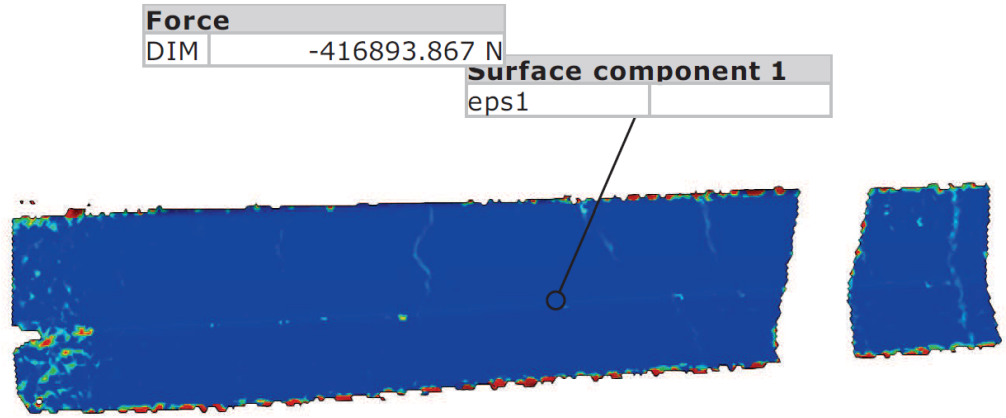

Fig F.9. LB1. Principal Strain Field ε1. 3D DIC at 850 kN.

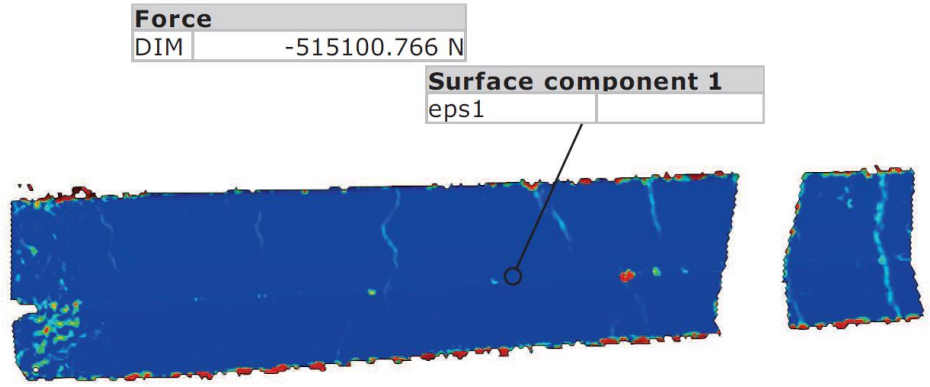

Fig F.10. LB1. Principal Strain Field ε1. 3D DIC at 1050 kN.

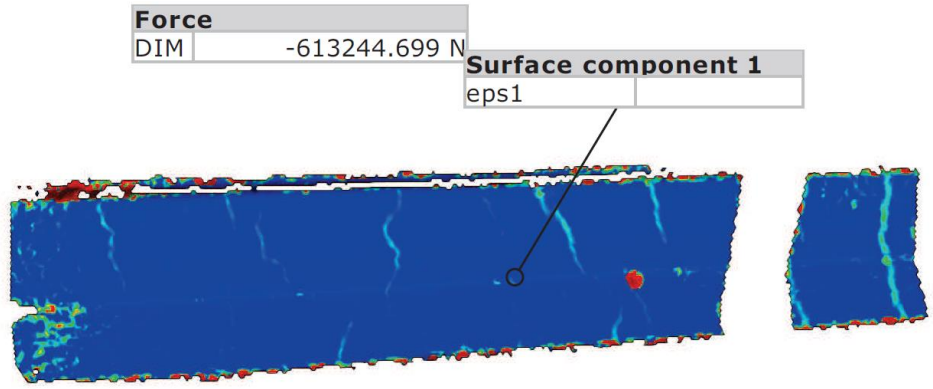

Fig F.11. LB1. Principal Strain Field ε1. 3D DIC at 1250 kN.

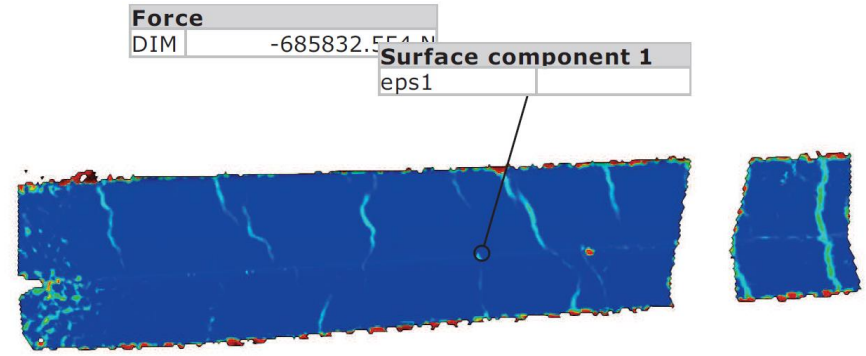

Fig F.12. LB1. Principal Strain Field ε1. 3D DIC at 1400 kN.

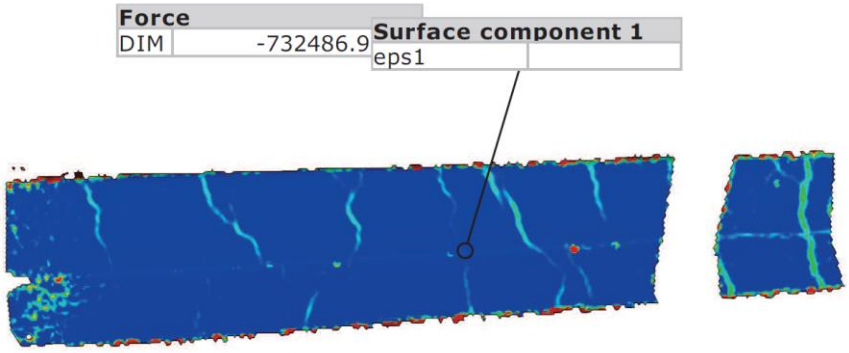

Fig F.13. LB1. Principal Strain Field ε1. 3D DIC at 1500 kN.

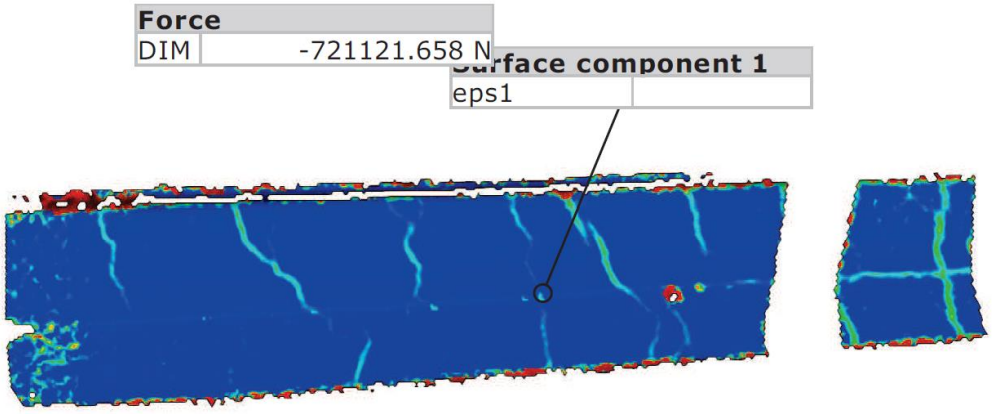

Fig F.14. LB1. 3D DIC at 1460 kN.

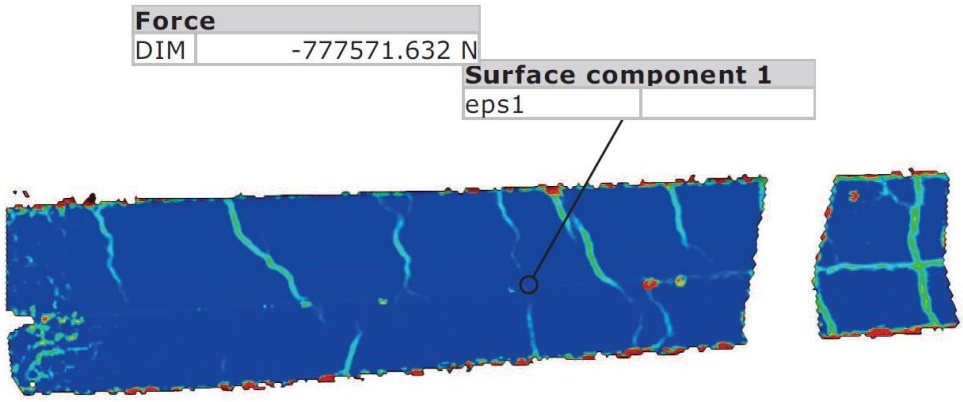

Fig F.15. LB1. Principal Strain Field ε1. 3D DIC at 1600 kN.

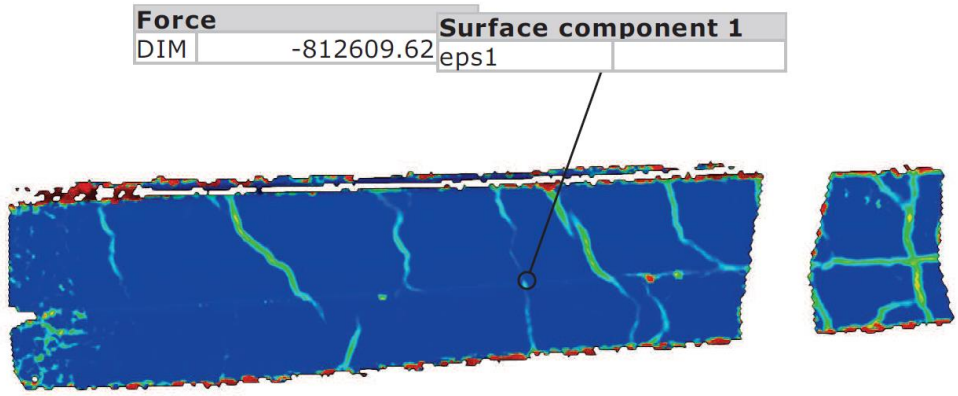

Fig F.16. LB1. Principal Strain Field ε1. 3D DIC at 1650 kN.

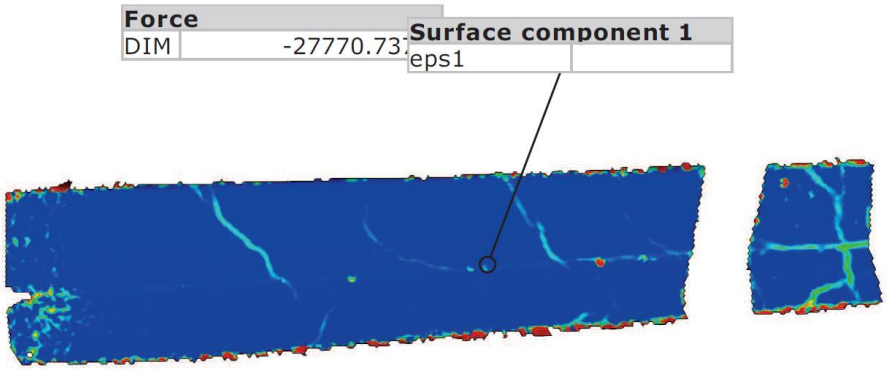

Fig F.17. LB1. Principal Strain Field ε1. 3D DIC at 50 kN.

G. LOAD CELLS - LB3

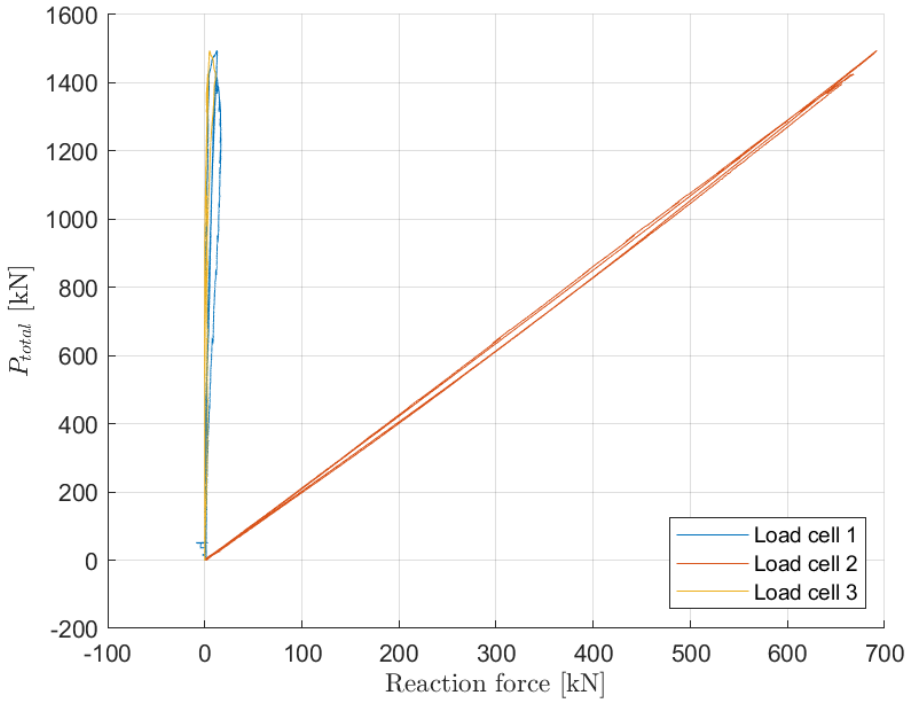

Fig G.1. LB3. Reaction force from load cells versus total load for load cell 1-3.

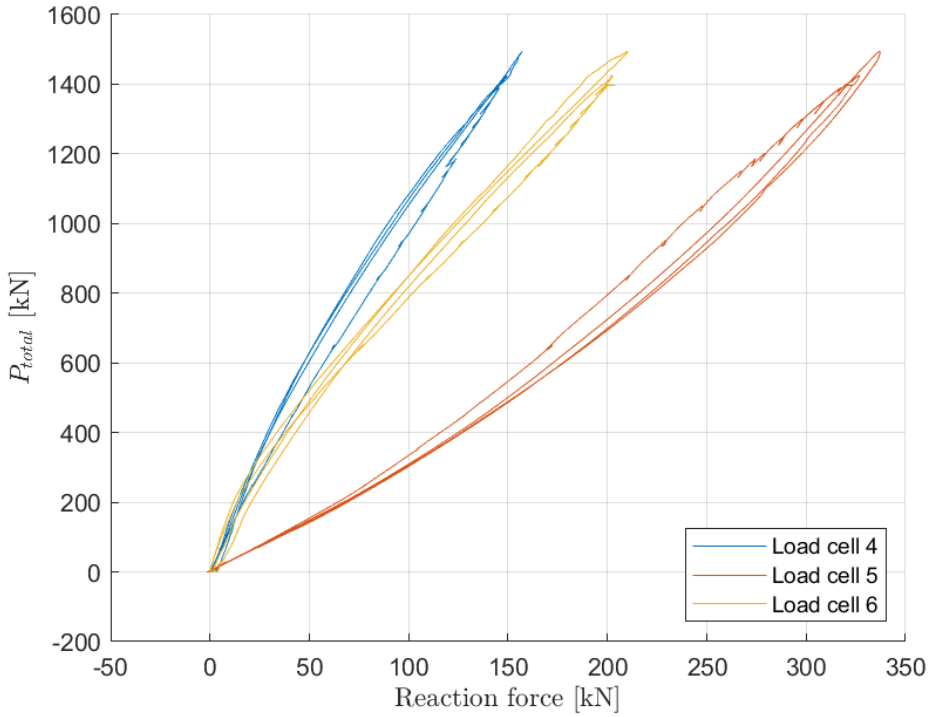

Fig G.2. LB3. Reaction force from load cells versus total load for load cell 4-6.

H. OPTIC FIBERS - LB3

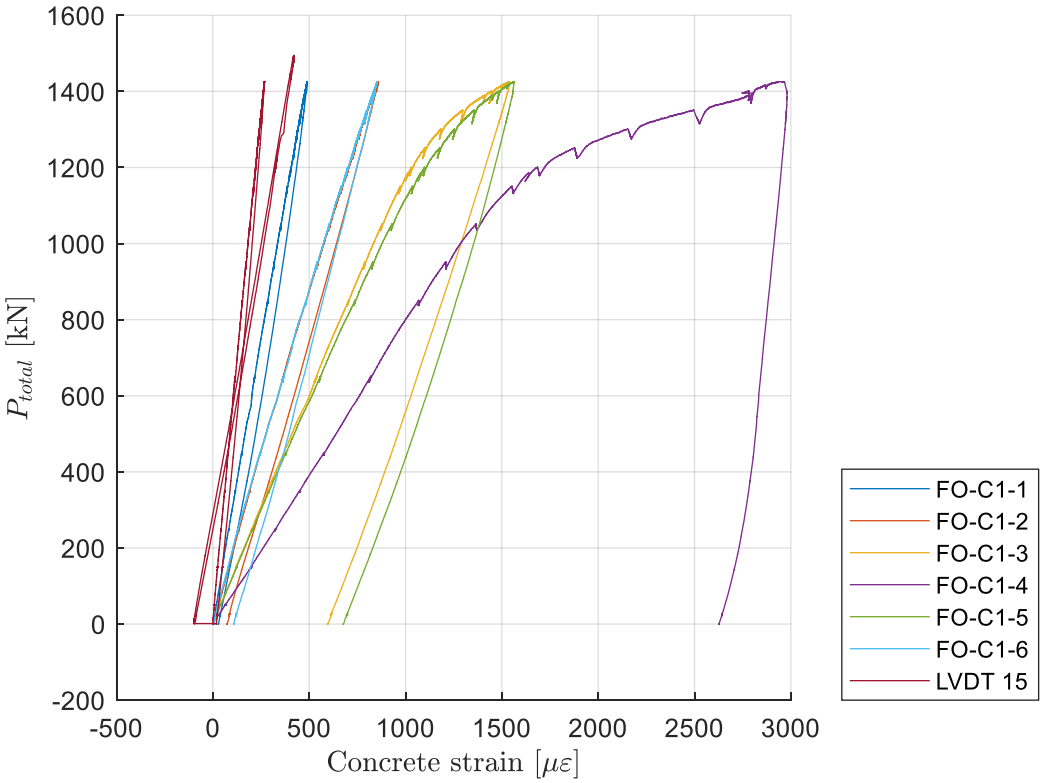

Fig H.1. LB3. Concrete strain versus total load for FO-C1-1 to FO-C1-6 and LVDT 15 at beam 1. FO-C1-7 was damaged during preparation of LB1 and was replaced by LVDT 15.

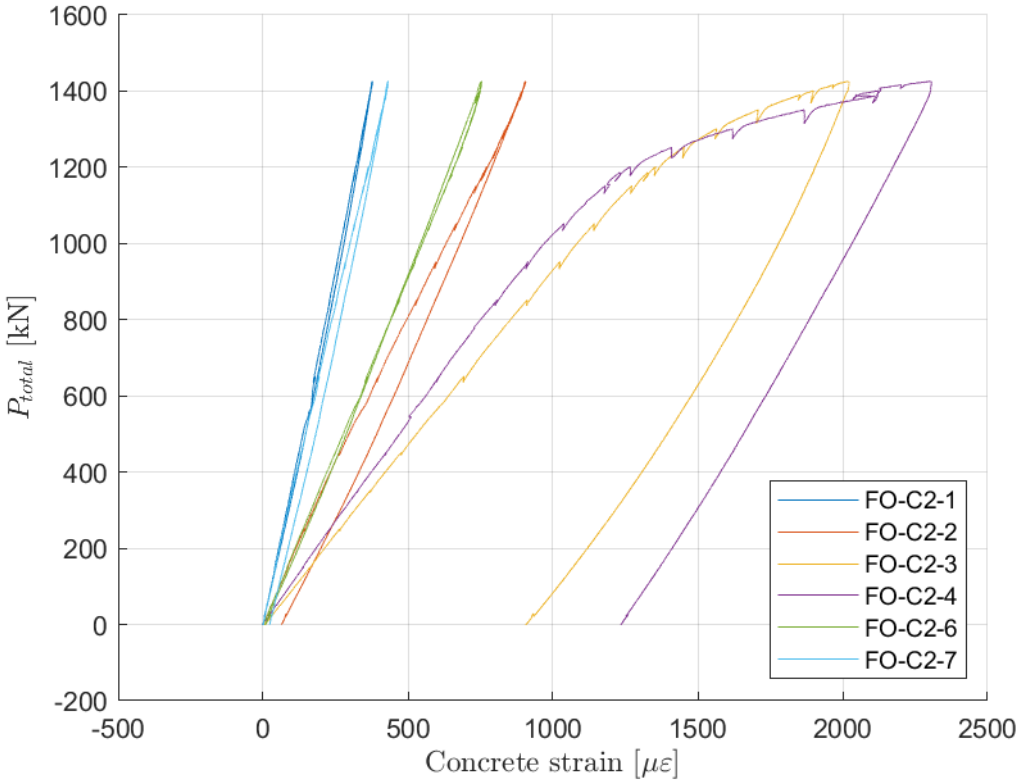

Fig H.2. LB3. Concrete strain versus total load for FO-C2-1 to FO-C2-7 at beam 2. FO-C2-5 fell out of range from the start of the testing.

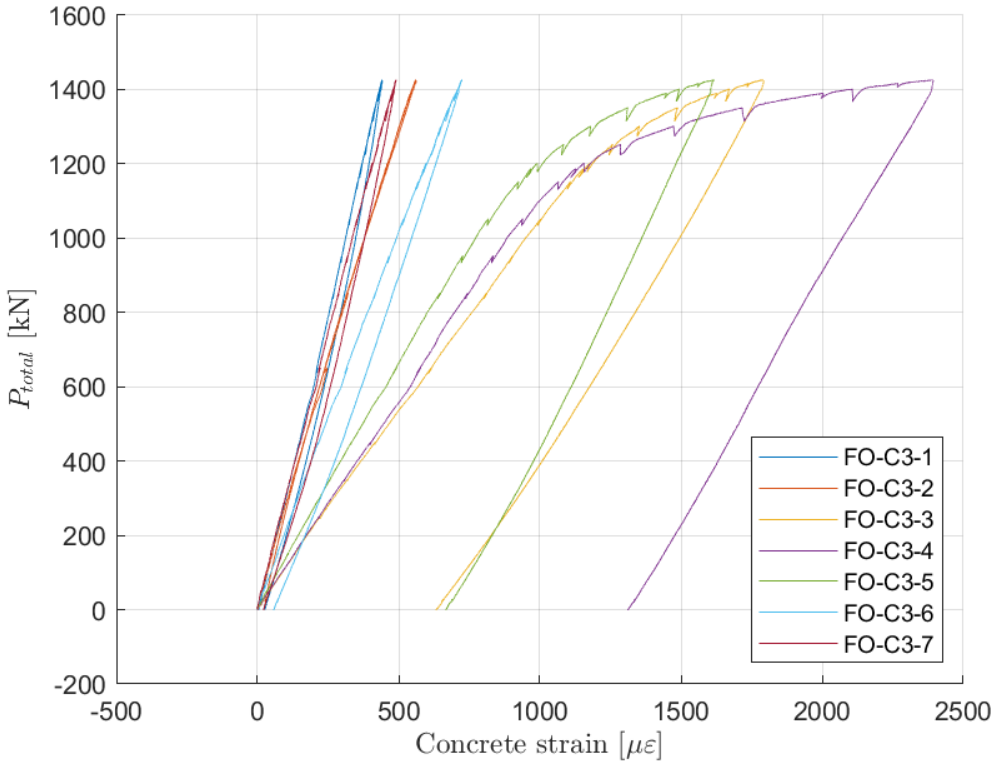

Fig H.3. LB3. Concrete strain versus total load for FO-C3-1 to FO-C3-7 at beam 3.

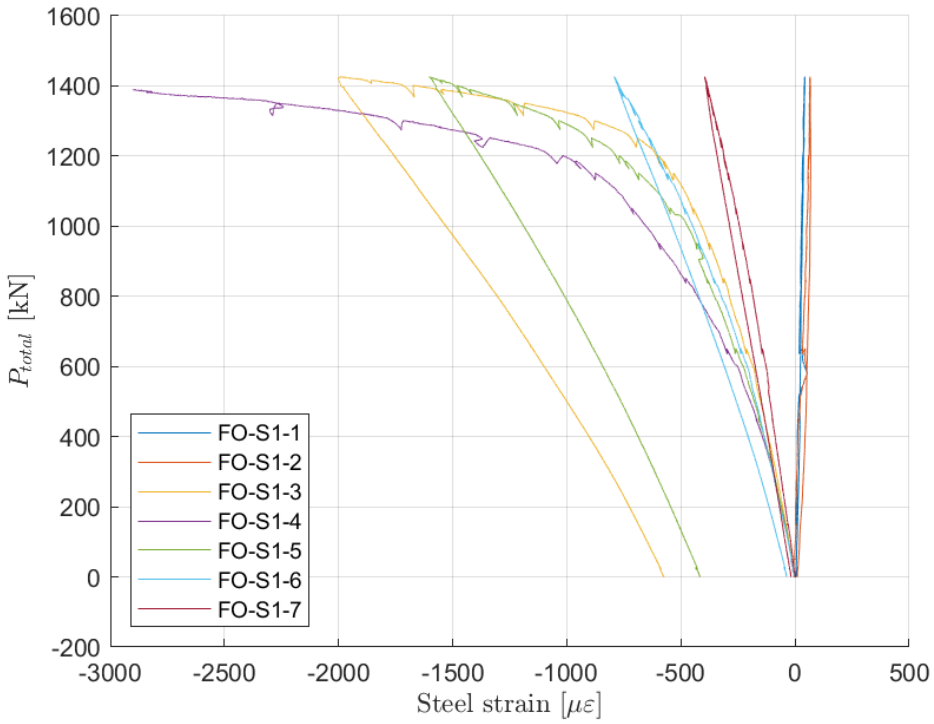

Fig H.4. LB3. Steel strain versus total load for FO-S1-1 to FO-S1-7 at beam 1. FO-S1-4 fell out of range and the measuring stopped when it reached its maximum strain.

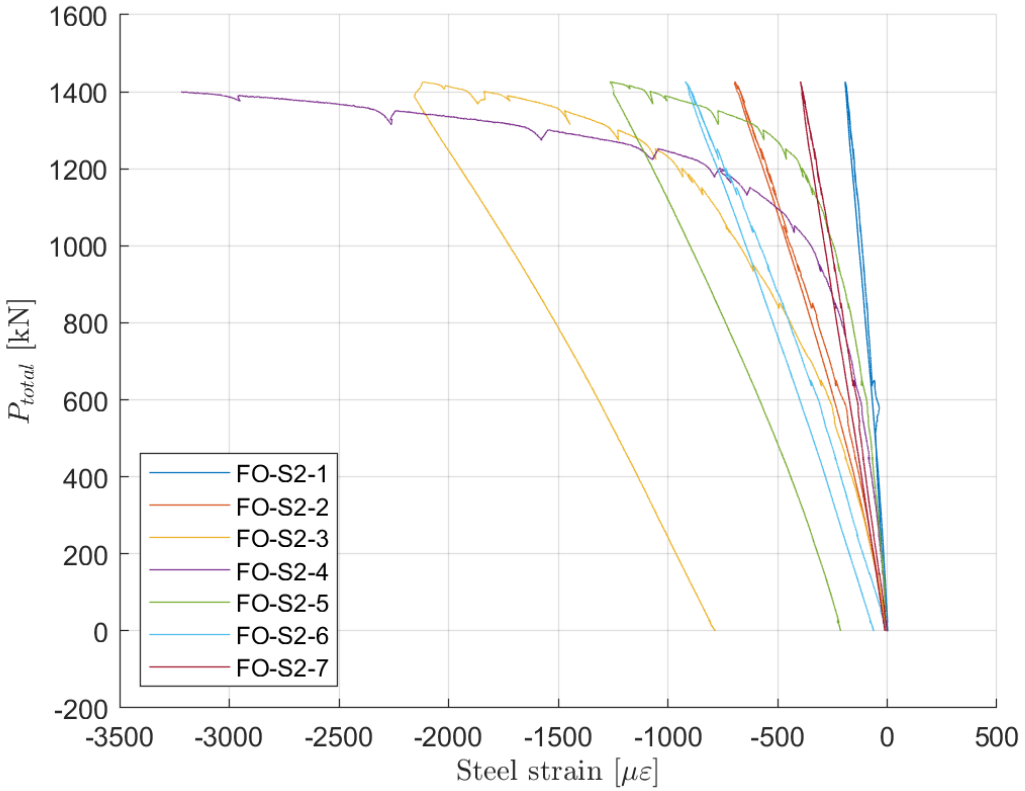

Fig H.5. LB3. Steel strain versus total load for FO-S2-1 to FO-S2-7 at beam 2. Around 1400 kN FO-S2-4 fell out of range. FO-S2-1 also fell out of range, the measurements following this have been left out.

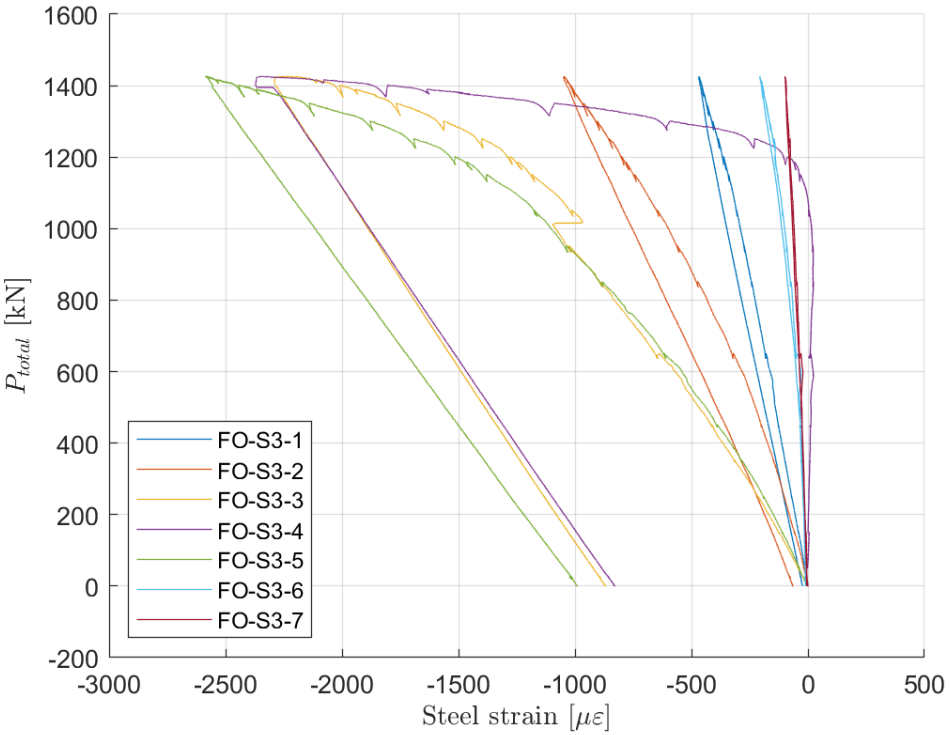

Fig H.6. LB3. Steel strain versus total load for FO-S3-1 to FO-S3-7 at beam 3.

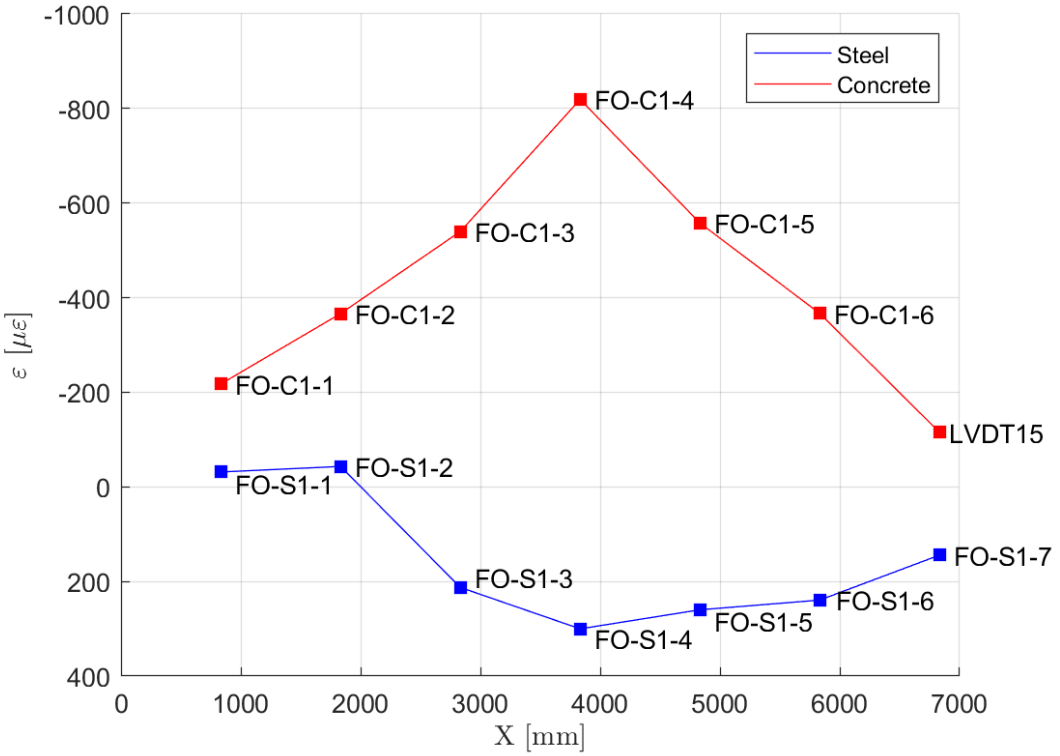

Fig H.7. LB3. Point A - Cracking starts (Ptotal=650 kN). X, the position of the optic fibers from the support, versus the strain measured for optic fibers above and below beam 1. FO-C1-7 broke during preparation of LB1 and was replaced by LVDT 15.

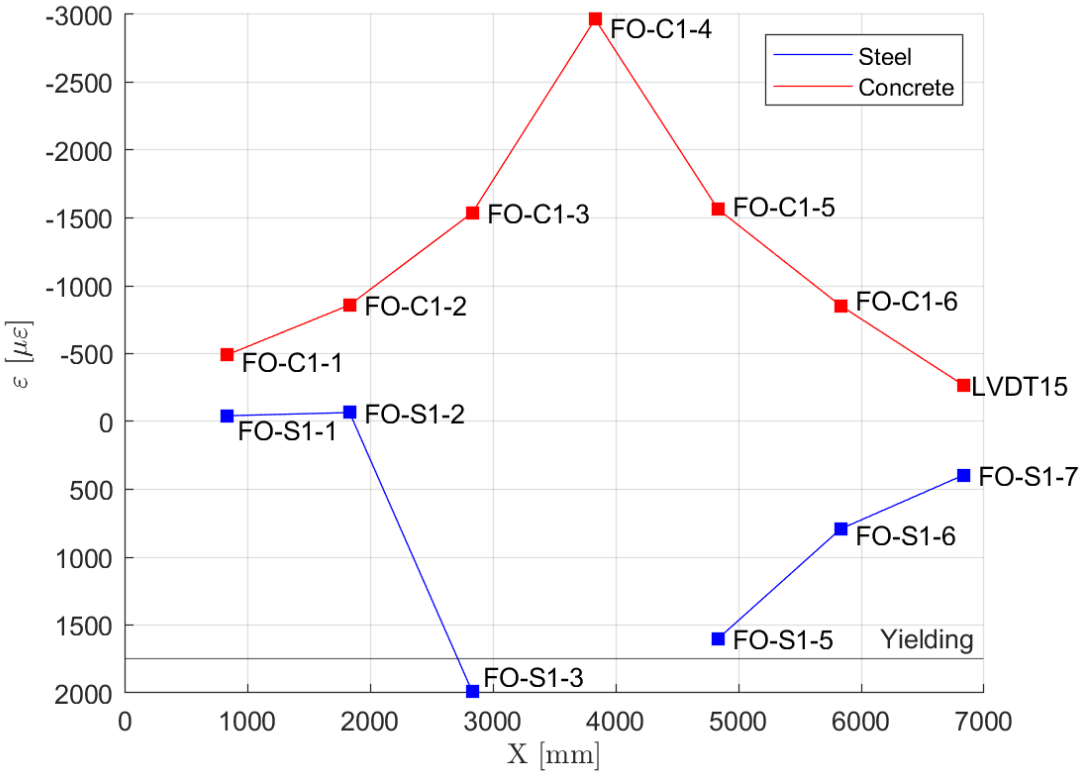

Fig H.8. LB3. Point C - Max load of first loading (Ptotal=1426 kN). X, the position of the optic fibers from the support, versus the strain measured for optic fibers above and below beam 1. FO-S1-4 fell out of range. FO-C1-7 broke during preparation of LB1 and was replaced by LVDT 15.

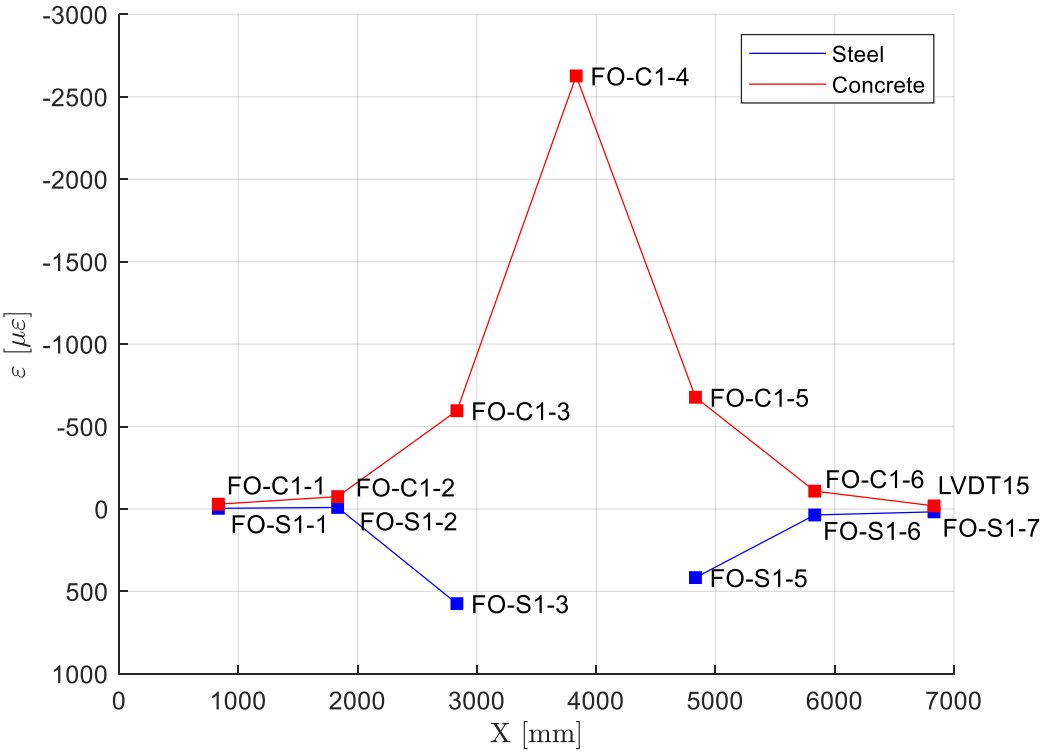

Fig H.9. LB3. Point D - Unloading to increase the displacement range of the hydraulic jacks (Ptotal=0 kN). X, the position of the optic fibers from the support, versus the strain measured for optic fibers above and below beam 1. FO-S1-4 fell out of range. FO-C1-7 broke during preparation of LB1 and was replaced by LVDT 15.

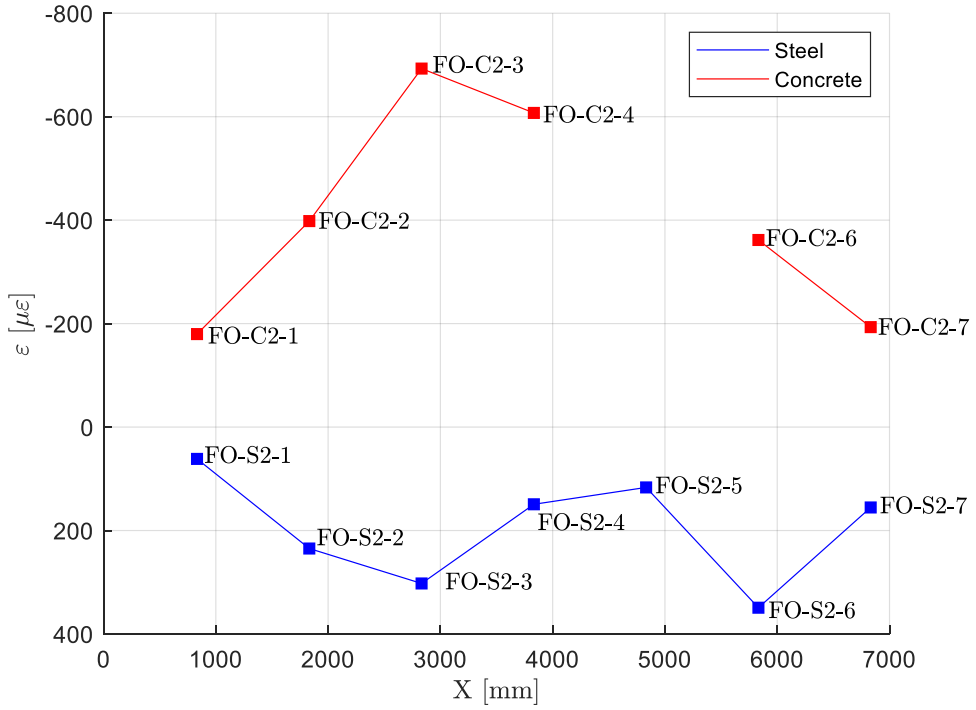

Fig H.10. LB3. Point A - Cracking starts (Ptotal=650 kN). X, the position of the optic fibers from the support, versus the strain measured for optic fibers above and below beam 2. FO-C2-5 fell out of range.

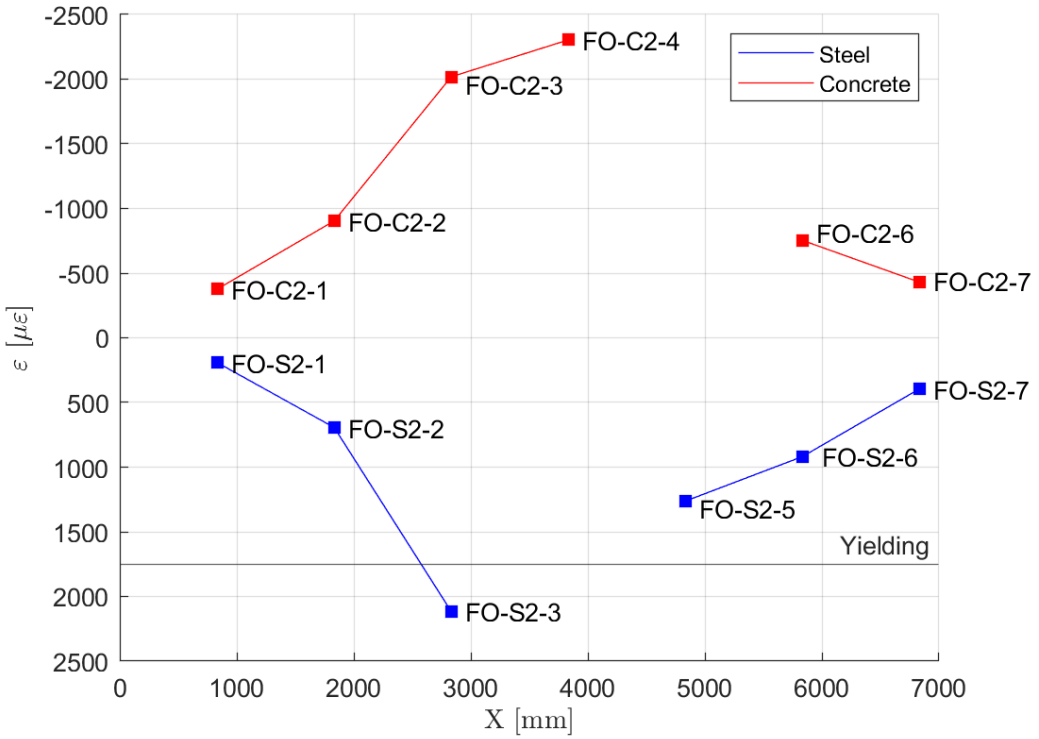

Fig H.11. LB3. Point C - Max load of first loading (Ptotal=1426 kN). X, the position of the optic fibers from the support, versus the strain measured for optic fibers above and below beam 2. FO-C2-5 and FO-S2-4 fell out of range.

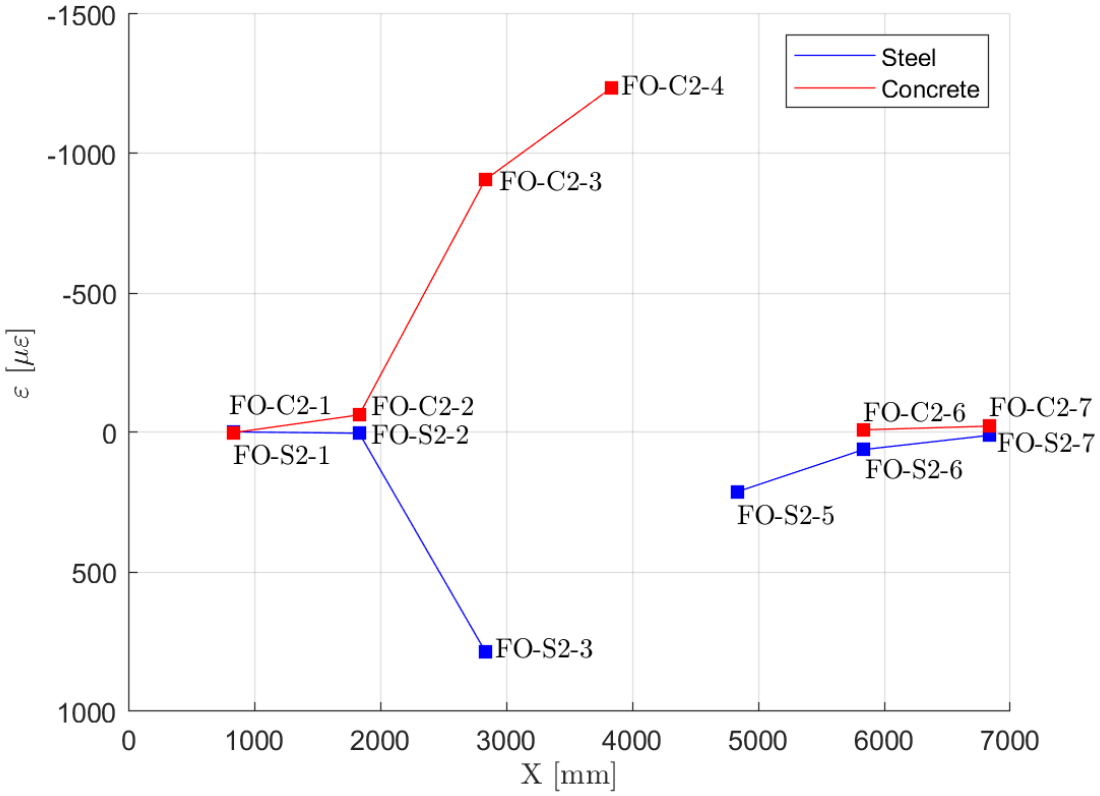

Fig H.12. LB3. Point D - Unloading to increase the displacement range of the hydraulic jacks (Ptotal=0 kN). X, the position of the optic fibers from the support, versus the strain measured for optic fibers above and below beam 2. FO-C2-5 and FO-S2-4 fell out of range.

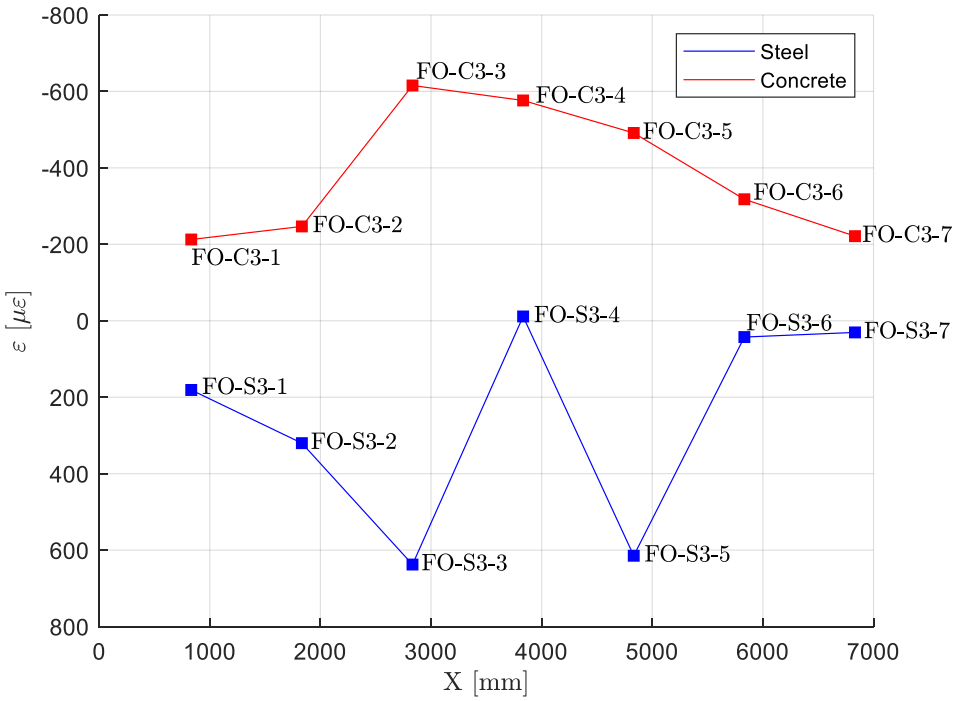

Fig H.13. LB3. Point A - Cracking starts (Ptotal=650 kN). X, the position of the optic fibers from the support, versus the strain measured for optic fibers above and below beam 3. The strain at FO-S3-4 first started to increase after yielding.

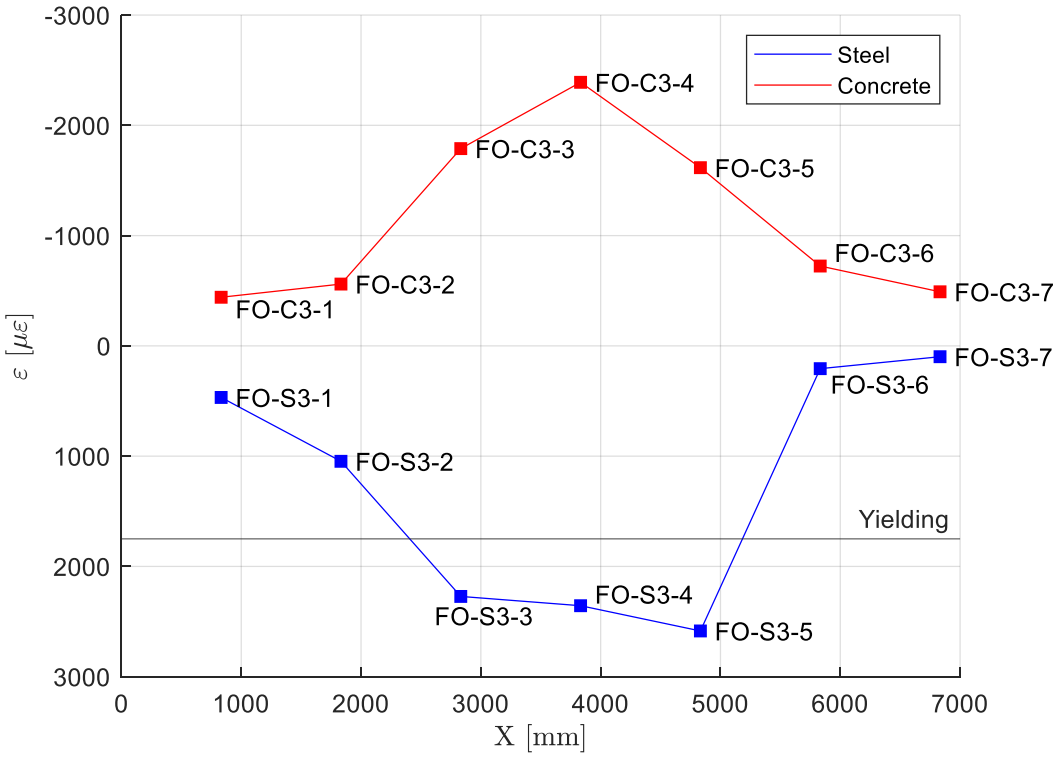

Fig H.14. LB3. Point C - Max load of first loading (Ptotal=1426 kN). X, the position of the optic fibers from the support, versus the strain measured for optic fibers above and below beam 3.

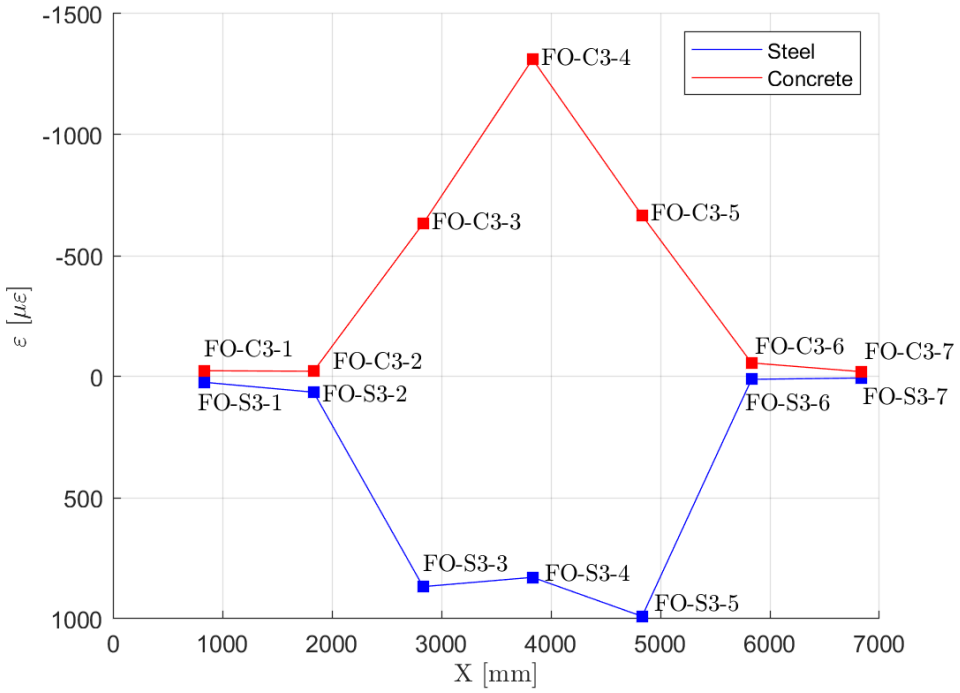

Fig H.15. LB3. Point D - Unloading to increase the displacement range of the hydraulic jacks (Ptotal=0 kN). X, the position of the optic fibers from the support, versus the strain measured for optic fibers above and below beam 3.

I. LASERS - LB3

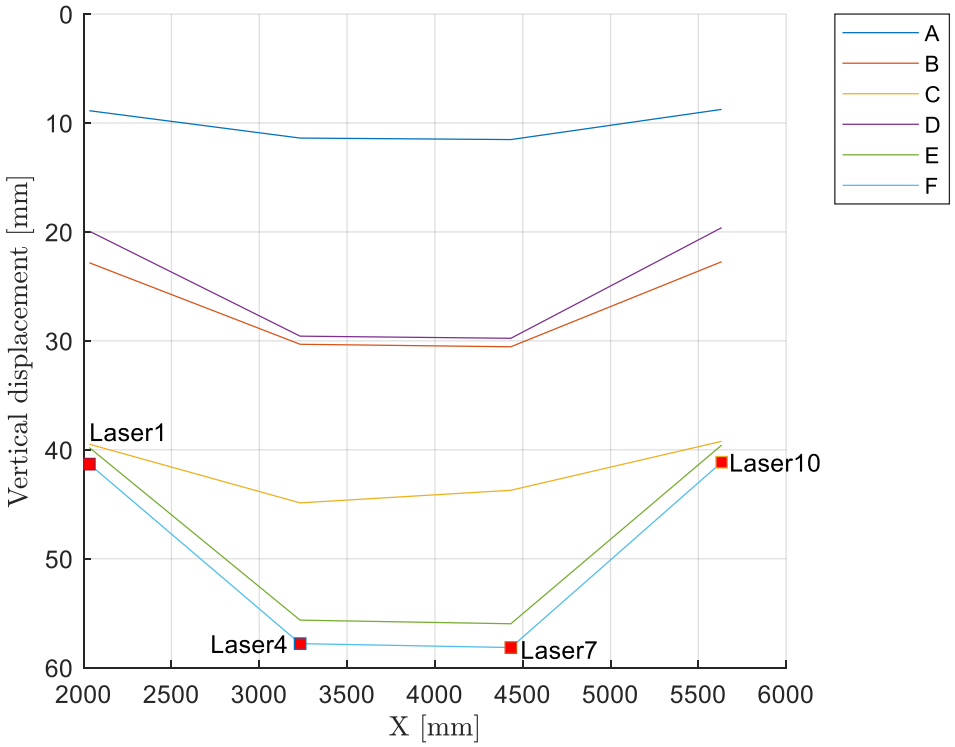

Fig I.1. LB3. Point A-F for laser 1, 4, 7 and 10 positioned at beam 1. X, distance to the support, versus the total vertical displacement. Laser 1 has been linearized as it measured jumps at different intervals.

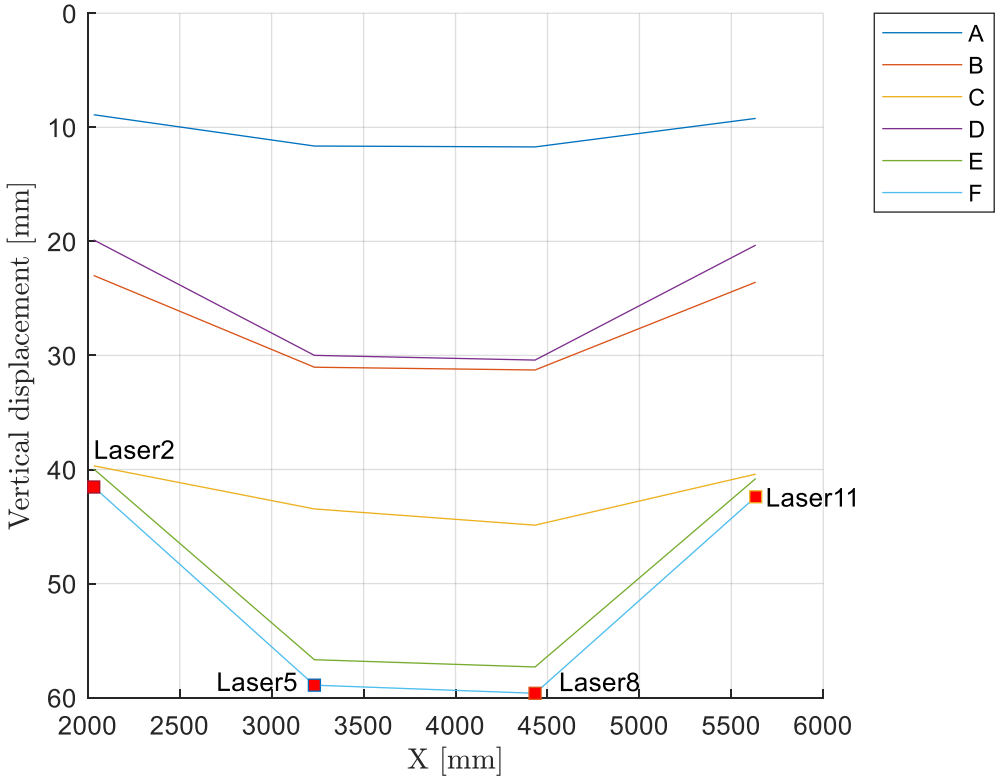

Fig I.2. LB3. Point A-F for laser 2, 5, 8 and 11 positioned at beam 2. X, distance to the support, versus the total vertical displacement.

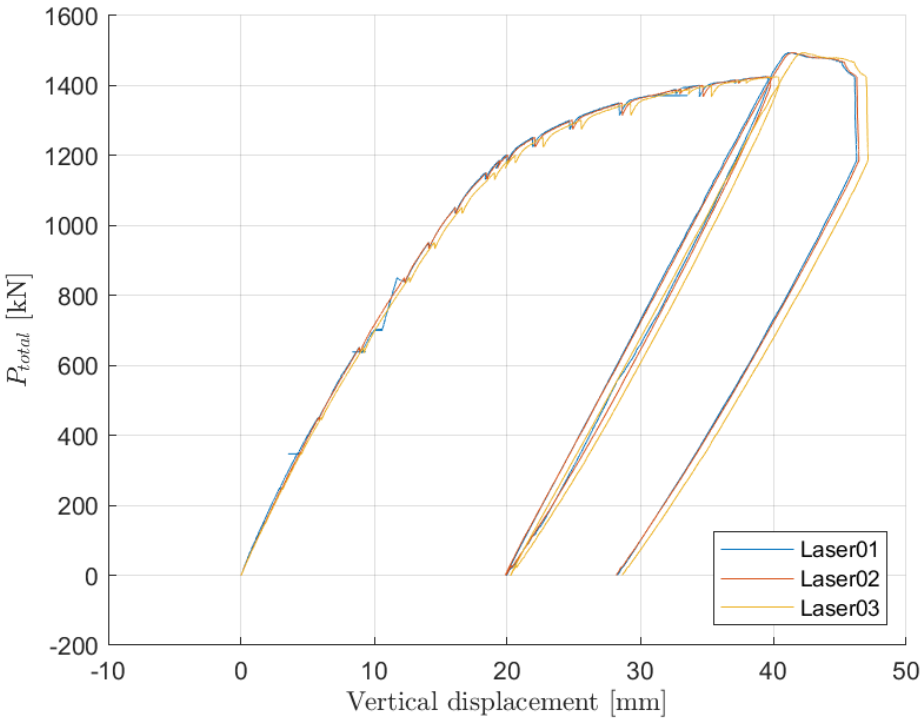

Fig I.3. Total vertical displacement versus load for laser 1-3. Laser 1 has been linearized as it measured jumps at different intervals.

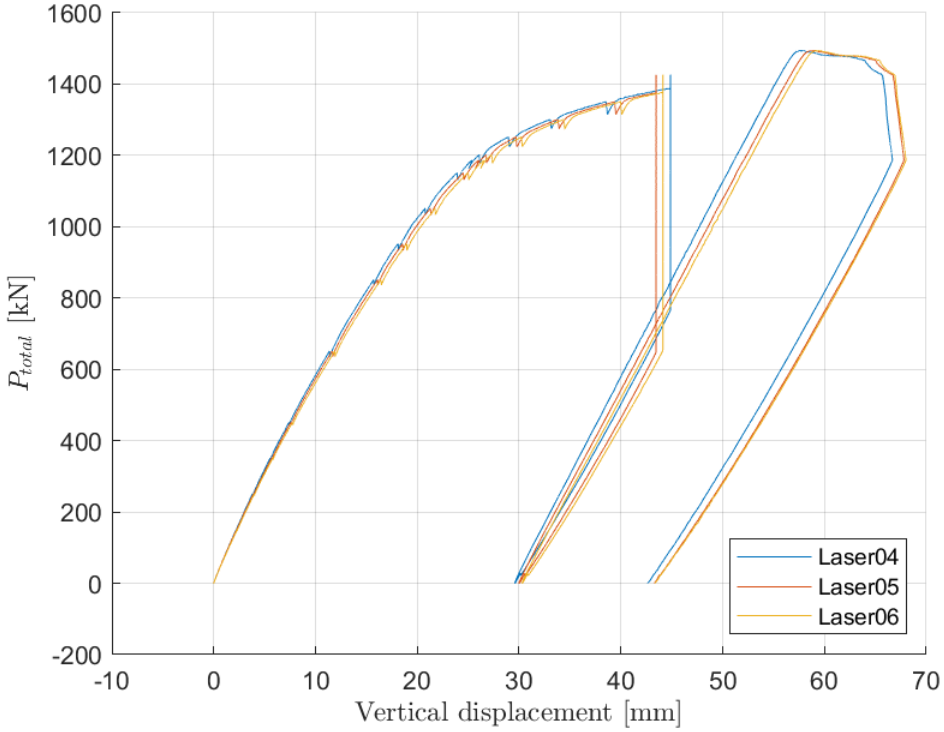

Fig I.4. LB3. Total vertical displacement versus load for laser 4-6.

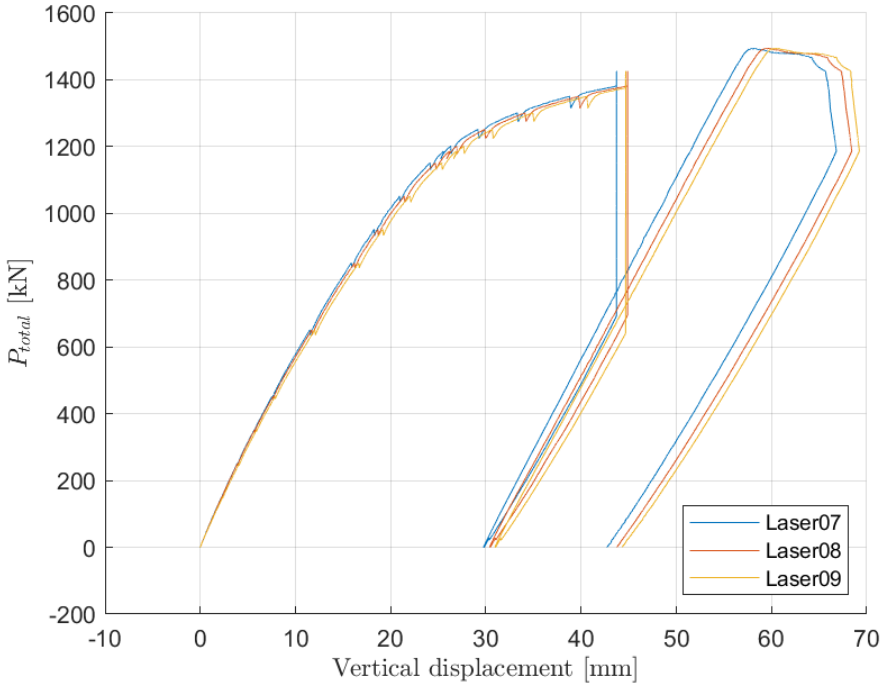

Fig I.5. Vertical displacement versus load for laser 7-9.

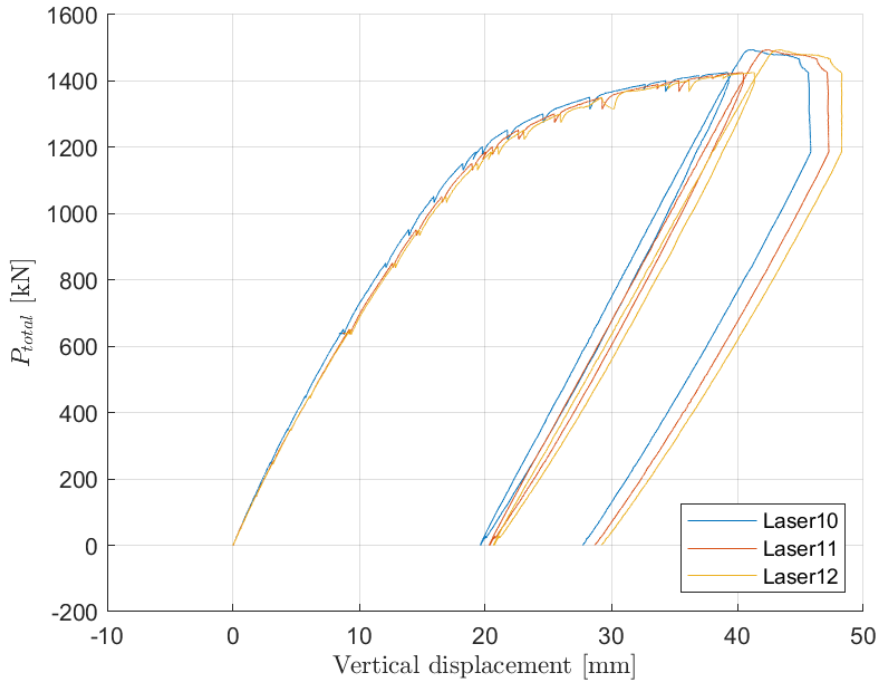

Fig I.6. Vertical displacement versus load for laser 10-12. Laser 12 has been linearized as the measurement had a jump.

J. LVDTS - LB3

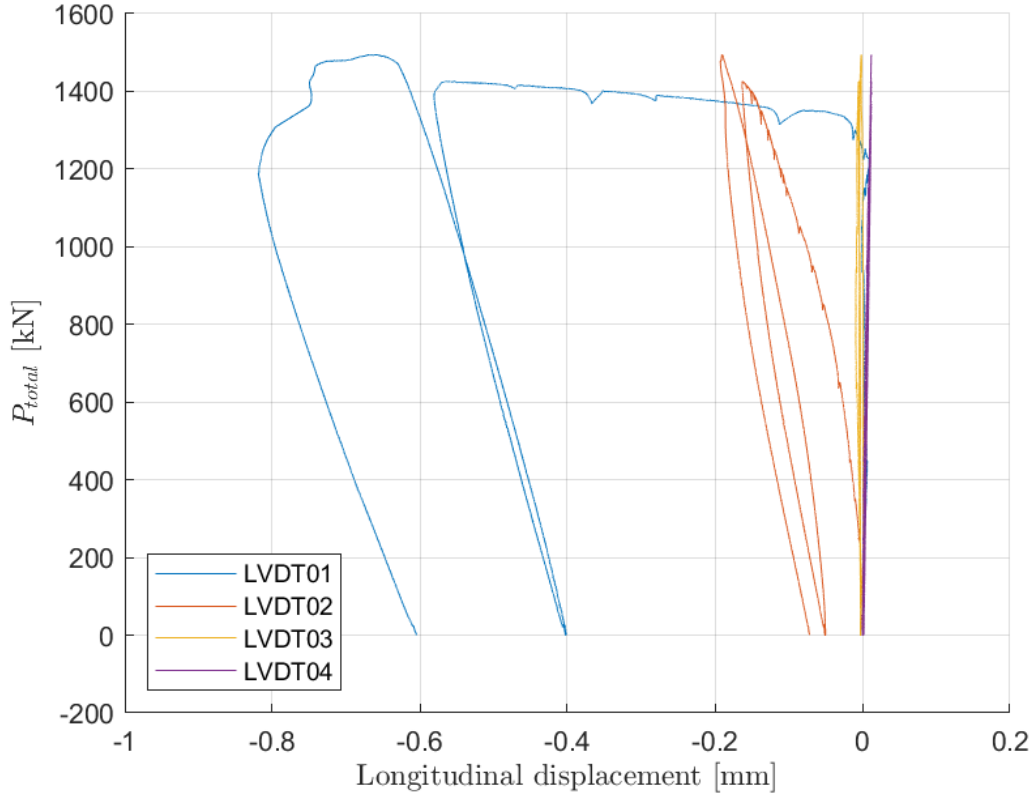

Fig J.1. LB3. Relative longitudinal displacement between bottom flange and concrete versus total load for LVDT 1-4 at beam 2.

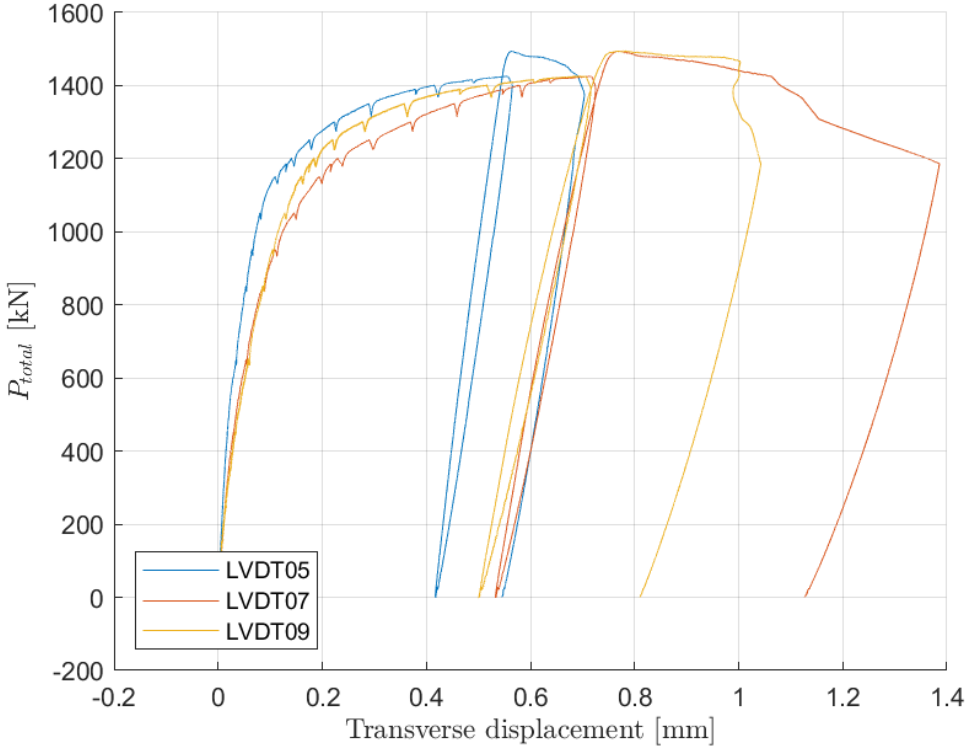

Fig J.2. LB3. Relative transverse displacement between beams 1 and 2 versus total load for LVDT 5, 7 and 9.

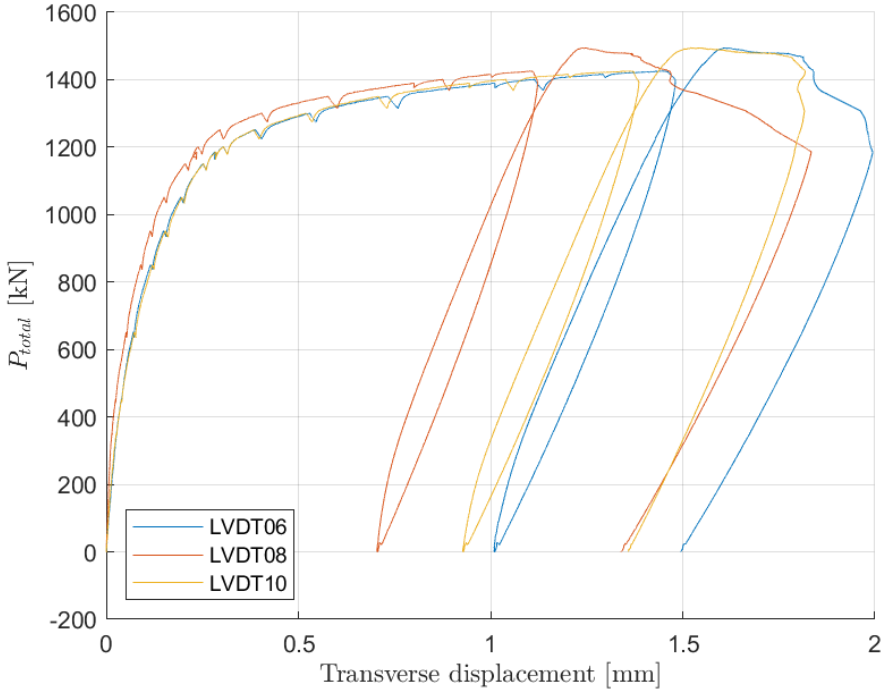

Fig J.3. LB3. Relative transverse displacement between beams 2 and 3 versus total load for LVDT 6, 8 and 10.

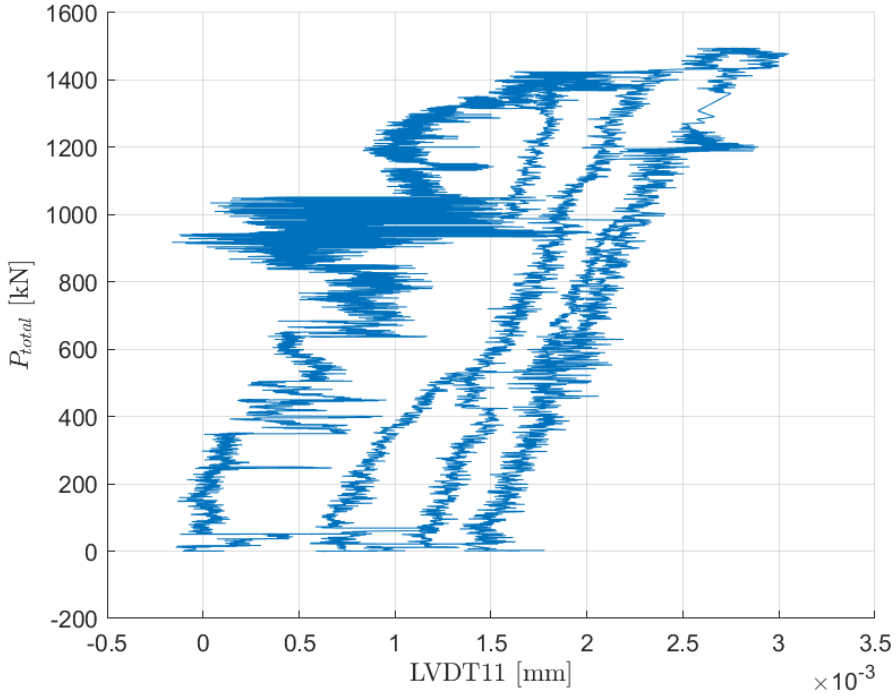

Fig J.4. LB3. Relative longitudinal displacement between concrete and bottom flange at beam 2 versus total load.

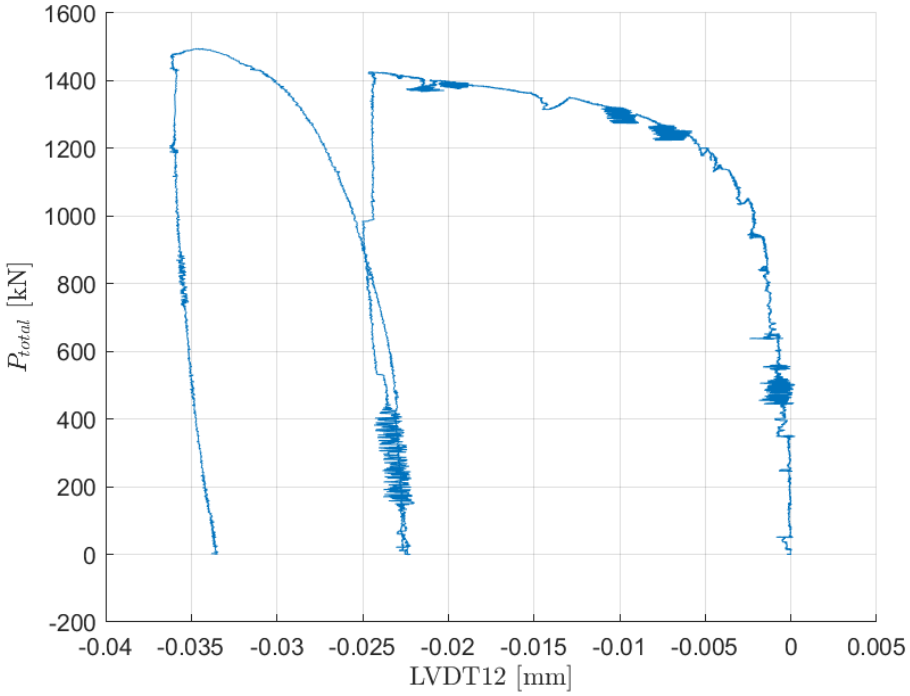

Fig J.5. LB3. Relative longitudinal displacement between concrete and top flange at beam 2 versus total load.

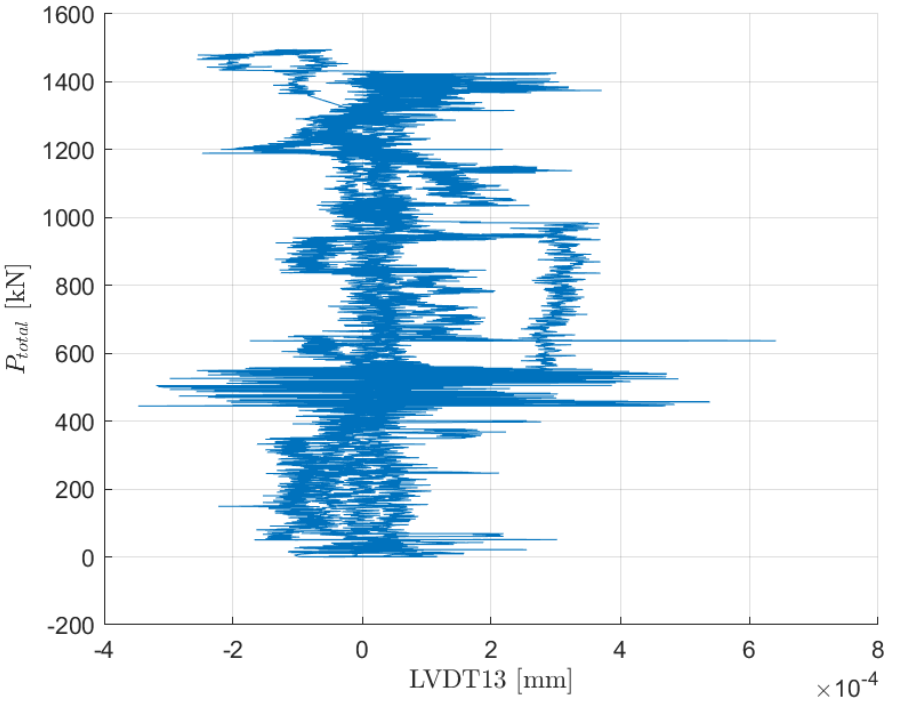

Fig J.6. LB3. Relative longitudinal displacement between concrete and bottom flange at beam 1 versus total load.

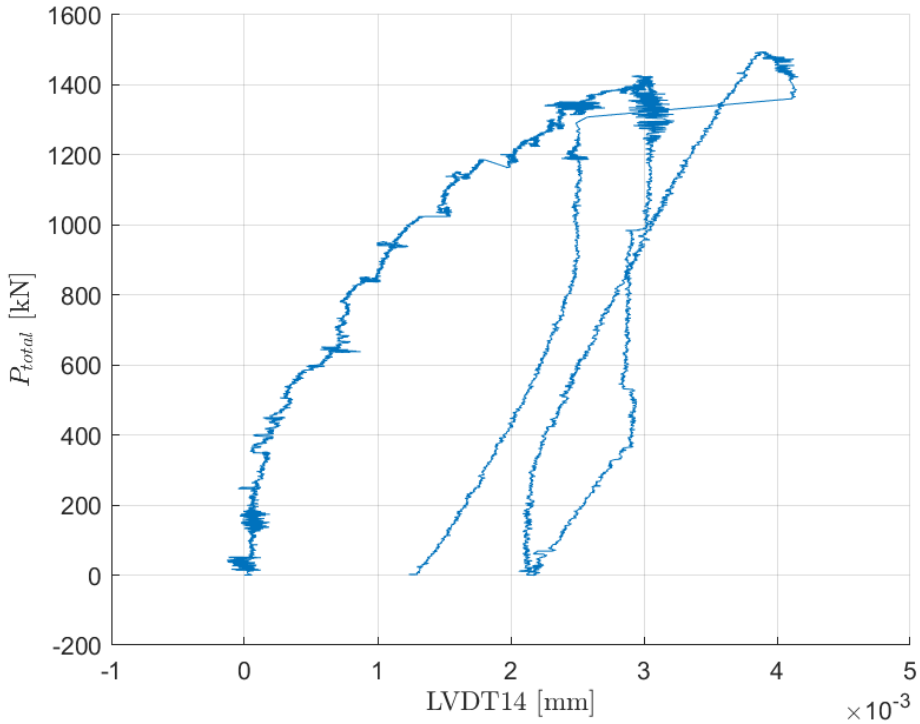

Fig J.7. LB3. Relative longitudinal displacement between concrete and top flange at beam 1 versus total load.

K.2D DIC - LB3

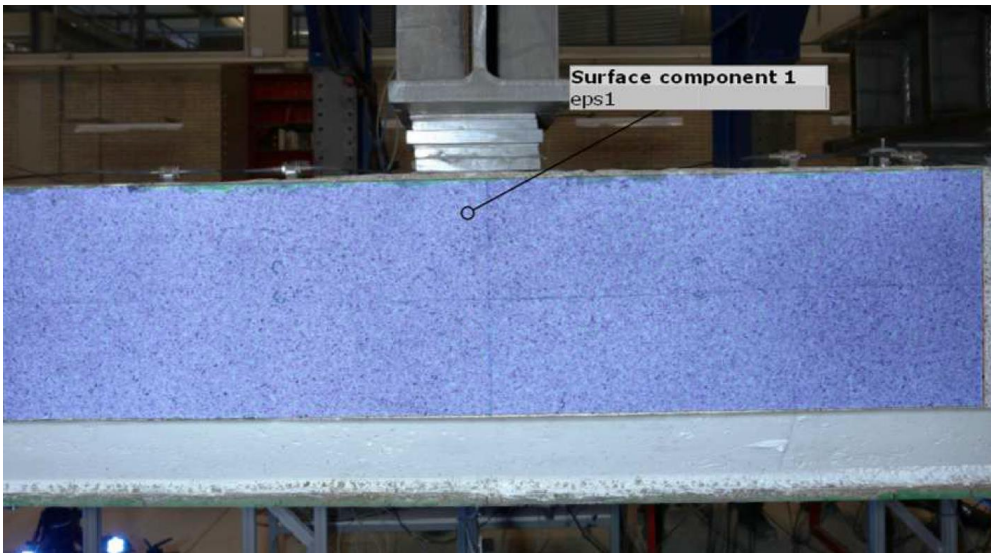

Fig K.1. LB3. Principal Strain Field ε1. 2D DIC at 50 kN.

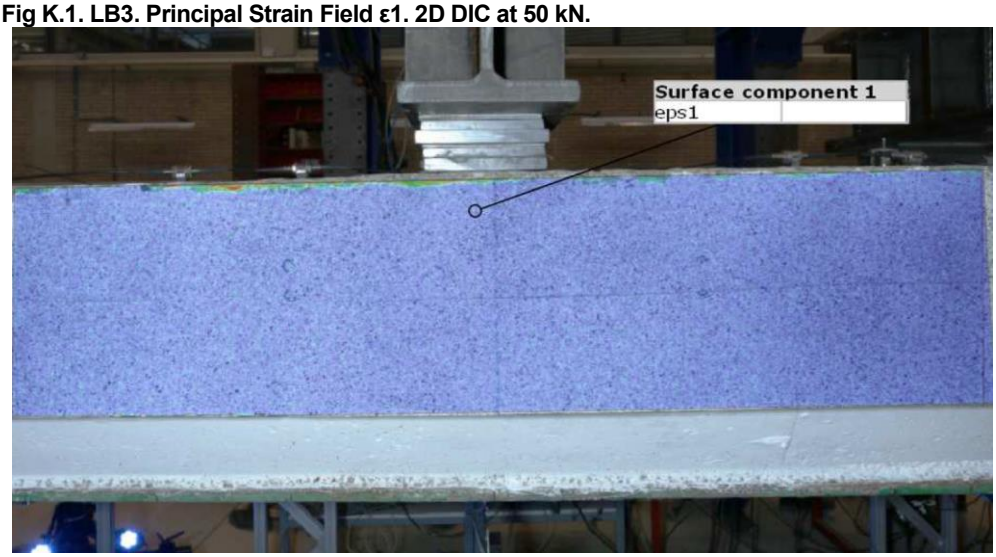

Fig K.2. LB3. Principal Strain Field ε1. 2D DIC at 150 kN.

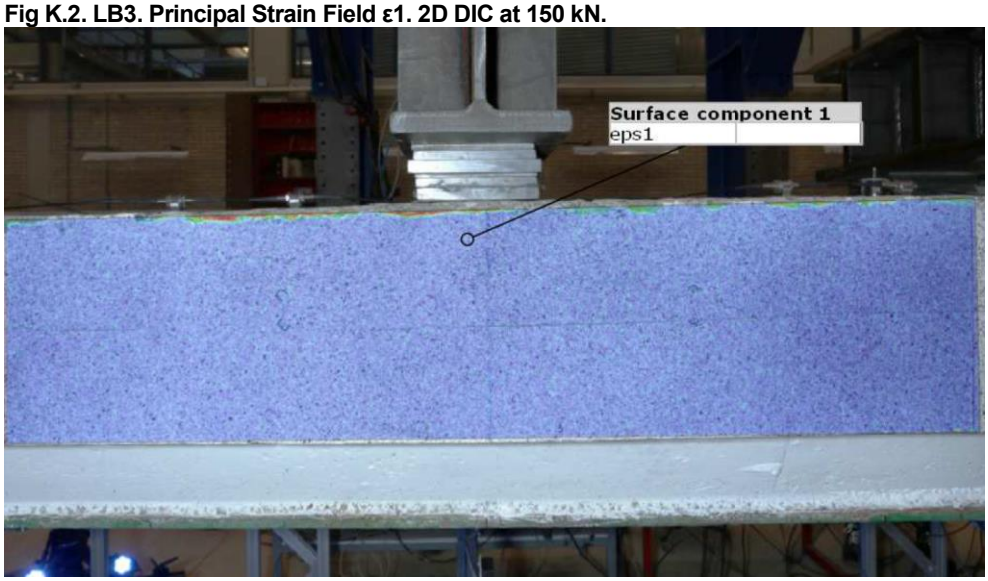

Fig K.3. LB3. Principal Strain Field ε1. 2D DIC at 250 kN.

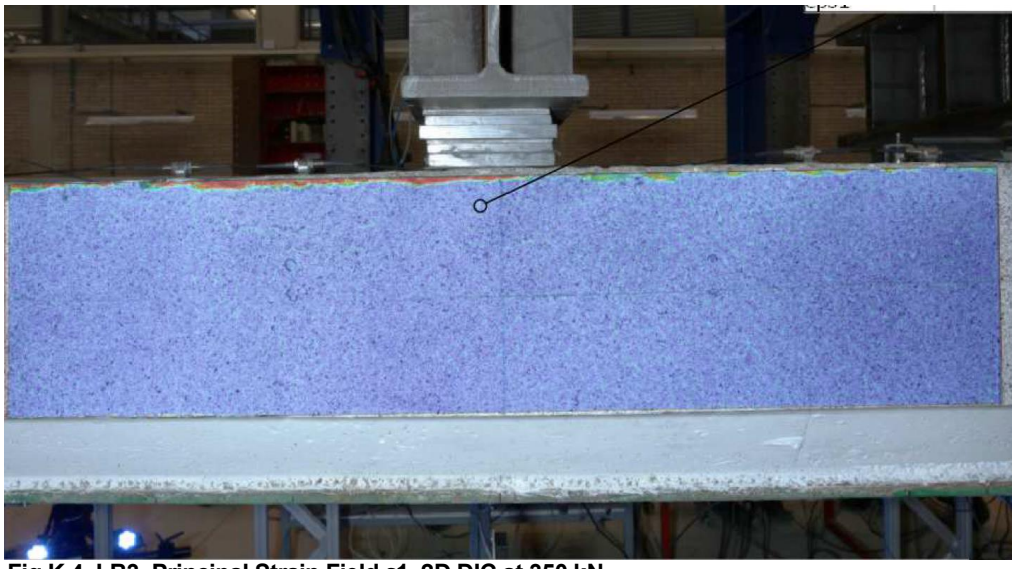

Fig K.4. LB3. Principal Strain Field ε1. 2D DIC at 350 kN.

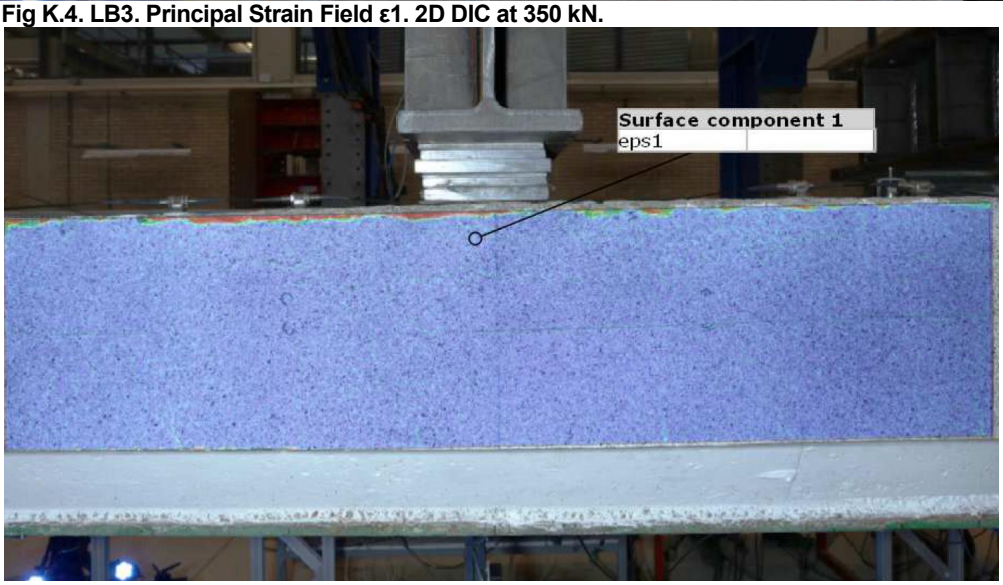

Fig K.5. LB3. Principal Strain Field ε1. 2D DIC at 450 kN.

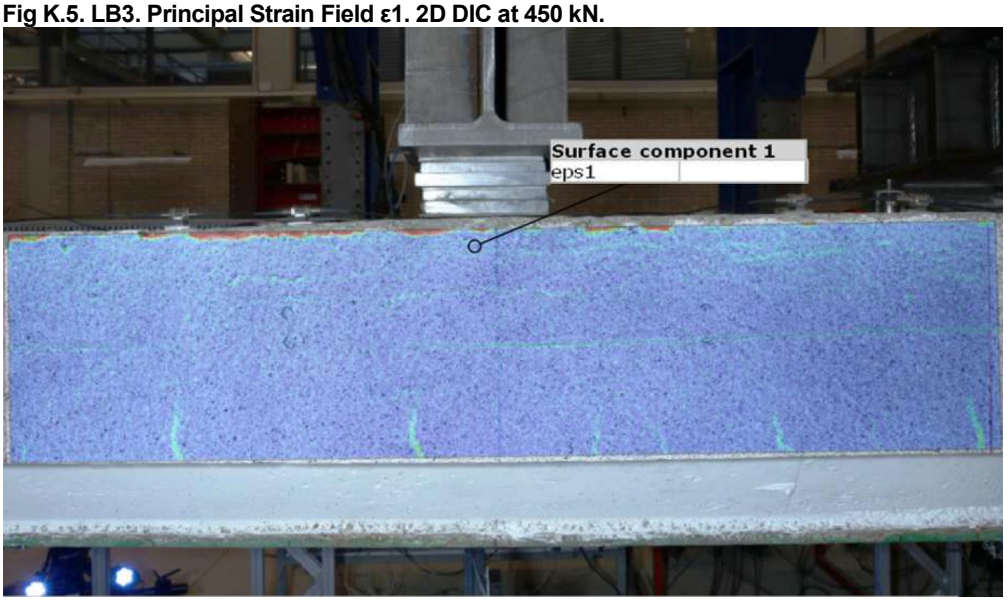

Fig K.6. LB3. Principal Strain Field ε1. 2D DIC at 850 kN.

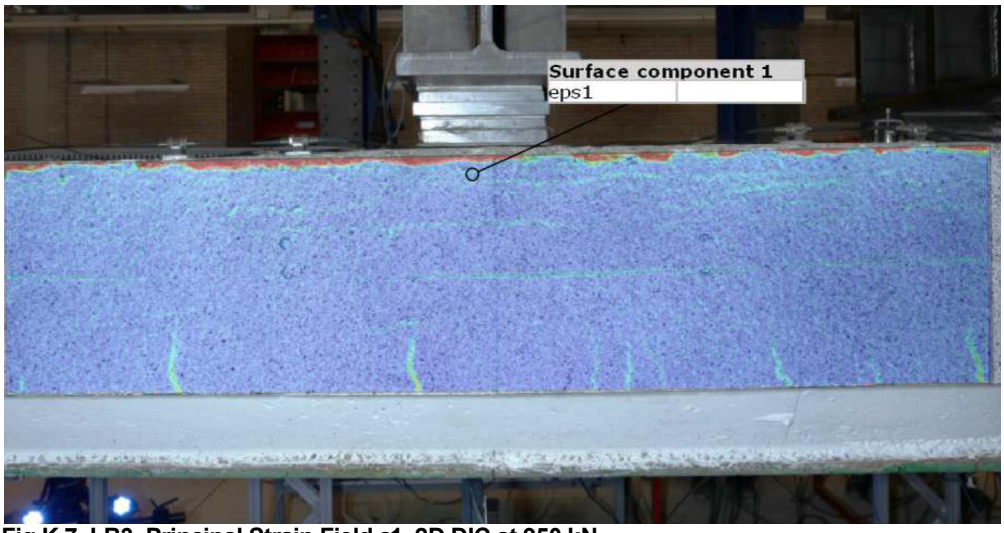

Fig K.7. LB3. Principal Strain Field ε1. 2D DIC at 950 kN.

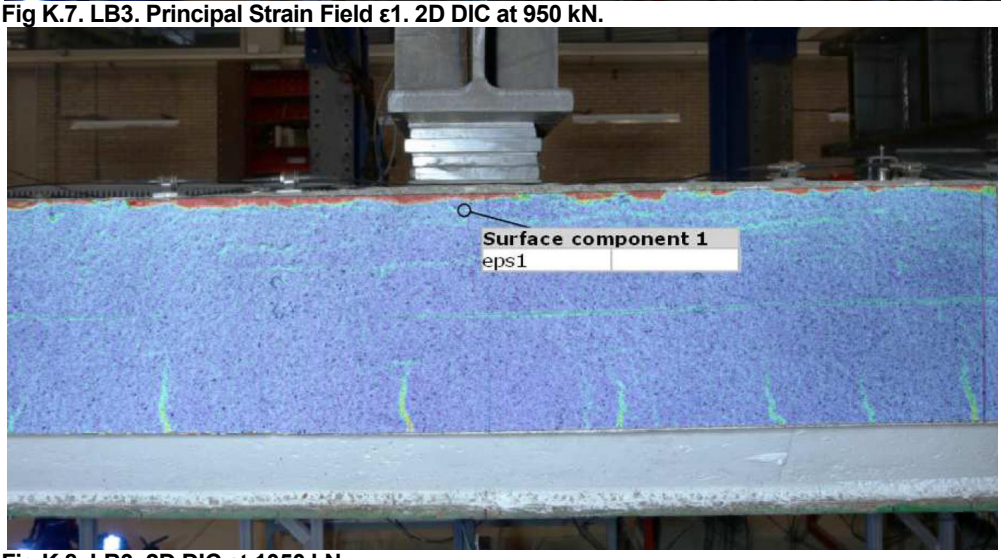

Fig K.8. LB3. 2D DIC at 1050 kN.

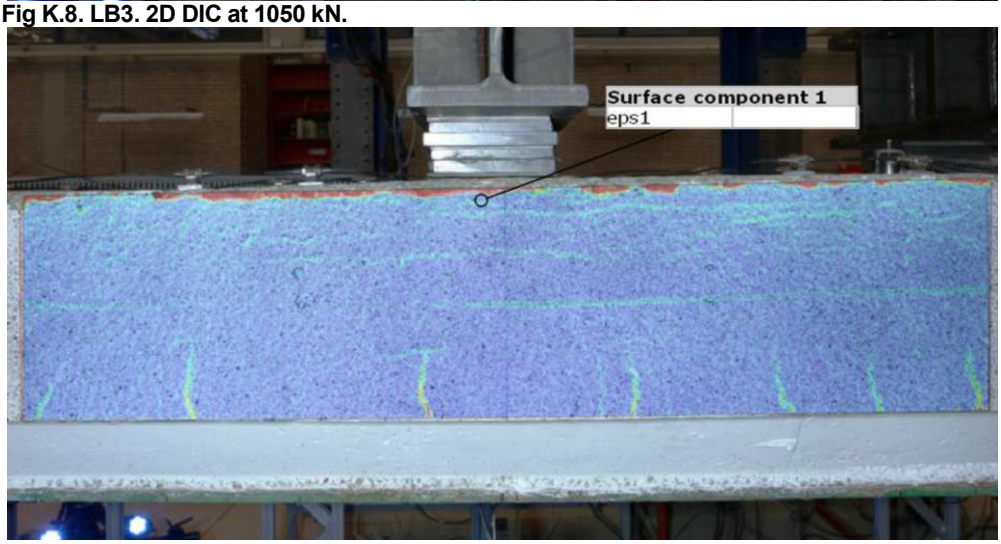

Fig K.9. LB3. Principal Strain Field ε1. 2D DIC at 1150 kN.

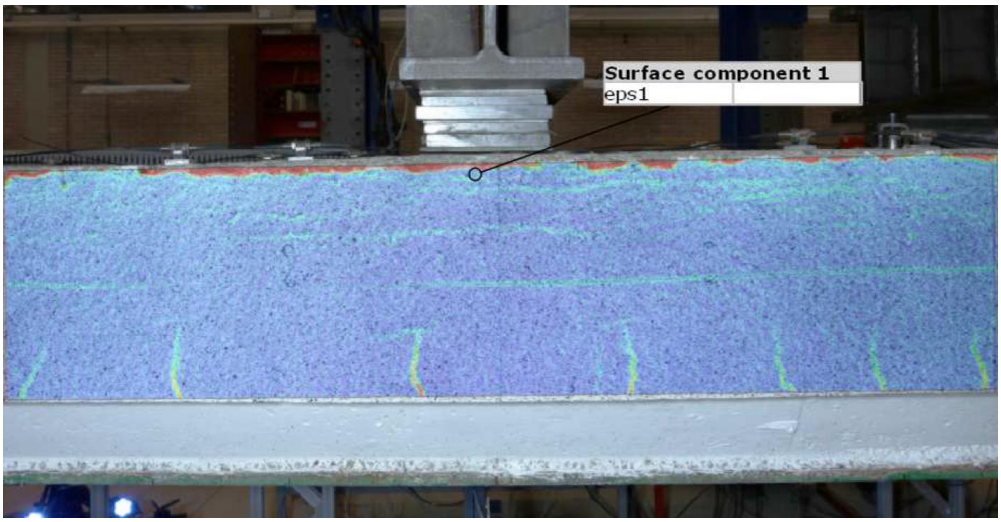

Fig K.10. LB3. Principal Strain Field ε1. 2D DIC at 1200 kN.

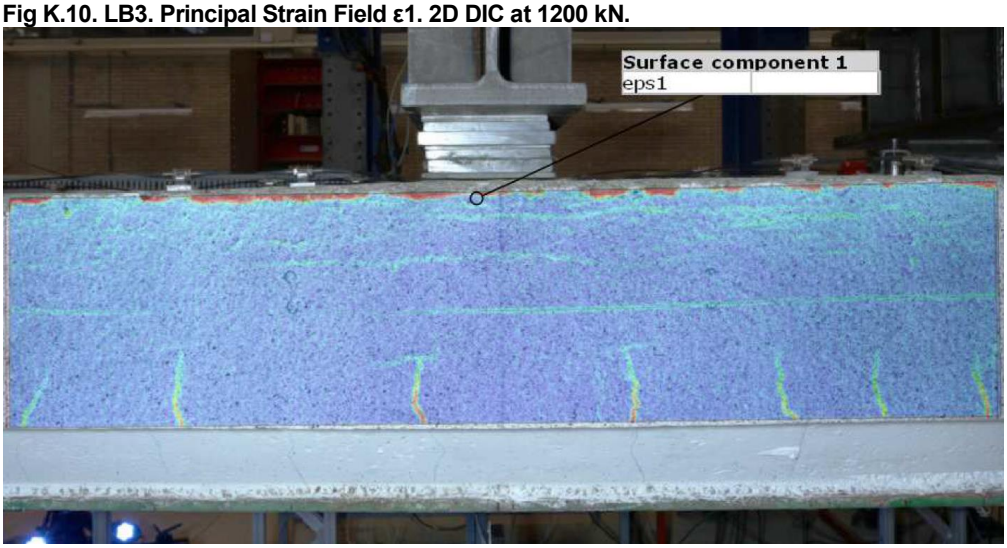

Fig K.11. LB3. Principal Strain Field ε1. 2D DIC at 1250 kN.

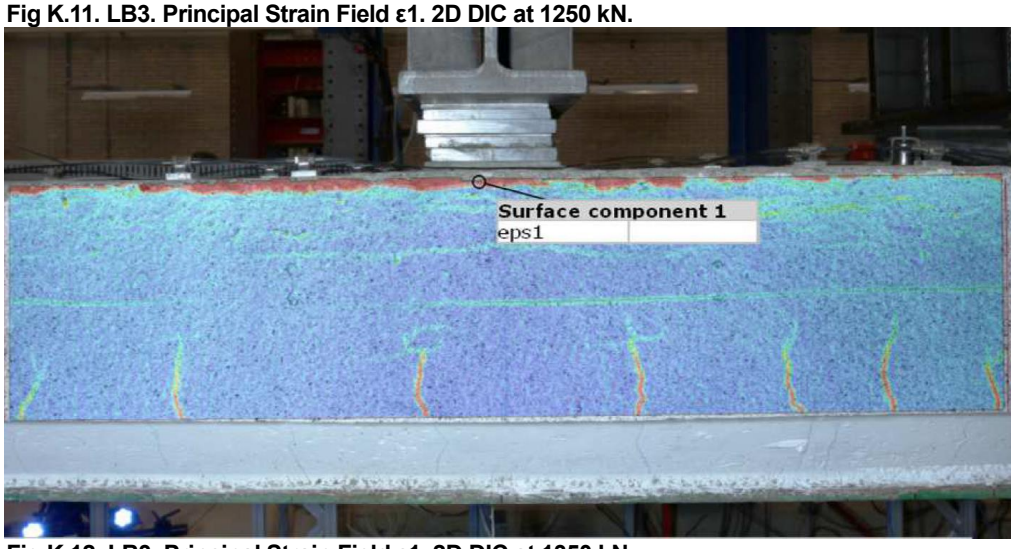

Fig K.12. LB3. Principal Strain Field ε1. 2D DIC at 1350 kN.

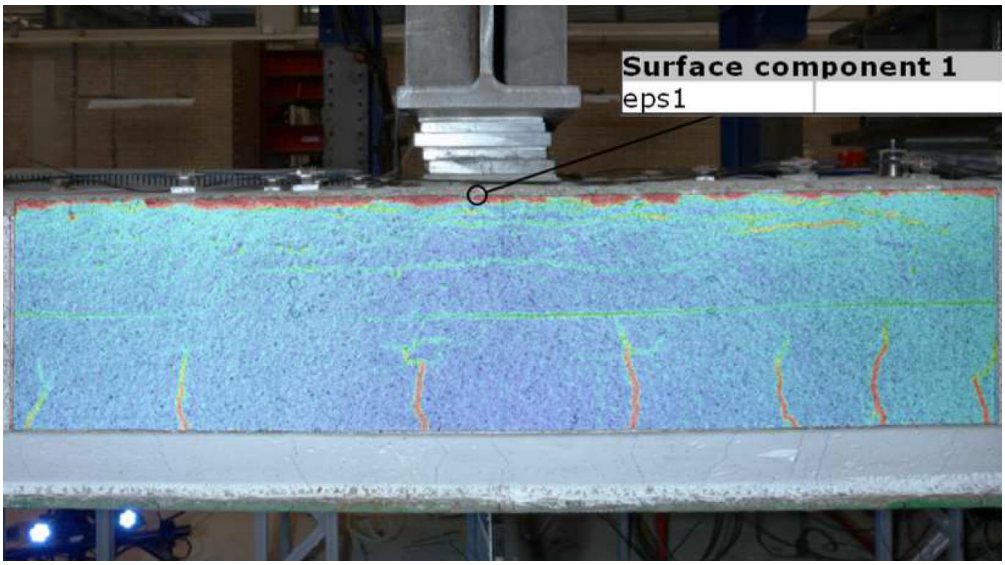

Fig K.13. LB3. Principal Strain Field ε1. 2D DIC at 1368 kN.

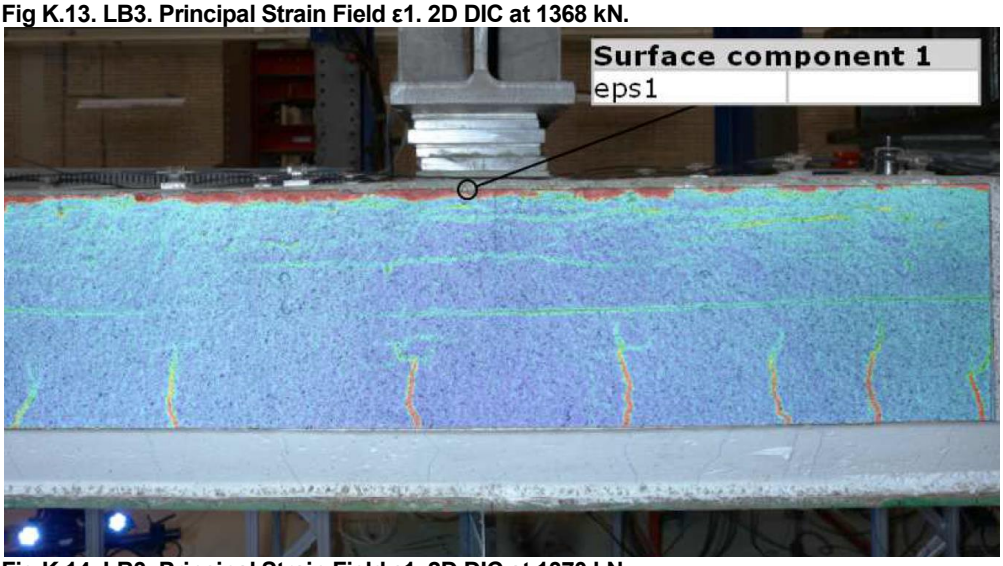

Fig K.14. LB3. Principal Strain Field ε1. 2D DIC at 1370 kN.

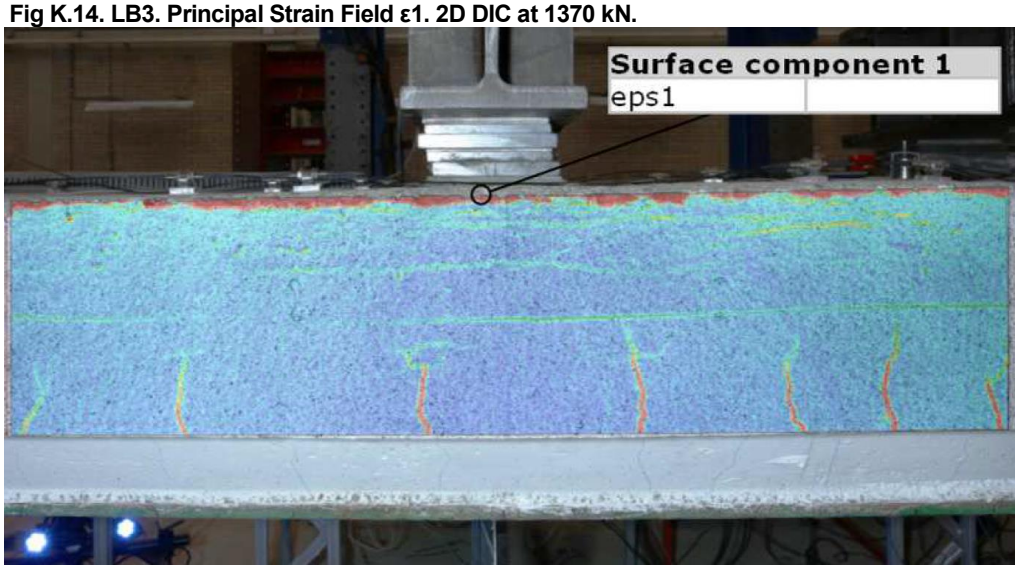

Fig K.15. LB3. Principal Strain Field ε1. 2D DIC at 1376 kN.

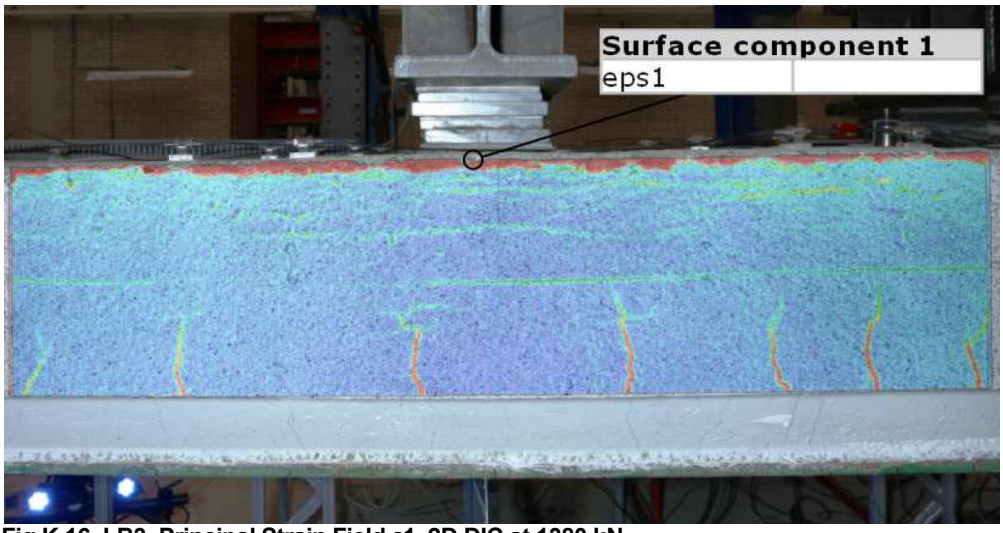

Fig K.16. LB3. Principal Strain Field ε1. 2D DIC at 1380 kN.

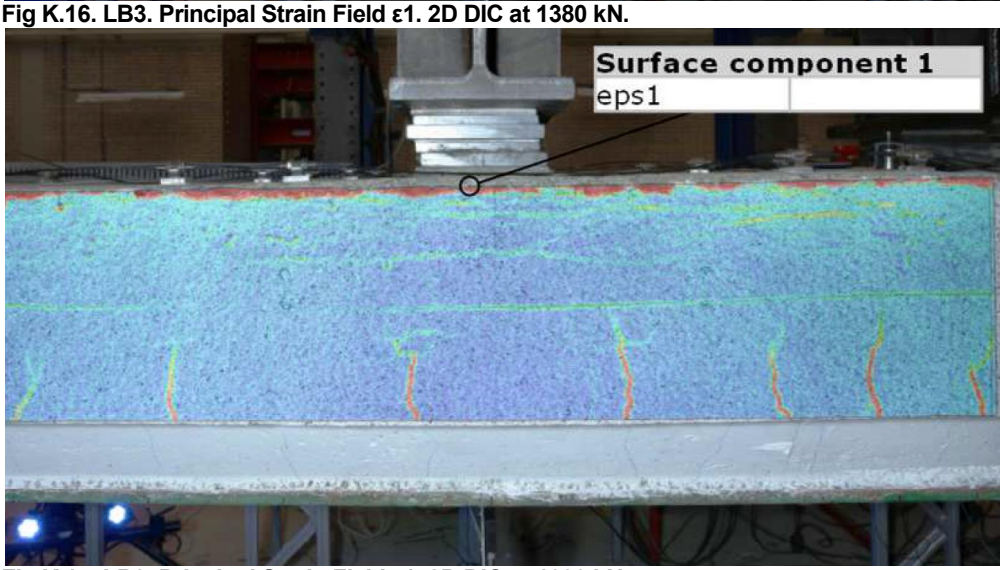

Fig K.17. LB3. Principal Strain Field ε1. 2D DIC at 1390 kN.

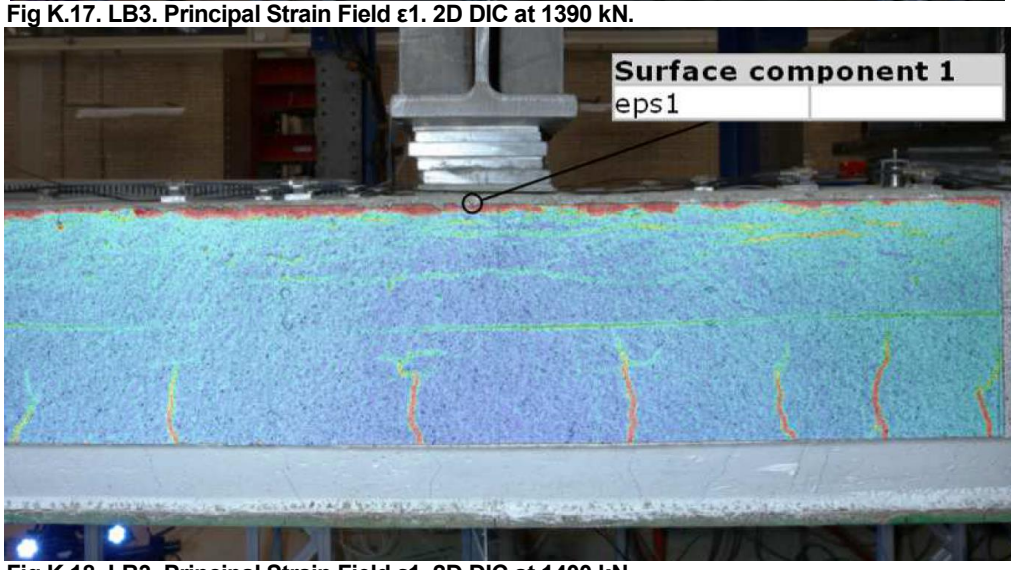

Fig K.18. LB3. Principal Strain Field ε1. 2D DIC at 1400 kN.

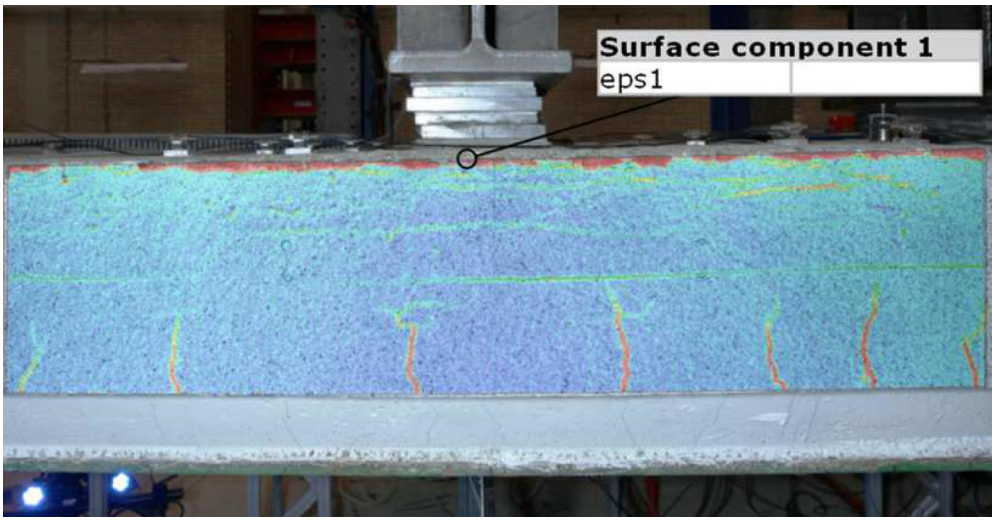

Fig K.19. LB3. Principal Strain Field ε1. 2D DIC at 1406 kN.

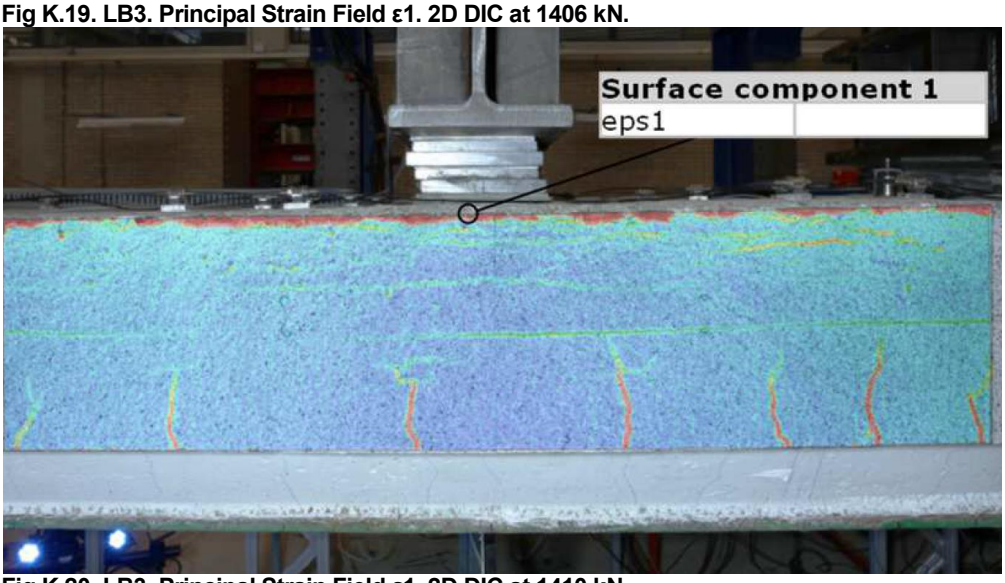

Fig K.20. LB3. Principal Strain Field ε1. 2D DIC at 1410 kN.

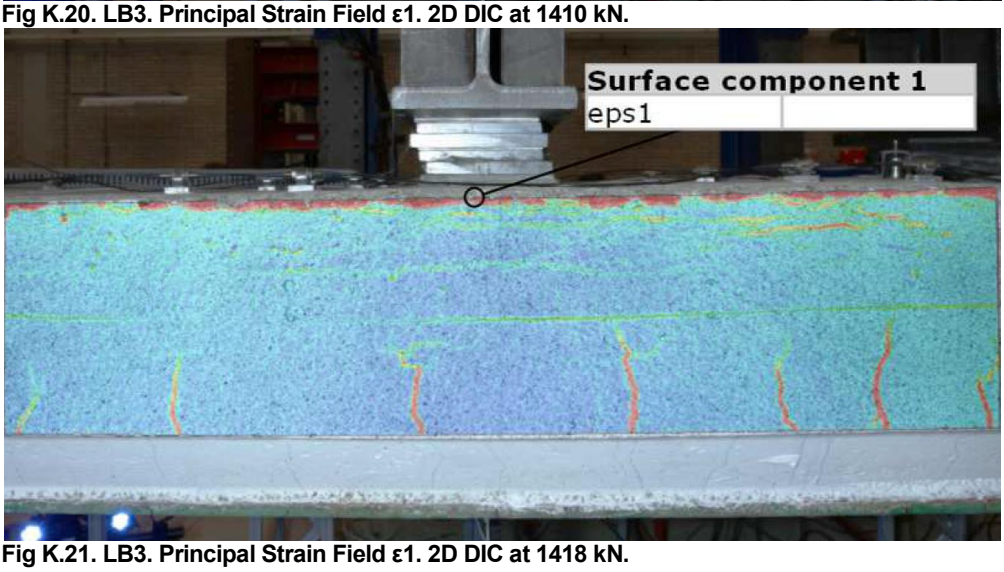

Fig K.21. LB3. Principal Strain Field ε1. 2D DIC at 1418 kN.

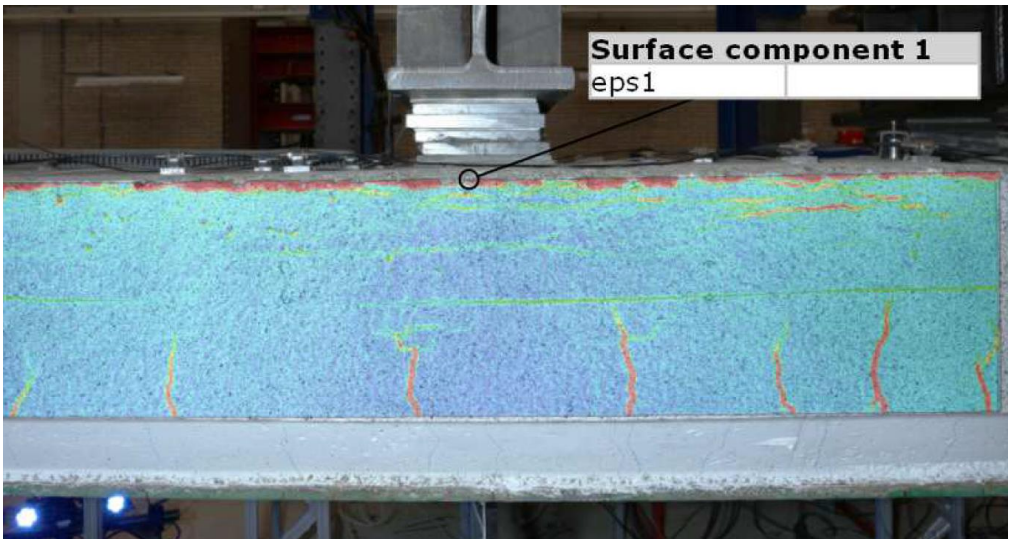

Fig K.22. LB3. Principal Strain Field ε1. 2D DIC at 1420 kN.

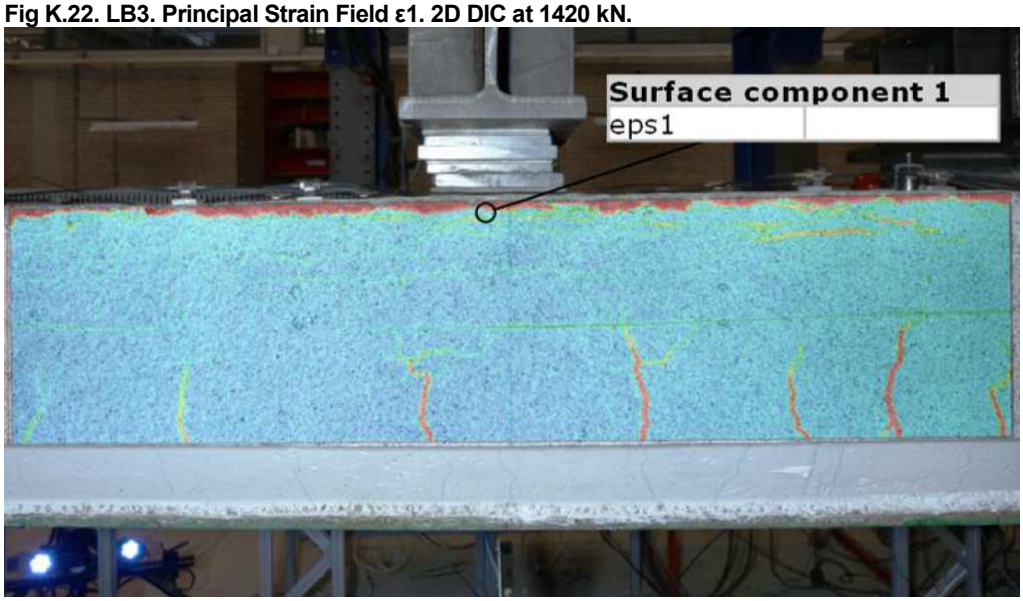

Fig K.23. LB3. Principal Strain Field ε1. 2D DIC at 0 kN. After unloading the specimen, to increase the displacement range of the hydraulic jacks.

L. 3D DIC - LB3

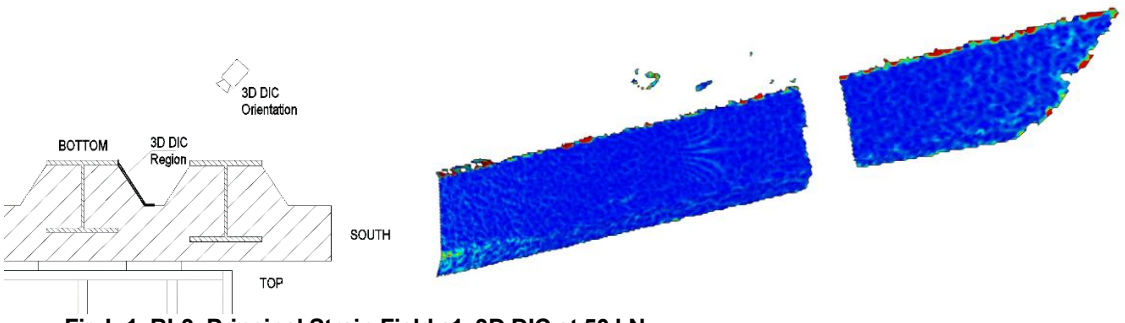

Fig L.1. BL3. Principal Strain Field ε1. 3D DIC at 50 kN.

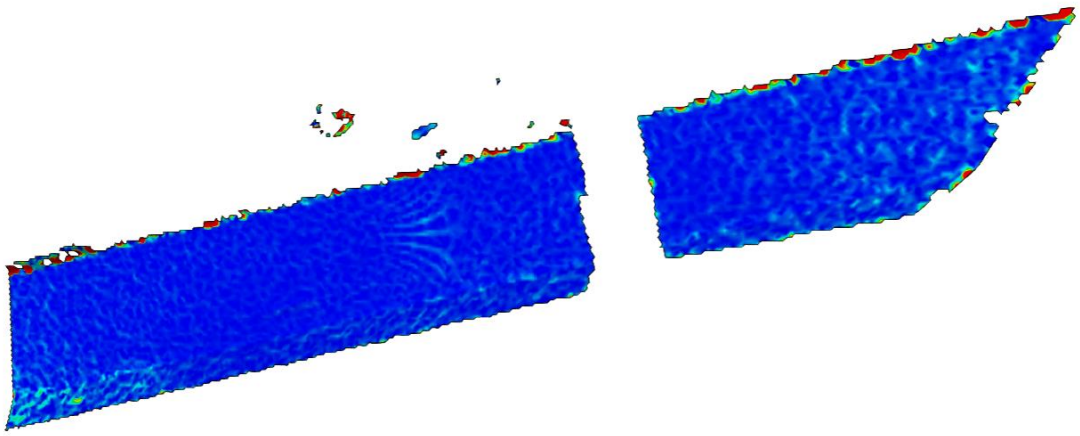

Fig L.2. LB3. Principal Strain Field ε1. 3D DIC at 150 kN.

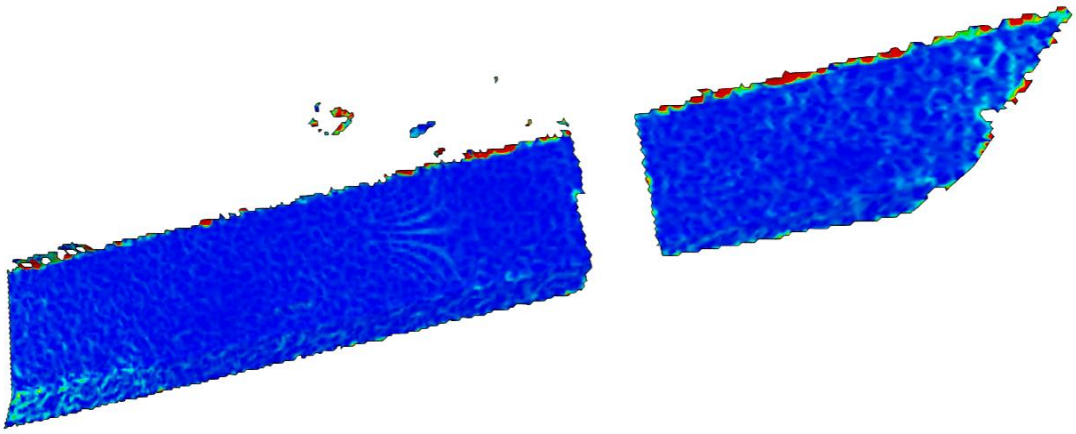

Fig L.3. LB3. Principal Strain Field ε1. 3D DIC at 250 kN.

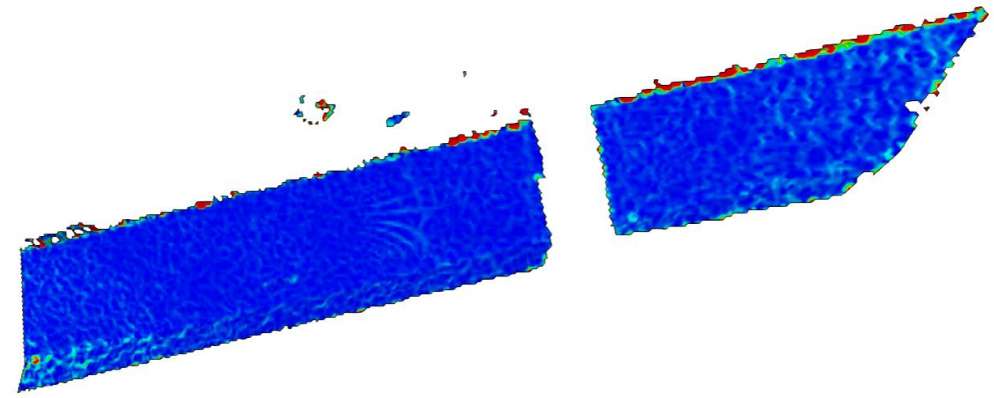

Fig L.4. LB3. Principal Strain Field ε1. 3D DIC at 350 kN.

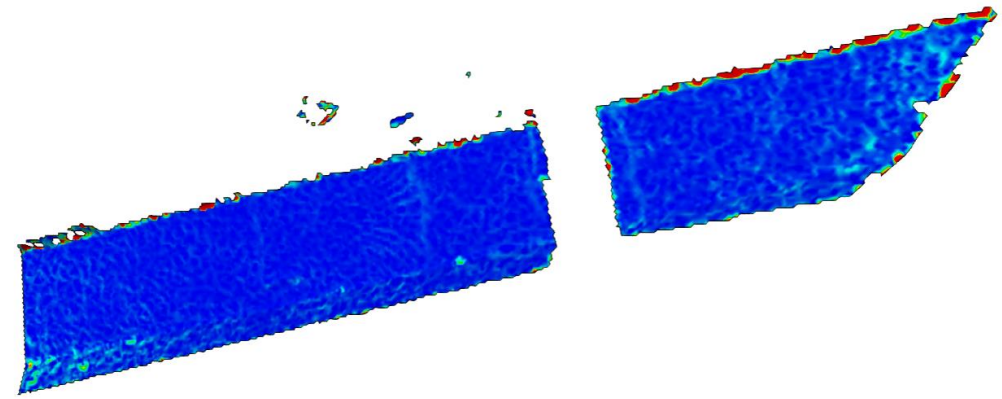

Fig L.5. LB3. Principal Strain Field ε1. 3D DIC at 450 kN.

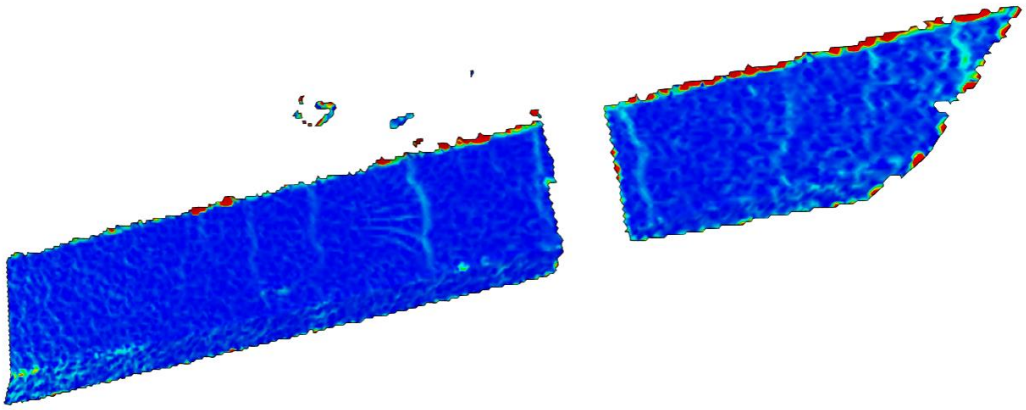

Fig L.6. LB3. Principal Strain Field ε1. 3D DIC at 650 kN.

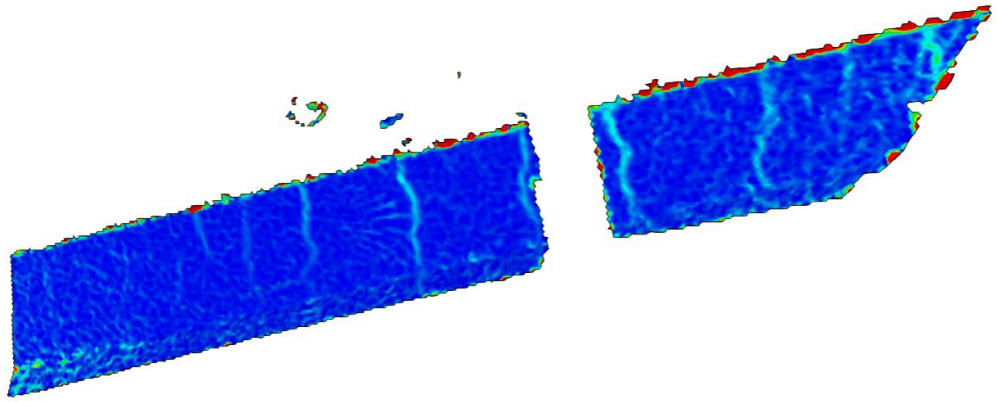

Fig L.7. LB3. Principal Strain Field ε1. 3D DIC at 850 kN.

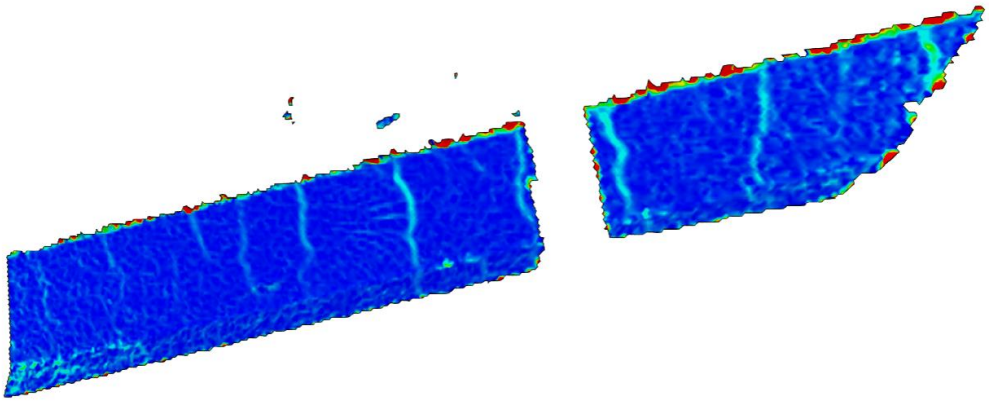

Fig L.8. LB3. Principal Strain Field ε1. 3D DIC at 950 kN.

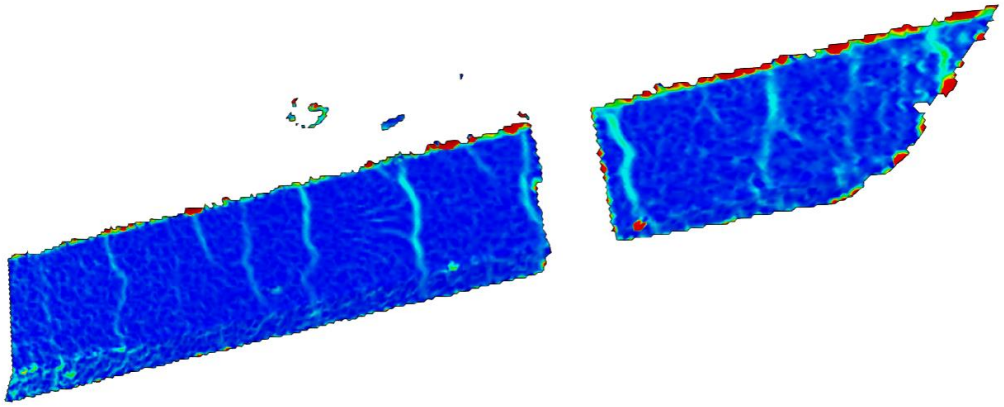

Fig L.9. LB3. Principal Strain Field ε1. 3D DIC at 1050 kN.

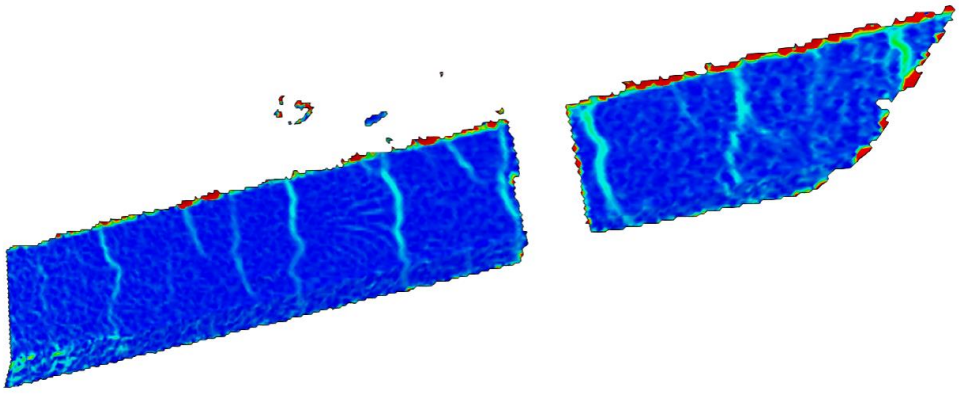

Fig L.10. LB3. Principal Strain Field ε1. 3D DIC at 1150 kN.

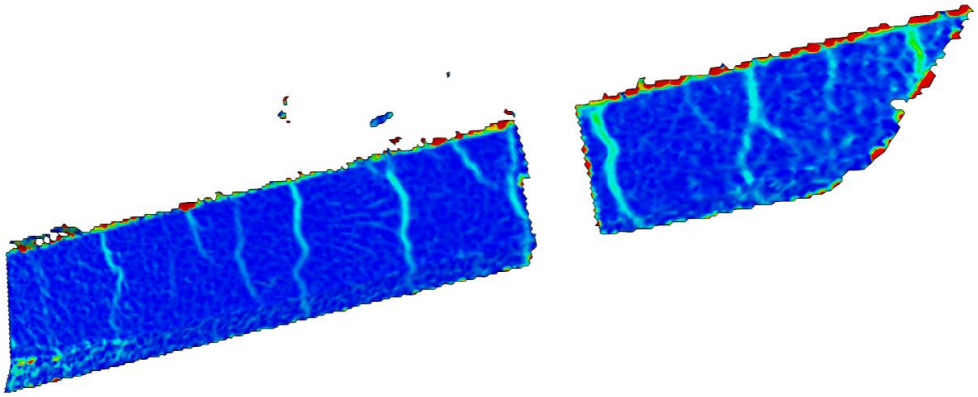

Fig L.11. LB3. Principal Strain Field ε1. 3D DIC at 1200 kN.

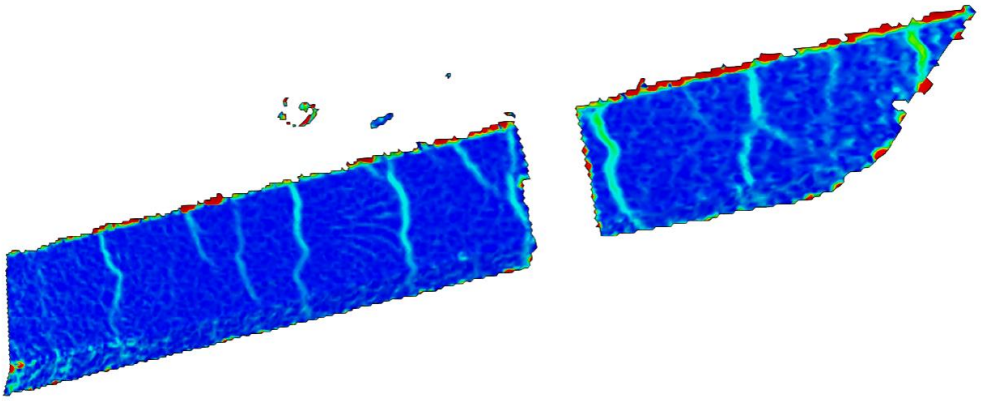

Fig L.12. LB3. Principal Strain Field ε1. 3D DIC at 1250 kN.

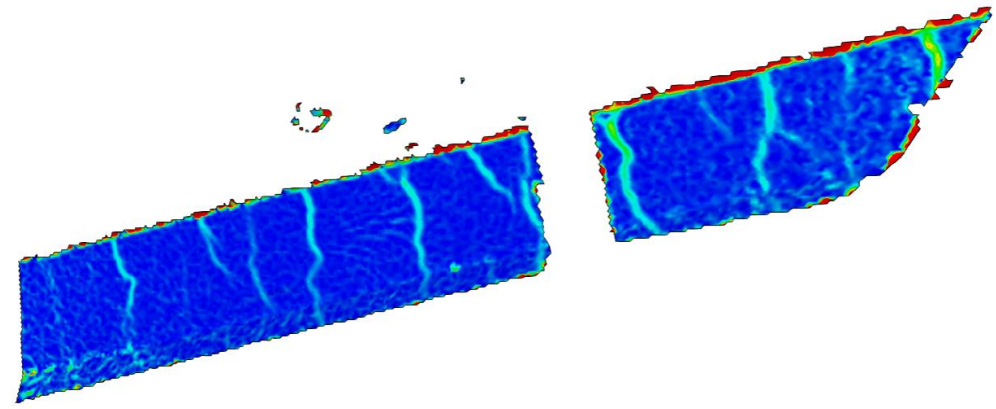

Fig L.13. LB3. Principal Strain Field ε1. 3D DIC at 1350 kN.

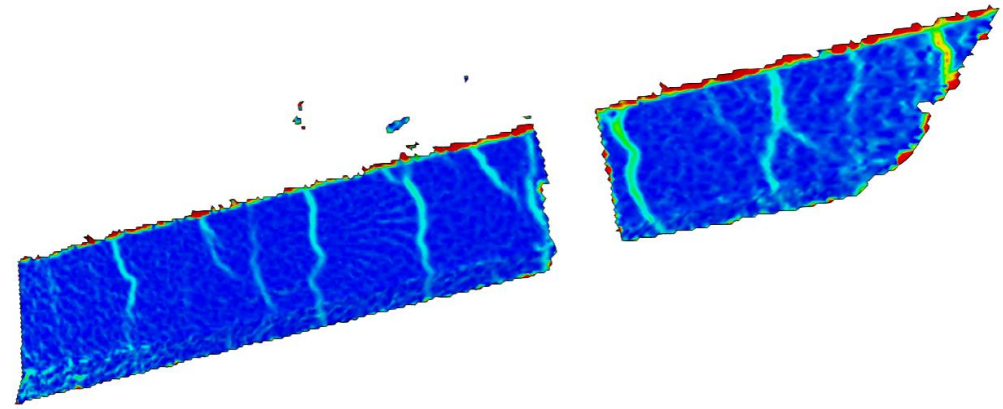

Fig L.14. LB3. Principal Strain Field ε1. 3D DIC at 1370 kN.

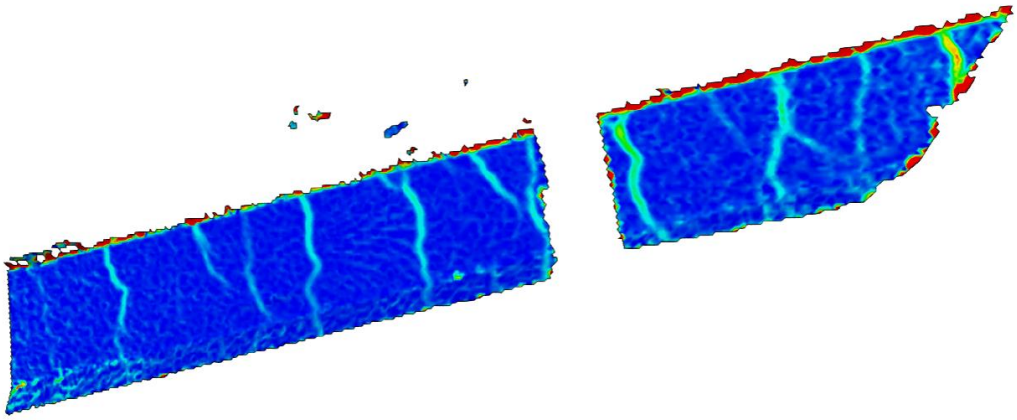

Fig L.15. LB3. Principal Strain Field ε1. 3D DIC at 1380 kN.

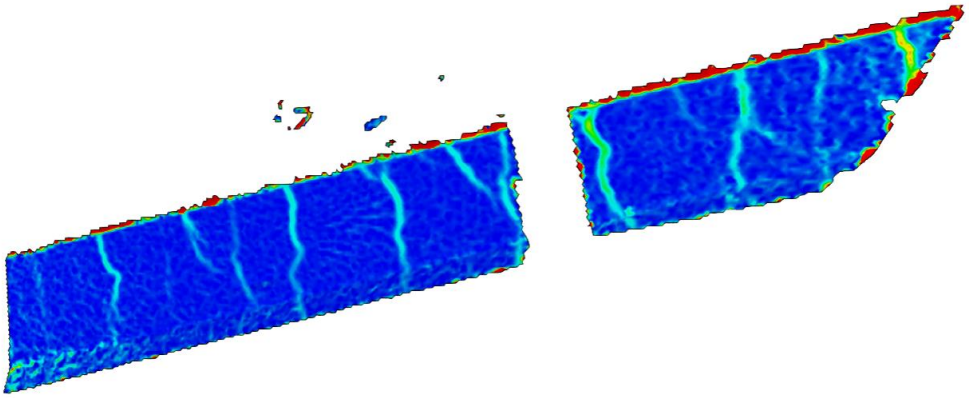

Fig L.16. LB3. Principal Strain Field ε1. 3D DIC at 1376 kN.

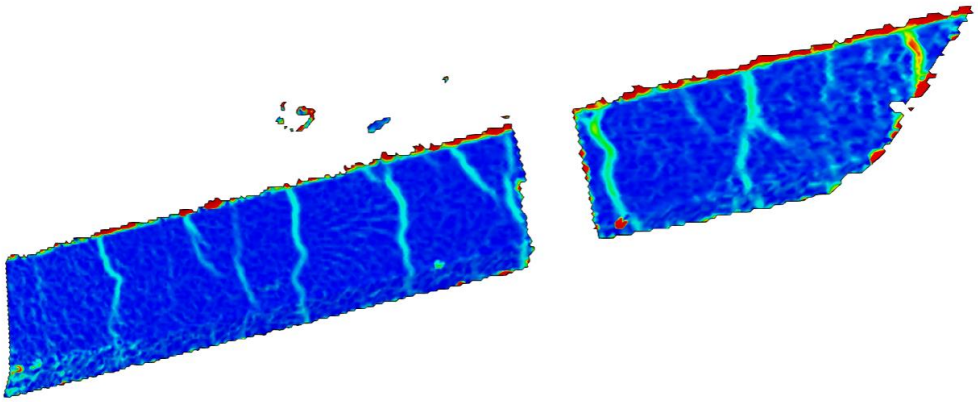

Fig L.17. LB3. Principal Strain Field ε1. 3D DIC at 1390 kN.

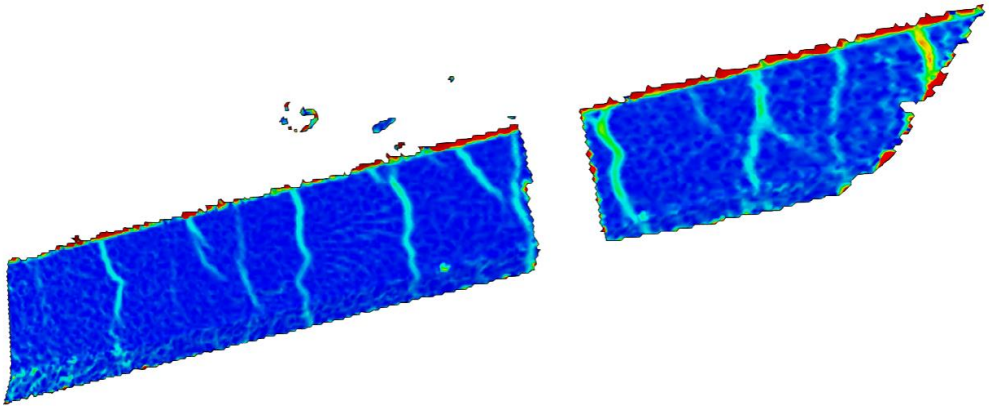

Fig L.18. LB3. Principal Strain Field ε1. 3D DIC at 1394 kN.

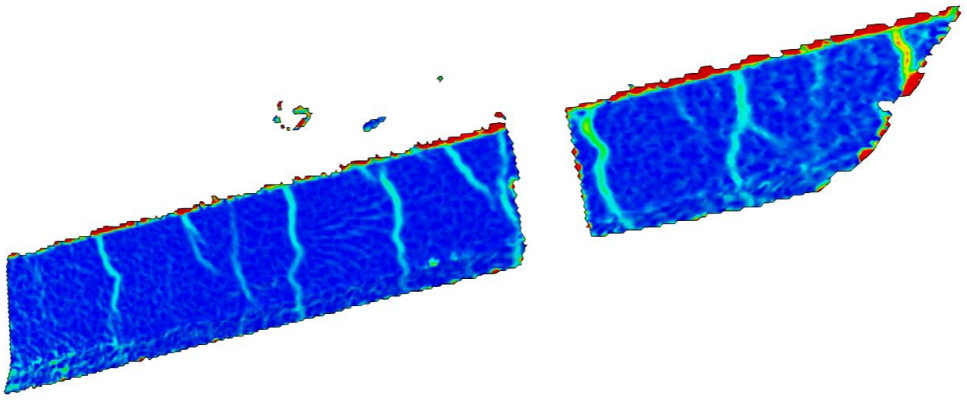

Fig L.19. LB3. Principal Strain Field ε1. 3D DIC at 1400 kN.

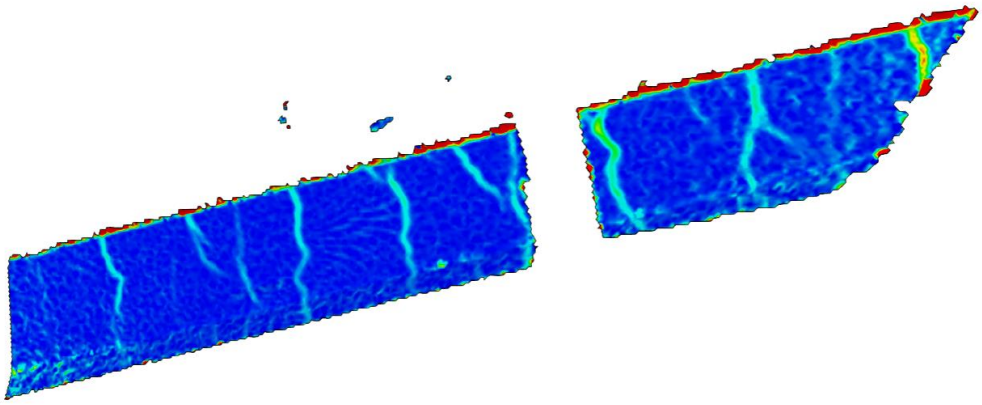

Fig L.20. LB3. Principal Strain Field ε1. 3D DIC at 1372 kN.

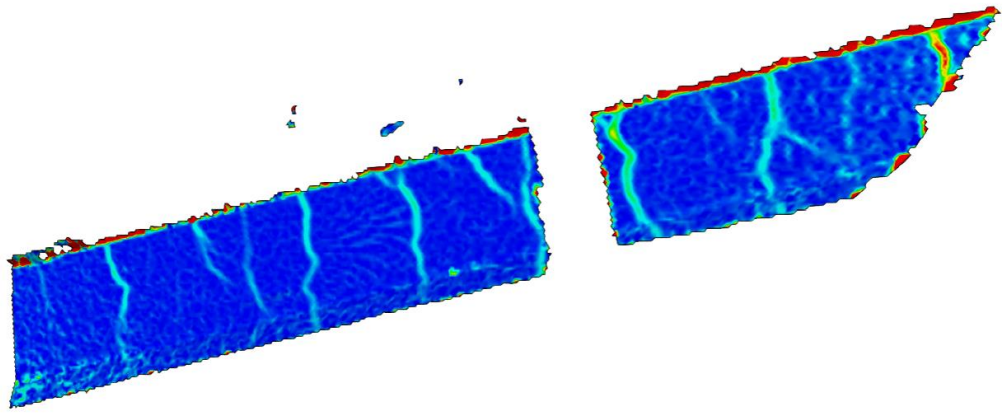

Fig L.21. Principal Strain Field ε1. LB3. 3D DIC at 1410 kN.

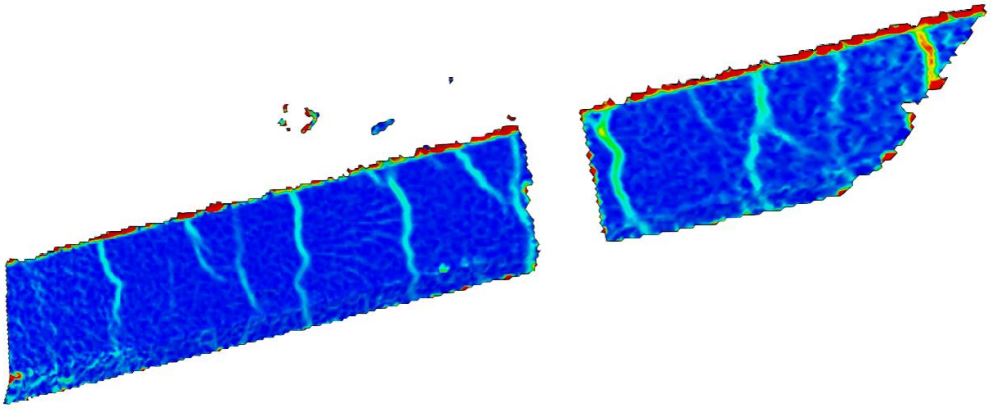

Fig L.22. LB3. Principal Strain Field ε1. 3D DIC at 1406 kN.

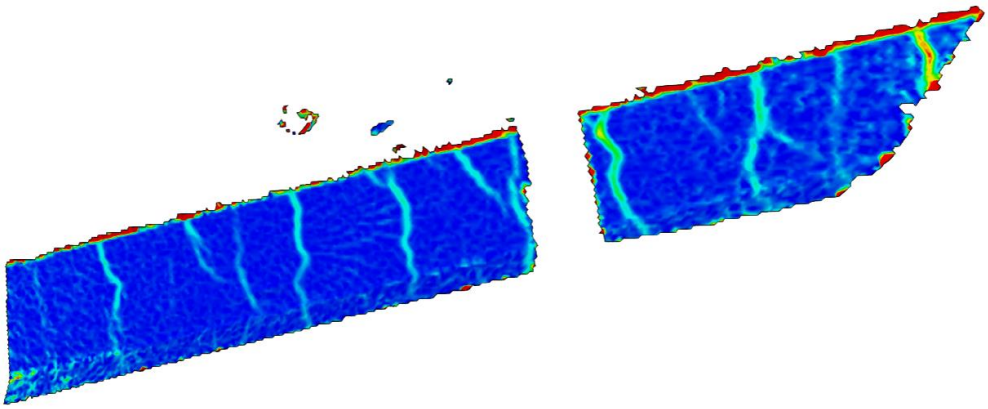

Fig L.23. Principal Strain Field ε1. LB3. 3D DIC at 1418 kN.

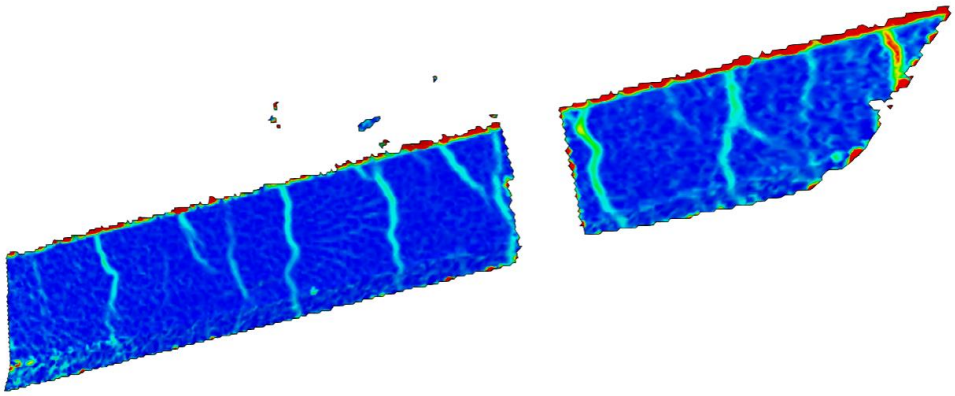

Fig L.24. Principal Strain Field ε1. LB3. 3D DIC at 1420 kN.

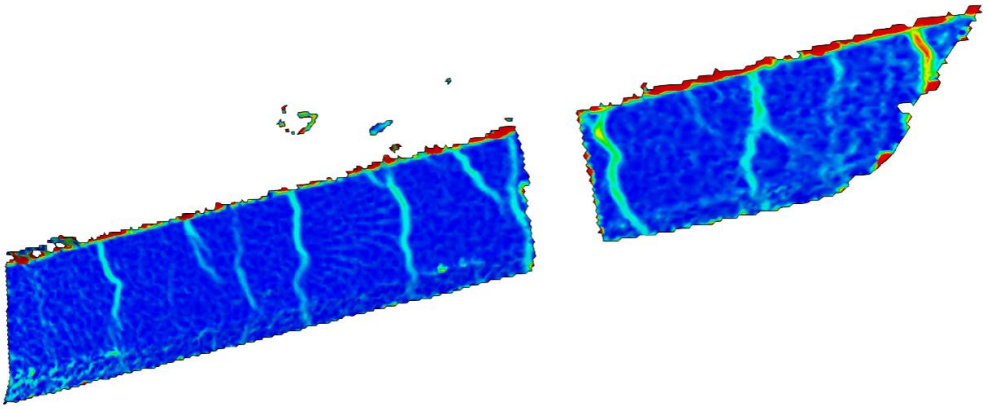

Fig L.25. LB3. Principal Strain Field ε1. 3D DIC at 1448 kN.

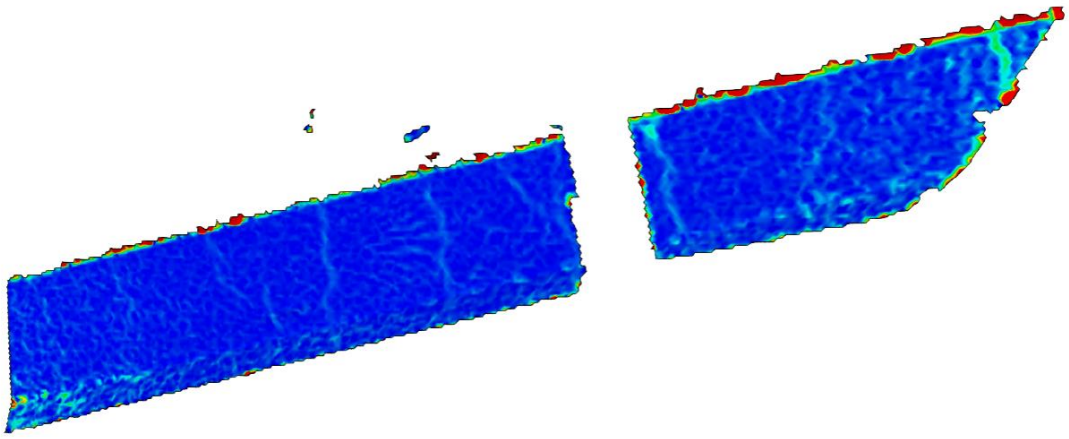

Fig L.26. LB3. Principal Strain Field ε1. 3D DIC at unloading 0 kN.